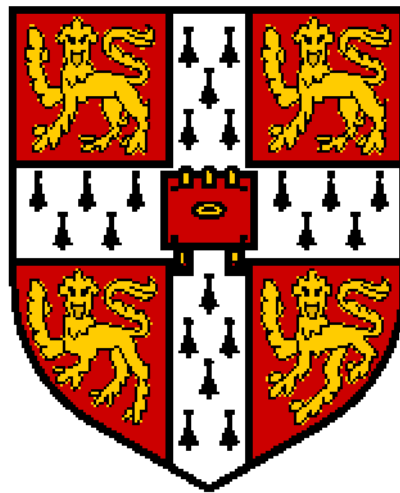


# **Vertically Aligned Nanocomposite (VAN) Oxide Films for Improved Ferroelectrics and Ferromagnetics**

**Ady Suwardi**

**Darwin College, University of Cambridge**



A dissertation submitted for the degree of Doctor of Philosophy at the

University of Cambridge

September 2017

# Preface

This dissertation is submitted for the Doctor of Philosophy degree at the University of Cambridge. The research was conducted for 2 years under the supervision of Professor Judith MacManus-Driscoll in the Device Materials Group, Department of Materials Science and Metallurgy, University of Cambridge, and for 2 years in Institute of Materials Research and Engineering, Singapore with the guidance of Dr. Yao Kui. I certify that, unless otherwise indicated, the work described is, to the best of my knowledge, original and my own work. No part of this dissertation has previously been submitted for any qualifications at this or any other university or other establishment. This dissertation does not exceed 60,000 words.

Some parts of the work in this dissertation have been part of publications as listed below:

- MacManus-Driscoll, J.; **Suwardi, A.**; Kursumovic, A.; Bi, Z.; Tsai, C.-F.; Wang, H.; Jia, Q.; Lee, O. J., New strain states and radical property tuning of metal oxides using a nanocomposite thin film approach. *APL Materials* 2015, 3 (6), 062507.
- MacManus-Driscoll, J.; **Suwardi, A.**; Wang, H., Composite epitaxial thin films: A new platform for tuning, probing, and exploiting mesoscale oxides. *MRS Bulletin* 2015, 40 (11), 933-942.
- **Suwardi, A.**; Prasad, B.; Lee, S.; Choi, E.-M.; Lu, P.; Zhang, W.; Li, L.; Blamire, M.; Jia, Q.; Wang, H.; Yao, K.; MacManus-Driscoll, J.L., Turning antiferromagnetic  $\text{Sm}_{0.34}\text{Sr}_{0.66}\text{MnO}_3$  into a 140 K ferromagnet using a nanocomposite strain tuning approach. *Nanoscale* 2016, 8 (15), 8083-8090.

Ady Suwardi

September 2017

# Acknowledgement

I would like to express my eternal gratitude for the assistance and guidance of many people during my time in Cambridge. I am forever indebted to my supervisor, Prof Judith MacManus-Driscoll for her guidance, patience and motivation throughout my study and also for patiently proofreading of my previous papers as well as this dissertation. I also wish to thank Dr. Yao Kui for his guidance and help during the time spent in Institute of Materials Research and Engineering, Singapore. I would also like to thank my parents and siblings for their constant motivation throughout my entire journey. In addition, I would like to thank Prof. Zoe Barber for being my advisor throughout my entire study. Within the Device Materials Group (DMG) in the Department of Materials Science and Metallurgy, I am extremely grateful to the abundance of help from Dr. Ahmed Kursumovic for his help in the nitty gritty details of most of my experiments in Cambridge. Without him none of the practical work would have been possible. Gratitude is extended also to Dr. Nadia Stelmashenko for many of her advice relating to AFM, PLD as well as vacuum systems. Special thanks to Mary Vickers and Andrew Moss for their help in XRD. Precious help from Dr. Shin Buhm Lee during the initial stages of my research will never be forgotten. Thanks to Dr. Seungho Cho, Dr. Abhijeet Sangle, Dr. Eun-Mi Choi, Dr. Bhagwati Prasad as well as to my fellow students from Cambridge for their support and company. Last but not least, my gratitude to Dr. Liu Huajun, Dr. Ivan Tan Chee Kiang, Dr Guo Shifeng, Dr. Chen Shuting, Dr. Li Yang, Dr. Meysam Sharifzadeh Mirshekarloo, Dr. Wong Zheng Zheng, Dr. Ke Qinqing, and all my fellow students and friends from Singapore in no particular order. I am grateful for the financial support from Agency for Science, Research and Technology (A\*STAR), Singapore.

Ady Suwardi

September 2017

# Abstract

In this work, I start by introducing a relatively recently innovated thin film architecture which offers a new direction in strain control, the vertically aligned nanocomposite (VAN). I first present the literature in the field, explaining the advantages and unique novel properties stemming from VAN structures. Next, I introduce the work I did to examine the unique strain states of  $\text{Ba}_{0.6}\text{Sr}_{0.4}\text{TiO}_3\text{-Sm}_2\text{O}_3$  VAN structures. It was found that the strain states in the functional  $\text{Ba}_{0.6}\text{Sr}_{0.4}\text{TiO}_3$  phase are unconventional compared to those in planar thin films. 3-dimensional strain was found to be acting on the  $\text{Ba}_{0.6}\text{Sr}_{0.4}\text{TiO}_3$  phase in the VAN structure. The origin of the strain was explained using a simple model which takes into account thermal expansion mismatch as well as lattice mismatch and elastic coefficients. The ferroelectric properties of the films were presented in relation to the observed strain states. I next present the work I did on the influence of strain on the magnetic properties in VAN film of  $\text{Sm}_{0.34}\text{Sr}_{0.66}\text{MnO}_3\text{-Sm}_2\text{O}_3$ . Ferromagnetism was achieved in an otherwise antiferromagnetic  $\text{Sm}_{0.34}\text{Sr}_{0.66}\text{MnO}_3$ . The effect was explained by a strain induced transition from super-exchange to double exchange coupling in the material.

Last but not least, the potential of scalability of VAN films was explored by using sputtering to grow VAN structures instead of the commonly-used PLD growth.  $\text{BaTiO}_3\text{-Sm}_2\text{O}_3$  was used as a primary study material due to its well reported VAN properties. Preliminary results showing indications of a VAN structure. Some basic physical property characterization is also presented and compared to the properties of PLD-grown films in the literature. Limitations and challenges that arise due to the fundamental differences between sputtering and PLD are also described.

# Table of Contents

Chapter 1 Introduction .....	1
1.1. Epitaxial Strain and Strain Engineering in Oxide Thin Films .....	2
1.1.1. Epitaxial Strain in Thin Films .....	2
1.1.2. Strain Engineering of Thin Films .....	4
1.2. Vertically Aligned Nanocomposite (VAN) .....	11
Chapter 2 Fabrication Process .....	22
2.1. Thin Film Deposition Techniques .....	22
2.2 Pulsed Laser Deposition (PLD) .....	24
2.2.1. Laser Fluence (Energy Density) .....	26
2.2.2. Background Gas Pressure .....	26
2.2.3. Target Materials .....	27
2.2.4. Target – Substrate Distance.....	28
2.2.5. Laser Repetition Rate and Deposition Rate .....	28
2.2.6. Substrate Temperature.....	28
2.3 Sputter Deposition .....	31
2.3.1. DC Sputtering .....	31
2.3.2. RF Sputtering .....	34
2.3.3. Magnetron sputtering .....	36
2.3.4. Reactive Sputtering.....	37
2.3.5. Deposition Parameters of RF Magnetron Sputtering.....	37
Chapter 3 Experimental Characterization Techniques.....	42
3.1 XRD .....	42
3.1.1. $2\theta - \omega$ Scans .....	44
3.1.2. $\omega$ Scan (Rocking Curve).....	45
3.1.3. Phi Scans.....	46
3.1.4. Reciprocal Space Map (RSM) .....	47
3.2. AFM .....	48
3.2.1. Contact Mode.....	49

3.2.2. Tapping Mode .....	49
3.2.3. Piezoresponse Force Microscopy (PFM).....	50
3.3. Superconducting Quantum Interference Device (SQUID) .....	50
3.4. Ferroelectric Properties .....	51
3.5. Field Emission Scanning Electron Microscope (FESEM).....	54
3.6. Transmission Electron Microscopy (TEM) and Scanning Transmission Electron Microscopy (STEM).....	56
Chapter 4 3-D Strain States in $(\text{Ba}_{0.6}\text{Sr}_{0.4}\text{TiO}_3)_{1-x}-(\text{Sm}_2\text{O}_3)_x$ and Its Influence on Ferroelectricity.....	57
4.1 Introduction.....	57
4.2 3D Auxetic-like Strain in $(\text{Ba}_{0.6}\text{Sr}_{0.4}\text{TiO}_3)_{1-x}-(\text{Sm}_2\text{O}_3)_x$ VAN .....	59
4.3 Origin of Plane Strain States in $(\text{Ba}_{0.6}\text{Sr}_{0.4}\text{TiO}_3)_{1-x}-(\text{Sm}_2\text{O}_3)_x$ VAN .....	68
4.3.1. For $x = 0.25$ and $x = 0.50$ .....	68
4.3.2. For $x = 0.75$ .....	72
4.4 Ferroelectric Properties .....	73
Chapter 5 Turning Antiferromagnetic SSMO into A Ferromagnetic Using VAN .....	78
5.1. Magnetism and Magneto-Transport.....	78
5.2. Ferromagnetic Insulators .....	82
5.3. Growth of $\text{Sm}_{0.34}\text{Sr}_{0.66}\text{MnO}_3-\text{Sm}_2\text{O}_3$ VAN Thin Films .....	86
5.4. Magnetic and Electrical Properties of $\text{Sm}_{0.34}\text{Sr}_{0.66}\text{MnO}_3-\text{Sm}_2\text{O}_3$ VAN Thin Films .....	95
Chapter 6 Exploration of VAN Structure Formation and Properties Using Sputter Deposition.....	102
6.1. Sputter Growth of $\text{BaTiO}_3-\text{Sm}_2\text{O}_3$ .....	102
6.1.1 Effect of Substrate Temperature.....	103
6.1.2 Effect of Sputtering Power.....	104
6.1.3 Effect of Total Gas Pressure.....	106
6.1.4 Effect of Ar/O <sub>2</sub> Ratio .....	107
6.1.5 Other Characterizations and Conclusions.....	108
6.2. Sputtering Growth of Other Nanocomposite Materials .....	115

6.2.1. Cu <sub>2</sub> O-ZnO Nanocomposite .....	115
6.2.2. BaTiO <sub>3</sub> -Cu <sub>2</sub> O Nanocomposite .....	117
6.3. Limitations and Challenges in Using Sputtering for VAN Growth .....	122
6.3.1. Ablation Selectivity.....	122
6.3.2. Inter-relationship between Deposition Parameters .....	123
6.3.3. Continuity of Deposition.....	125
Chapter 7 Conclusions and Future Works.....	126
Reference .....	128

## List of Acronyms

AFM	Atomic force microscopy
ALD	Atomic layer deposition
BSTO	$\text{Ba}_{1-x}\text{Sr}_x\text{TiO}_3$
BTO	$\text{BaTiO}_3$
CFO	$\text{CoFe}_2\text{O}_4$
CVD	Chemical vapor deposition
DC	Direct current
DFT	Density functional theory
DME	Domain matching epitaxy
FESEM	Field-emission scanning electron microscopy
FWHM	Full-width half maximum
HRTEM	High resolution tunneling electron microscopy
LCMO	$\text{La}_{1-x}\text{Ca}_x\text{MnO}_3$
LSMO	$\text{La}_{1-x}\text{Sr}_x\text{MnO}_3$
MAD	Metalorganic aerosol deposition
MBE	Molecular beam epitaxy
MEMS	Microelectromechanical systems
MTJ	Magnetic tunnel junction
PFM	Piezo-response force microscopy
PLD	Pulsed laser deposition
PVD	Physical vapor deposition
PZT	$\text{Pb}[\text{Zr}_x\text{Ti}_{1-x}]\text{O}_3$
RF	Radio frequency
RHEED	Reflection high-energy electron diffraction
RSM	Reciprocal space mapping
SPM	Scanning probe microscopy
SQUID	Superconducting quantum interference device
SRO	$\text{SrRuO}_3$
SSMO	$\text{Sm}_{1-x}\text{Sr}_x\text{MnO}_3$
STEM	Scanning tunneling electron microscopy
STO	$\text{SrTiO}_3$

T <sub>c</sub>	Curie temperature
TEM	Tunneling electron microscopy
UHV	Ultra high vacuum
UV	Ultraviolet
VAN	Vertically-aligned nanocomposite
XPS	X-ray photoelectron spectroscopy
XRD	X-ray diffraction

# Overview of Chapters

This thesis focuses on the growth and characterization of vertically aligned nanocomposites (VAN) epitaxial thin films and the interesting ferroelectric and ferromagnetic properties that are achieved using them. Chapter 1 presents an introduction to the thesis including the nature of standard epitaxial oxide thin films and VAN films. Chapter 2 presents thin film deposition techniques with a focus on pulsed laser deposition (PLD) as well as sputtering which are used extensively in this study. Various thin film characterization techniques are presented in Chapter 3.

From Chapter 4 onwards, the research work undertaken in the thesis is presented. Due to the variety of topics for each chapter, the background and motivation as well as experimental details are presented at the beginning of each chapter rather than a separate chapter. Chapter 4 focuses on understanding the nature and origin of strain in VAN architectures as well as the improvement of ferroelectric properties in  $\text{Ba}_{0.6}\text{Sr}_{0.4}\text{TiO}_3$  VAN. Chapter 5 presents the results on inducing new strain states in  $\text{Sm}_{0.34}\text{Sr}_{0.66}\text{MnO}_3$  VAN films and it discusses how this enables  $\text{Sm}_{0.34}\text{Sr}_{0.66}\text{MnO}_3$  from be changed from an antiferromagnet into a ferromagnetic phase. Chapter 6 focuses on VAN fabrication using sputtering. Lastly, the Conclusions as well as Future Work are presented in Chapter 7.

# Chapter 1 Introduction

This chapter presents a short overview of the dissertation, as well as a background to oxide thin film growth, strain effects in thin films and VAN films.

Over the past decades, many studies have been done to achieve a more complete understanding of transition metal-oxides and the resulting functional properties such as magnetism, ferroelectricity, and superconductivity. With the advances in physical vapor deposition as well as better characterization technologies, thin film growth has become increasingly viable and popular. The modern study of complex oxide materials has largely been led by the development of new growth and characterization techniques that have allowed researchers unprecedented access to new phases, structures and properties of these materials.<sup>1</sup> For instance, epitaxial growth of thin films provides an unconventional pathway to discovery and stabilization of new materials that otherwise will not be stable in bulk. High quality thin film materials can be produced much faster than by bulk single crystal growth which is time consuming and they can be integrated in electronic devices which bulk crystals cannot.<sup>2</sup>

More recently, the novel thin film architecture of vertically-aligned nanocomposites (VAN) has also been demonstrated.<sup>3-4</sup> A VAN consists of vertically aligned distinctive phases normally grown on a single crystal substrate. The main characteristics that define VAN architecture is the ability to couple multiple functional properties through strain. This renders epitaxial VAN films new functional properties. The inducement of strain resulting from elastic coupling is vital for the control of multi-functionalities and to offer the possibility of functionalities which cannot be obtained in standard films. Thus, one of the focuses of this work is to understand and provide a model to explain the epitaxial strain states which arise in VAN oxide thin films.

# 1.1. Epitaxial Strain and Strain Engineering in Oxide Thin Films

## 1.1.1. Epitaxial Strain in Thin Films

Strain represents the change of material's sizes compared with that in the pure, as-synthesized state. In thin films, strain mainly originates from hetero-epitaxy on the substrates on which the thin films are grown. The lattice parameters of the thin films and the substrates are usually not identical and during growth the thin films adjust itself to minimize the interfacial energy with the substrate in the form of strain.

Figure 1.1 shows three different modes of film growth on a substrate. Figure 1.1 (a) shows homo-epitaxy/commensurate growth which happens when the substrate and film are of the same lattice parameter. Figure 1.1 (b) shows hetero-epitaxy growth of materials with different lattice parameters, hetero-epitaxy is often used for strain engineering in functional thin film growth.

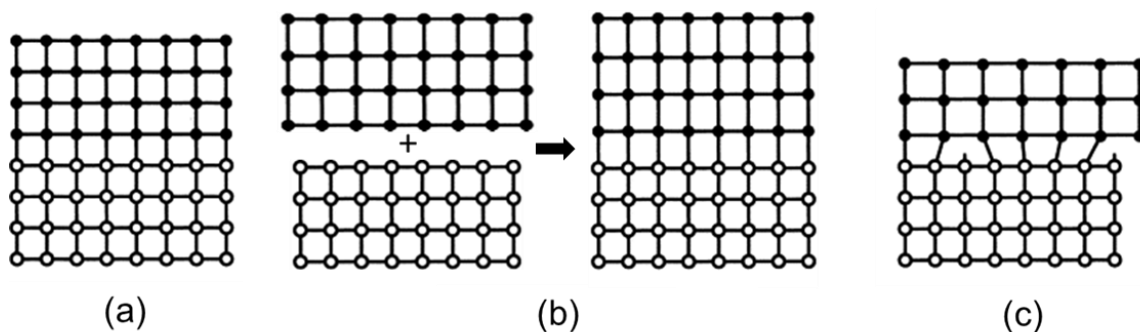


Figure 1.1 Schematic of different types of lattice matching in thin film growth on substrate showing (a) homoepitaxy/commensurate growth, (b) pseudomorphic/fully strained growth, and (c) Incommensurate/fully relaxed growth. (Figure from <sup>5</sup>)

The grown film in Figure 1.1 (b) is under tensile or compression stress on the substrate without relaxing this strain by generating misfit dislocations. To understand how stress develop in thin film, it is useful to look at lattice mismatch. The *in-plane* lattice mismatch of film with respect to substrate is evaluated by:

$$f = \frac{a_{f0} - a_s}{a_{f0}} \quad (1.1),$$

where  $a_s$  is *in-plane* the lattice parameter of the substrate and  $a_{f0}$  is the *in-plane* lattice parameter of the thin films in its original (strain-free) condition.

The *in-plane* biaxial strain  $\epsilon_{//}$  of the film grown on substrate is defined as:

$$\epsilon_{//} = \frac{a_f - a_{f0}}{a_{f0}} \quad (1.2),$$

Likewise, the *out-of-plane* strain  $\epsilon_{\perp}$  of the thin film is defined as:

$$\epsilon_{\perp} = \frac{a_{f\perp} - a_{f0\perp}}{a_{f0\perp}} \quad (1.3).$$

Where  $a_{f\perp}$  and  $a_{f0\perp}$  is the *out-of-plane* lattice parameters of the strained film and strain-free film, respectively. Positive results from the above equations represents tensile strain and vice versa.

It is important to note that in hetero-epitaxy thin film growth, the strain can only exist up to a certain thickness before it becomes fully relaxed, as shown in Figure 1.1 (c).

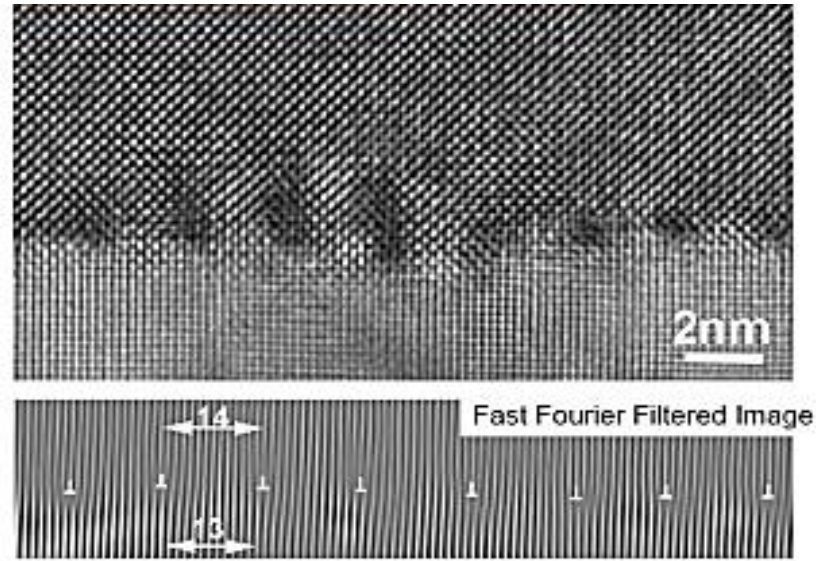


Figure 1.2 High resolution transmission electron microscopy (HRTEM) and fast Fourier filtered images showing domain matching epitaxy of SrTiO<sub>3</sub> thin film with MgO substrate forming a 14:13 domain matching relationship.(Figure from <sup>6</sup>)

It is interesting to note that when lattice mismatch is very large, e.g.  $f > 0.7\%$ , it is

possible for domain matching epitaxy (DME) to form (shown in Figure 1.2.<sup>6</sup>) In this case, the epitaxial growth of thin films is possible by domains matching of integral multiples of substrate and film lattice units across the interface.<sup>7</sup>

In the case of domain matching epitaxy, misfit dislocations can be found at the interface between substrate and film. These dislocations serve to fully or partially relax the strain, resulting in unstrained, high quality growth throughout the film thickness.

A great advantage of epitaxial thin film growth is that it enables strain manipulation in thin films through careful selection of substrates. This can be used to deposit films with desirable physical properties since strain states in functional oxide films affect their physical properties. For instance, biaxial strains from substrate was reported to induced magnetic anisotropy and influences the magneto-transport properties in epitaxial manganite films.<sup>8-9</sup>

### **1.1.2. Strain Engineering of Thin Films**

Strain engineering is a powerful and accessible way to manipulate the properties of functional oxide thin films. For instance, a lot of works have been done to investigate the effect of strain on the structure and properties of  $ABO_3$  perovskite. Generally,  $ABO_3$  perovskite consists of cubic sub-lattices of A and B cations. The B cations are coordinated by oxygen anions forming an octahedral structure, as shown in Figure 1.3. Ideally,  $ABO_3$  perovskite has standard cubic symmetry with  $Pm3m$  space group. However, the structure of  $ABO_3$  perovskite can easily be distorted, and many different functionalities can result from these different distortions. Figure 1.3 shows three main structural distortions in perovskites. The polar displacement of B cations, rigid rotation of octahedral  $BO_6$  units and Jahn-Teller distortions of the  $BO_6$  octahedra are shown in Figure 1.3 (a), (b), and (c) respectively.<sup>10</sup> Polar displacement of B cations in Figure 1.3 (a) can be associated with ferroelectricity because the displacement of B cations creates dipole moment in each unit cell, which can be switched and retained by applying electric field. Rigid rotation and Jahn-Teller distortions of  $BO_6$  octahedra is associated with magnetic coupling that can either lead to enhancement or suppression of

ferromagnetism, depending on the orbital hybridization of the materials involved.

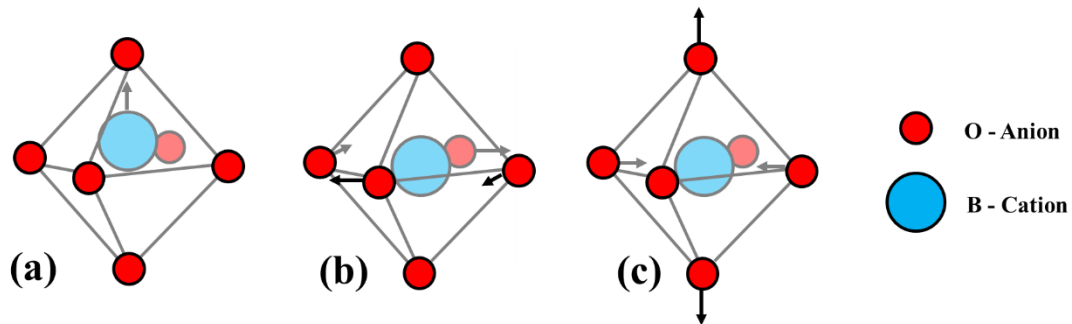


Figure 1.3 Common perovskite distortion modes. (a) Polar displacement of B-site cations; (b) rigid rotation of the  $\text{BO}_6$  octahedra, and (c) Jahn-Teller distortion of the  $\text{BO}_6$  octahedra.

The understanding of octahedral rotations is very important to investigate the strain effect in magnetic materials. For example, it has been shown that the tensile strain in  $\text{LaCoO}_3$  magnetic films stabilizes the intermediate or high spin states and that the lattice distortion will increase the paramagnetic effective moment.<sup>11-12</sup> As the  $\text{LaCoO}_3$  film undergoes tensile strain, the bonding angle between Co-O-Co gradually increases from bulk value of  $163^\circ$  toward  $180^\circ$  which leads to stronger hybridization of Co 3d and O 2p orbitals. This hybridization favours ferromagnetic coupling between the orbitals.

Another example of study on strain engineering in oxide materials was done by Adamo *et al.* In their work, epitaxial  $\text{La}_{0.7}\text{Sr}_{0.3}\text{MnO}_3$  (LSMO) thin films were deposited using molecular beam epitaxy (MBE) on various single crystal substrates with different lattice parameters to induce different level of epitaxial strain. The *out-of-plane* ( $\epsilon_{zz}$ ) lattice strain as a function of the *in-plane* ( $\epsilon_{xx}$ ) lattice strain on LSMO thin film is shown on Figure 1.4. Different magnetic behaviors of the films were observed for different level of substrate-induced strains.<sup>13</sup> For instance, a decreasing trend of ferromagnetic  $T_c$  was observed by varying the substrate-induced biaxial strain from compressive ( $-2.3\%$ ) strain to tensile ( $+3.2\%$ ) strain. Contrary to the trend of  $\text{LaCoO}_3$ , the tensile strain in LSMO will increase the Jahn–Teller distortion of the  $e_g$  electron levels which results in weaker orbital hybridization and thus a decrease in  $T_c$ .

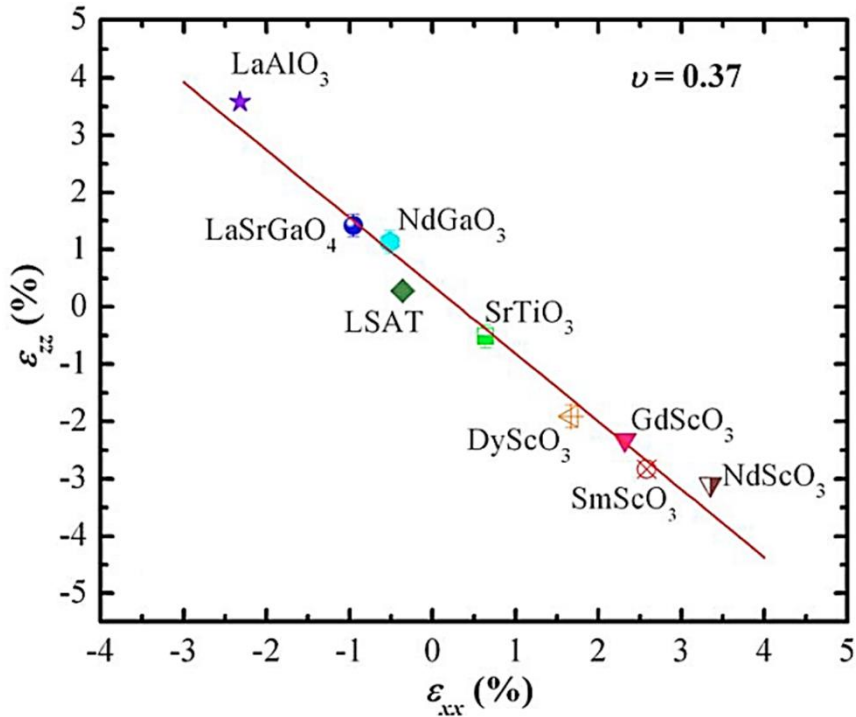


Figure 1.4. The *out-of-plane* ( $\epsilon_{zz}$ ) lattice strain as a function of the *in-plane* ( $\epsilon_{xx}$ ) lattice strain. The value of out-of-plane strain was calculated based on the Poisson ratio of  $\text{La}_{0.7}\text{Sr}_{0.3}\text{MnO}_3$  (LSMO). (Figure from <sup>13</sup>)

In any perovskites, the three distortion modes in Figure 1.3 energetically compete with each other and the most stable one in ground state will play a dominant role in physical properties. These structural instabilities typically include long-range cooperative displacements of atoms in the crystal, as shown in Figure 1.5.

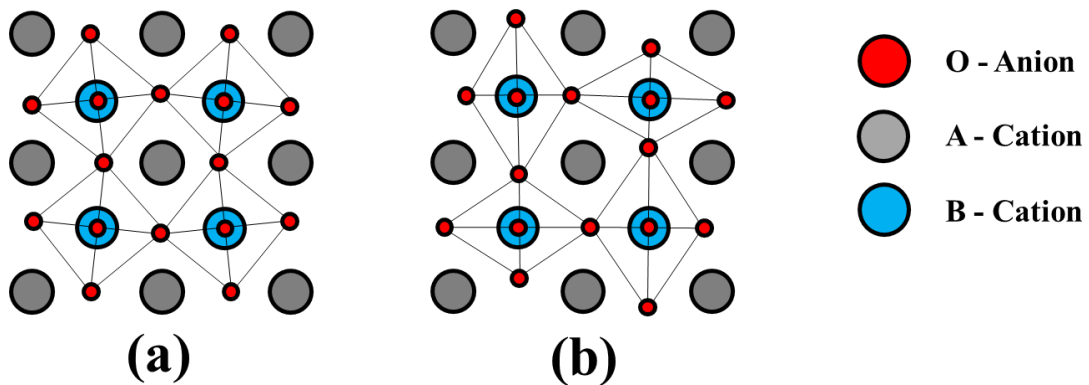


Figure 1.5 Lattice diagram of (a) the octahedral rotations and (b) the Jahn-Teller distortion. The A cations are shown in black, B cations are shown in blue and oxygen atoms shown in red.

Similar to magnetic properties, studies have been done on strain effect from substrate on ferroelectricity as well.<sup>14</sup> A diagram showing pseudo-cubic lattice parameters was summarized in Figure 1.6 for perovskite and perovskite-related thin film growth. The upper part of the figure shows commonly-grown perovskite oxides while the lower part of the figure shows commonly-used crystal substrate for thin film growth. Ferroelectric properties are measured by spontaneous polarizations which are very sensitive to even small values of strain. It has been reported that strain on the order of 1% can lead to large enhancement of the ferroelectric transition temperature (increasing ferroelectric  $T_c$ ) and coercive field in ferroelectric materials.<sup>15-17</sup> In addition, it was reported that bi-axial strain results in switchable polarizations either parallel or perpendicular to the plane of epitaxy which leads to stabilization of the incipient ferroelectric properties in thin films form.<sup>18</sup>

Strain engineering is particularly useful for ferroelectric applications because it can be used to tune  $c/a$  ratio which is the primary parameter determining the magnitude of saturation polarization and ferroelectric  $T_c$ . In the past years, lots of efforts have been spent not only to achieve strained epitaxial film but also to obtain low defect heterostructure thin films. For example, buffer layers are used in the case where the lattice mismatch between film and substrate is very big. The use of buffer layer is primarily to reduce the level of internal stress accumulated in the thin films, which also means less dislocations to accommodate the internal stress. It is important to note that the residual strain due to incomplete strain relaxation in the buffer layer may act as the seed for additional defects during the subsequent film growth.<sup>19-20</sup>

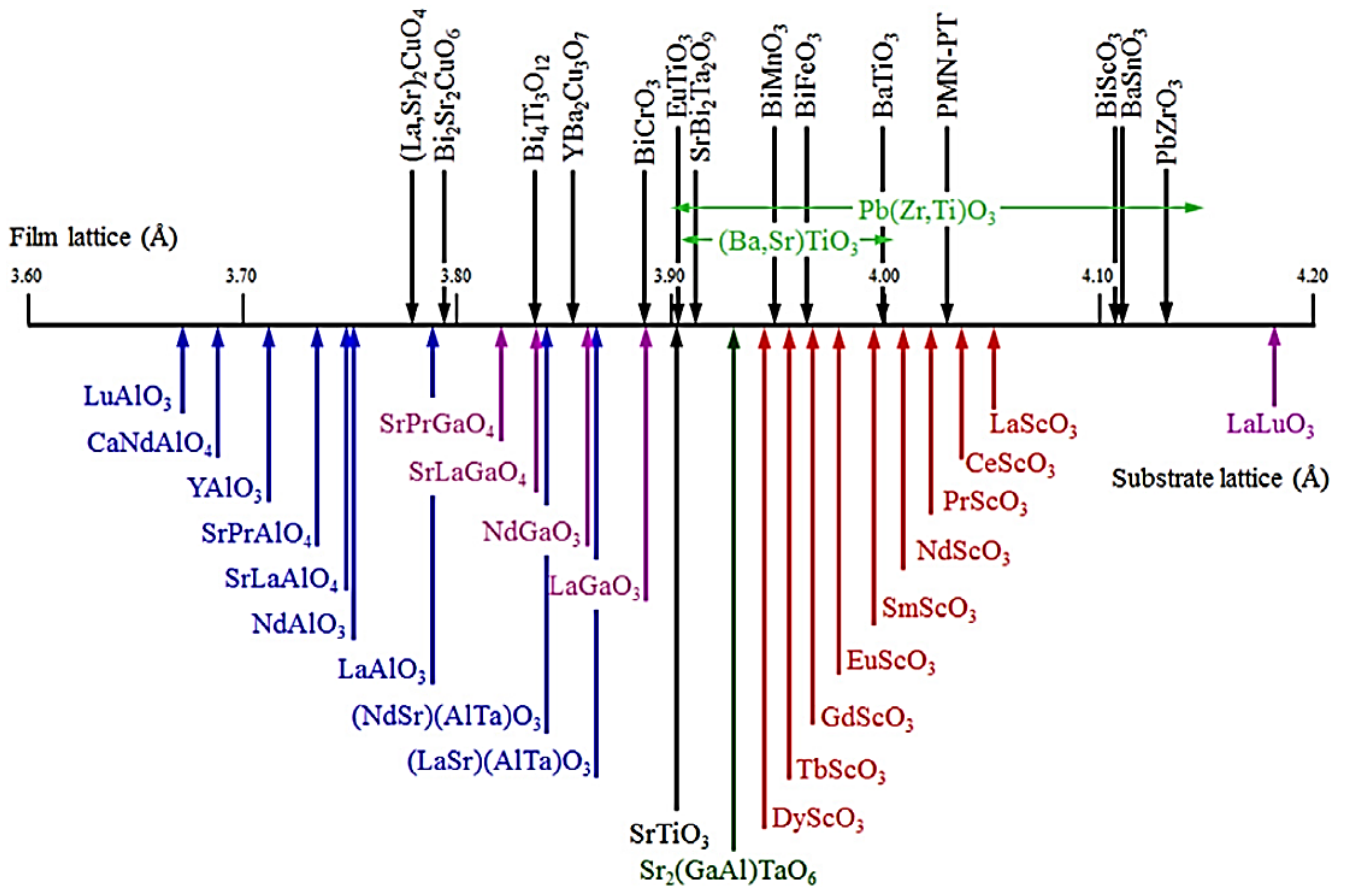


Figure 1.6 Pseudo-cubic lattice parameter of perovskite and perovskite-related oxide thin films and substrates. Black arrows represent commonly grown perovskite thin films, blue arrows represent Al-based substrates, purple arrows represent Ga-based substrates, and red arrows represent Sc-based substrates (Figure from <sup>21</sup>)

Apart from ferromagnetic and ferroelectric properties, exciting results have also been found in strained superconductors where strain can be used to increase the superconducting  $T_c$  of  $\text{La}_{2-x}\text{Sr}_x\text{CuO}_4$  films when grown on different substrates with either compressive or tensile strain. (in this particular case, compressive and tensile strain results in increased superconducting  $T_c$ ).<sup>22</sup>

In addition to strain engineering using crystal substrates with various lattice parameters (layered heterostructures), superlattices are another effective way to control strain in oxide thin films. Superlattices consists of periodic structures of layers of two (or more) materials with a typical layer thickness being from a unit cell ( $< 1\text{nm}$ ) to a few nanometers. In superlattices, the *in-plane* lattice parameter of all the constituents is

fully strained to that of the substrates and the primary factor that determines the physical properties of the superlattice is the elastic strain from the substrates. Some superlattice systems that have been intensively studied of recent times are (001)  $\text{PbTiO}_3$ /(001)  $\text{SrTiO}_3$  and (001)  $\text{BaTiO}_3$ /(001)  $\text{SrTiO}_3$  superlattices to investigate the effect of strain on thin layers of the ferroelectric materials. The HRTEM images of these superlattices are shown in Figure 1.7.<sup>1</sup>

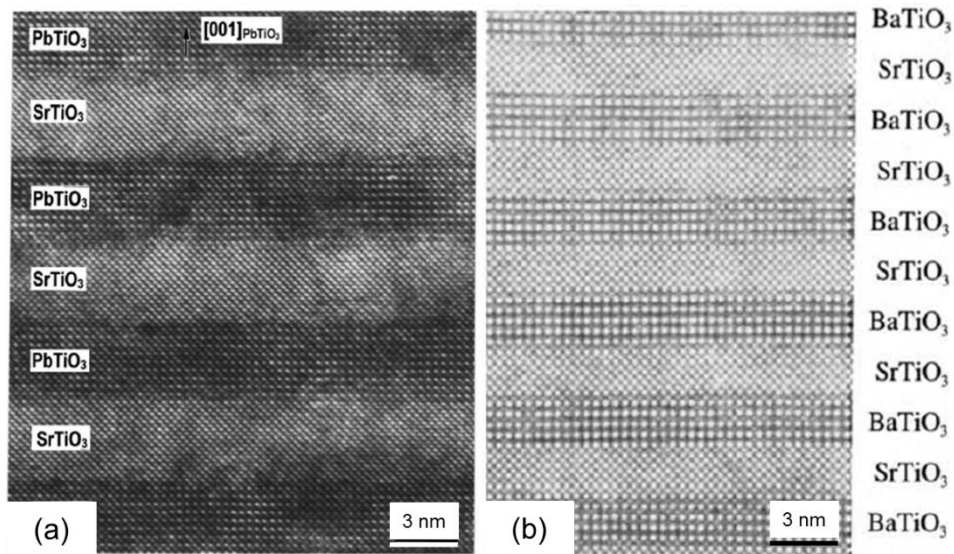


Figure 1.7 HRTEM images of (a)  $\text{PbTiO}_3$ / $\text{SrTiO}_3$  and (b)  $\text{BaTiO}_3$ / $\text{SrTiO}_3$  superlattices grown by MBE.(Figure (a) from <sup>23</sup> , figure (b) from <sup>1</sup>)

More recently, Tenne *et al.* reported the growth of the (001)  $\text{BaTiO}_3$ /(001)  $\text{SrTiO}_3$  superlattice on the (001)  $\text{SrTiO}_3$  substrate by molecular beam epitaxy (MBE).<sup>24</sup> The ferroelectric  $T_c$  of the MBE grown superlattice is shown in Figure 1.8. The thickness of the  $\text{BaTiO}_3$  layer in the superlattice varied from 1 to 8 unit cells and the thickness of the (001)  $\text{SrTiO}_3$  spacer layer was fixed to be either 4 (solid blue plot) or 13 (solid red plot) unit cells. For a fixed number of unit cells in  $\text{SrTiO}_3$  (m), as the number of unit cells in each of the  $\text{BaTiO}_3$  increases (thicker layer), the dipole coupling between each ferroelectric  $\text{BaTiO}_3$  layer gets stronger, and hence results in increase of the ferroelectric  $T_c$ . Likewise, for a fixed number of unit cells of  $\text{BaTiO}_3$  (n), as the  $\text{SrTiO}_3$  layer becomes thicker, the dipole coupling between each  $\text{BaTiO}_3$  layer gets weaker,

resulting in a lower ferroelectric  $T_c$  (as shown in the blue vs red plot in Figure 1.8). In short, both experimental results and first-principle calculations of the superlattice showed a significant increase of the ferroelectric  $T_c$  in a multi-domain state (thicker layer or thinner inter-layer spacing) instead of single-domain state by varying the thicknesses of  $\text{BaTiO}_3$  and  $\text{SrTiO}_3$  interlayer in the superlattice.<sup>1</sup>

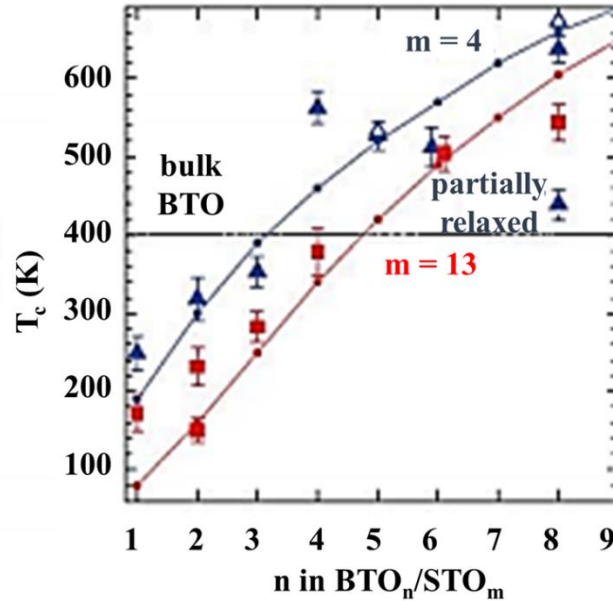


Figure 1.8 The dependence of ferroelectric  $T_c$  on  $n$  and  $m$  in  $(\text{BaTiO}_3)_n/(\text{SrTiO}_3)_m$  superlattices. The blue symbols and solid blue line are for  $m = 4$  and red symbols and solid red line are for  $m = 13$ . (Figure from <sup>1</sup>)

Layered heterostructures and superlattices are not the only architectures of strain controllable oxide thin films. A new oxide thin film architecture in the form of vertically aligned nanocomposite (VAN) thin films offer a different approach to strain control.<sup>3-4</sup> An example of VAN is epitaxial pillars of magnetic oxides in a thin film ferroelectric matrix which results in electrical coupling of ferromagnetic properties through magnetostriction.<sup>3, 25</sup> Since the main focus of this thesis is to discuss physical properties coupling and enhancement via strain coupling in VAN films, a detailed introduction to VAN will be separately presented in the next section.

## 1.2. Vertically Aligned Nanocomposite (VAN)

Vertically aligned nanocomposites (VAN) are a relatively new and promising architecture that can be used to control strain levels in oxide thin films.<sup>4, 26-28</sup> A schematic of a VAN film is shown in Fig. 1.9. In VAN films, two phases are self-assembled to form a vertical structure, either as nano-pillars embedded in a matrix or in a checkerboard structure.

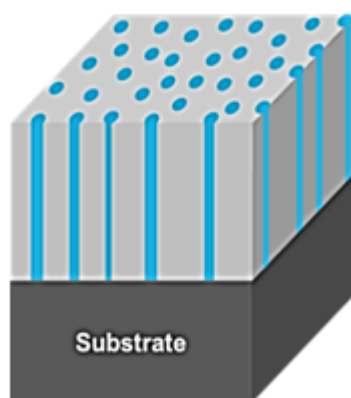


Figure 1.9. Schematic diagram showing an example vertically aligned nanocomposite structure. (Figure from <sup>29</sup>)

Both phases are heteroepitaxially grown on the given substrate while the vertical interfaces between both phases maintain certain epitaxial relationship as well, depending on their vertical lattice matching. The VAN thin film system exhibits many interesting physical properties with its unique microstructure. It promises a novel way of achieving multi-functionality and tunable strain which is very different from the situation for conventional single-phase thin films.

One unique feature of the VAN structure is that unlike conventional thin films, the strain level in the VAN structure is not limited by its thickness. In fact, high strain levels are reported for films with thickness up to  $> 1 \mu\text{m}$ , something that would not be possible in any single-phase thin film.<sup>27, 30</sup> The reason for this is that the strain states in VAN structure originated from the vertical interface epitaxy between the phases involved with minimum influence from the substrate.

Besides strain, novel cross-coupling of functional properties over the large vertical interfacial areas can be achieved using this architecture. For instance, multiferroicity can be achieved by pairing ferromagnetic-ferroelectric phases in the VAN structure.<sup>31-43</sup>

Historically, the first work that led to the discovery of VAN was a mixed phase film of LCMO ( $(\text{La}_{0.7}\text{Ca}_{0.3}\text{MnO}_3)_{1-x}(\text{MgO})_x$ ) reported by Moshnyaga *et al* in 2003.<sup>44</sup> These thin films did not have a clean VAN structure but instead contained poorly oriented LCMO grains coated with MgO. The films were grown by a solution based technique called metal-organic aerosol deposition (MAD) and the initial objectives were to demonstrate the phase transition and tunable magneto-transport properties in the LCMO phase. Albeit not vertically aligned, this work laid an important foundation to physical properties coupling through the use of oxide nanocomposites.

The first ever reported VAN structure was by Zheng *et al.* on  $\text{BaTiO}_3\text{-CoFe}_2\text{O}_4$  (BTO-CFO) nanocomposite. The work was inspired by the early development of  $\text{BaTiO}_3\text{-CoFe}_2\text{O}_4$  (BTO-CFO) bulk composites. The coupling between ferroelectric and ferromagnetic properties was achieved by vertically aligned nanostructures of epitaxial  $\text{CoFe}_2\text{O}_4$  magnetostrictive spinel pillars embedded in a ferroelectric  $\text{BaTiO}_3$  perovskite matrix.<sup>3</sup> Subsequently, many studies have been undertaken on self-assembled perovskite VAN architecture to achieve multi-ferroic coupling such as in  $\text{BiFeO}_3\text{-CoFe}_2\text{O}_4$ ,<sup>31-33, 35-38, 45</sup>  $\text{BiFeO}_3\text{-NiFe}_2\text{O}_4$ ,<sup>39-40</sup> and  $\text{PbTiO}_3\text{-CoFe}_2\text{O}_4$  systems.<sup>41-43</sup> All these studies were aimed at exploiting the strong coupling between ferromagnetic and ferroelectric properties in the nanocomposite through strain.

Figure 1.10 shows an example of a typical VAN structure. TEM images of  $(\text{BaTiO}_3)_{0.5} - (\text{Sm}_2\text{O}_3)_{0.5}$  (BTO- $\text{Sm}_2\text{O}_3$ ) with both planar (Figure. 1.10 (a)) and cross-section (Figure. 1.10 (b)) of the film shows a clear vertical alignment of nanopillars and matrix. Nanopillars of  $\text{Sm}_2\text{O}_3$  are embedded in a matrix structure of  $\text{BaTiO}_3$ . This is just one of several possible self-assembled structures. More details regarding other possible structures will be shown in the later section.

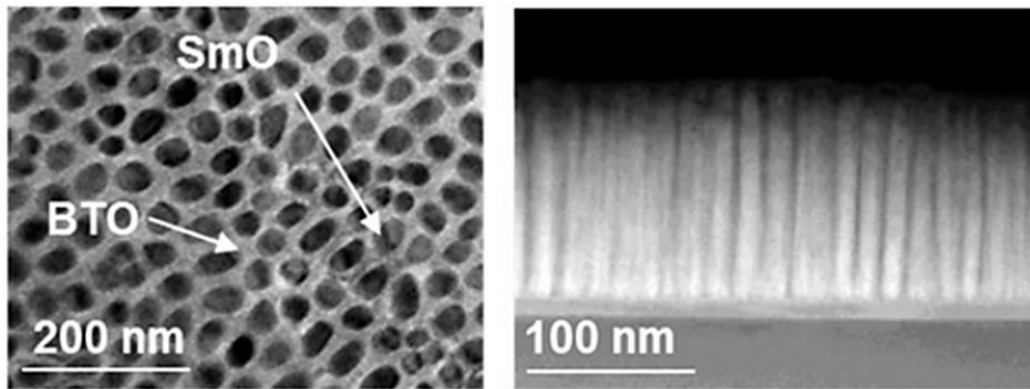


Figure 1.10. TEM images showing an example of real VAN structure from top view (left) and lateral view (right). On the left part of the figure, BaTiO<sub>3</sub> (BTO) forms the matrix while Sm<sub>2</sub>O<sub>3</sub> (Sm<sub>2</sub>O<sub>3</sub>) forms the nano-pillar with lateral dimension of about 20 nm. The lateral view of the TEM image shows well-aligned and low tilting angle of the nano-pillars in the VAN structure. (Figure from <sup>29</sup>)

VAN architectures are interesting not only for achieving multi-functionality, but can also be exploited for enhancing a single functionality through strain manipulation of one of the phases by another. Enhancement of functionality by strain has been widely reported for horizontal (*in-plane*) strain thin films. For instance, strain field perturbed ferroelectricity.<sup>46</sup> Large improvements in the ferroelectric Curie temperature, remnant polarization and structural phase transition temperature have been demonstrated in SrTiO<sub>3</sub> and BaTiO<sub>3</sub> through use of substrate-controlled, coherent in-plane biaxial strain.<sup>18, 47</sup> In VAN, some of the successfully grown films such as BaTiO<sub>3</sub>-Sm<sub>2</sub>O<sub>3</sub>,<sup>30</sup> (Ba<sub>0.60</sub>Sr<sub>0.40</sub>TiO<sub>3</sub>)<sub>1-x</sub>(Sm<sub>2</sub>O<sub>3</sub>)<sub>x</sub> (BSTO- Sm<sub>2</sub>O<sub>3</sub>),<sup>48</sup> BiFeO<sub>3</sub>-Sm<sub>2</sub>O<sub>3</sub>,<sup>4, 49-52</sup> BiFeO<sub>3</sub>-Fe<sub>2</sub>O<sub>3</sub>,<sup>25</sup> and BiMnO<sub>3</sub>-Sm<sub>2</sub>O<sub>3</sub><sup>53</sup> have shown unprecedented improvement in properties through strain coupling in nanocomposite films such as obtaining high Curie temperature,<sup>30</sup> improving tunability,<sup>48</sup> reducing dielectric loss,<sup>52</sup> enhancing multiferroic coupling,<sup>54</sup> and achieving photostriction-magnetic coupling.<sup>55</sup>

Besides coupling ferroelectricity with magnetism, nanocomposites have also been developed for tunable microwave devices using ferroelectric and dielectric phases.

Some popular combination of ferroelectric and low permittivity oxides are  $\text{Ba}_{0.60}\text{Sr}_{0.40}\text{TiO}_3\text{-MgO}$ ,<sup>56-58</sup>  $\text{Ba}_{0.60}\text{Sr}_{0.40}\text{TiO}_3\text{-TiO}_2$ ,<sup>59-60</sup>  $\text{Ba}_{0.50}\text{Sr}_{0.50}\text{TiO}_3\text{-Al}_2\text{O}_3$ ,<sup>61</sup> and  $\text{BaTiO}_3\text{-CeO}_2$ .<sup>62-63</sup>

A summary of oxide VAN materials investigated so far is presented in Table 1.1. The presentation of the table is classified based on the resulting physical properties (e.g. superconductivity, ferroelectricity, etc) in relation to the coupling mechanism in the VAN structure (e.g. vertical strain control, vertical interface coupling, etc) as well as crystal structure (e.g. perovskite).

<b>Vertically Aligned Nanocomposite Characteristics</b>	<b>Defect Engineering</b>	<b>Vertical strain control</b>	<b>Strong Coupling Effects</b>	<b>Vertical Heterointerface</b>	<b>Vertical Strain Control and Coupling</b>
Nanocomposite family	Superconductivity	Ferroelectricity	Multiferroicity	Electronic and ionic transport	Dielectric and optical effects
Perovskite-related	-BaZrO <sub>3</sub> -YBa <sub>2</sub> Cu <sub>3</sub> O <sub>7-δ</sub> (YBCO) <sup>64</sup> -BaSnO <sub>3</sub> -YBCO <sup>65</sup> -BaHfO <sub>3</sub> -YBCO <sup>66</sup> -Ba <sub>2</sub> YTaO <sub>6</sub> -YBCO <sup>67</sup> -Ba <sub>2</sub> YNbO <sub>6</sub> -YBCO <sup>68</sup>	-BaTiO <sub>3</sub> -Sm <sub>2</sub> O <sub>3</sub> <sup>69</sup> -BaTiO <sub>3</sub> -CeO <sub>2</sub> <sup>70</sup> -BiFeO <sub>3</sub> -Sm <sub>2</sub> O <sub>3</sub> <sup>71</sup>	-BiFeO <sub>3</sub> -CoFe <sub>2</sub> O <sub>4</sub> <sup>32</sup> -BaTiO <sub>3</sub> -CoFe <sub>2</sub> O <sub>4</sub> <sup>3</sup> -BiFeO <sub>3</sub> -NiFe <sub>2</sub> O <sub>4</sub> <sup>72</sup> -La <sub>2</sub> CoMnO <sub>6</sub> -ZnO <sup>54</sup>	-La <sub>0.7</sub> Sr <sub>0.3</sub> MnO <sub>3</sub> (LSMO)-ZnO <sup>73</sup> -LSMO-CeO <sub>2</sub> <sup>74</sup> -LSMO-Mn <sub>3</sub> O <sub>4</sub> <sup>75</sup> -LSMO-NiO <sup>76</sup> -La <sub>1-x</sub> Ca <sub>x</sub> MnO <sub>3</sub> -MgO <sup>77</sup> -SrTiO <sub>3</sub> -Sm <sub>2</sub> O <sub>3</sub> <sup>78</sup> -SrRuO <sub>3</sub> -ZnO <sup>79</sup>	-Ba <sub>0.6</sub> Sr <sub>0.4</sub> TiO <sub>3</sub> -Sm <sub>2</sub> O <sub>3</sub> <sup>80</sup> -SrRuO <sub>3</sub> -CoFe <sub>2</sub> O <sub>4</sub> <sup>81</sup>
Layered oxides			-Bi <sub>5</sub> Ti <sub>3</sub> FeO <sub>15</sub> -CoFe <sub>2</sub> O <sub>4</sub> <sup>73</sup>		

Table 1.1. Epitaxial nanocomposite heterostructures grouped by VAN coupling characteristics, functionality as well as crystal structure.

As presented in Table 1.1., the range of functionality that can be studied using VAN architectures is very broad. More exciting possibilities can be further explored by broadening the scope of VAN structure to include not only oxide, but metals and possibly polymers. More recently, VAN structures consisting of separate metal and oxide phases were successfully fabricated by PLD.<sup>82-83</sup> In summary, the development of the self-assembled VAN architectures represents an exciting new thin film form for achieving unprecedented property enhancements and new mutli-functionalities.

### 1.2.1 Materials Selection Criteria for VAN

The first thing to consider when selecting the phases to be fabricated for VAN is the solubility limit of the respective phases. Generally, inter-diffusion between the two phases in the nanocomposite can be minimized through careful selection of materials with low mutual solid solubility (in this case, solid insolubility is good to minimize mixing). Through systematic studies done on VAN for materials selection in growing self-assembled nanocomposites, MacManus-Driscoll *et al.* presented simple guidelines and characteristics<sup>4, 28</sup> as follows:

- One or both phases in the nanocomposites should be able to grow epitaxially on the single crystal substrate. These phases are not necessarily the phases that are present in the target material (e.g. PLD or sputtering target). Instead, phases with lowest lattice mismatch with the underlying single crystal substrate are generally more thermodynamically favored to grow.
- The two phases involved should be immiscible with each other.
- Both phases should have similar growth kinetics at the chosen growth temperature.
- Cations with large differences in ionic radii are important to prevent intermixing between the two phases.
- Finally, a difference in elastic modulus is required to achieve strain control on one phase by the stiffer phase.<sup>4</sup>

### 1.2.2. Growth Mechanisms for VAN

The nucleation and growth of self-assembled nanocomposites has been extensively studied in organic block copolymers, metals and semiconductor systems<sup>84-86</sup> but not widely before for oxide thin films. Before going into discussion of the growth of VAN structures, a general widely accepted mechanisms for thin films growth will be discussed. The three widely accepted mechanisms of thin film growth namely island growth (Volmer-Weber growth), layer-by-layer growth (Frank-Van der Merwe growth) and island-layer growth (Stranski-Krastanov growth).<sup>87-89</sup> Figure 1.11 shows the schematic of the respective growth modes. These models are all based on interfacial energy between ad-atoms with ad-atoms and ad-atoms with substrate. Volmer–Weber

growth occurs when the clusters forms on the substrate and grow into three-dimensional island features. A simple explanation for this growth is that the atoms deposited have stronger bond with each other than to the substrate. This happens when the substrate and film are of different materials. Frank-Van der Merwe growth is the opposite of Volmer-Weber growth. In this mode of growth, atoms formation occurs layer by layer. In this mode, the depositing atoms have stronger bond to the substrate than with each other. Besides, it typically occurs at relatively low growth rate and high temperature. This is the ideal mode for all epitaxial growth of thin films. Lastly, Stranski-Krastanov (S-K growth) mode is the combination of island and layer by layer modes. Initially the film grows by layer by layer mode but after a while, it becomes energetically unfavorable and island growth modes prevails.

In order to form an epitaxial film, layer-by-layer growth is more favorable. On the other hand, for vertically aligned nanocomposites, the growth mechanism more closely resemble island growth of two separate phases.<sup>90</sup>

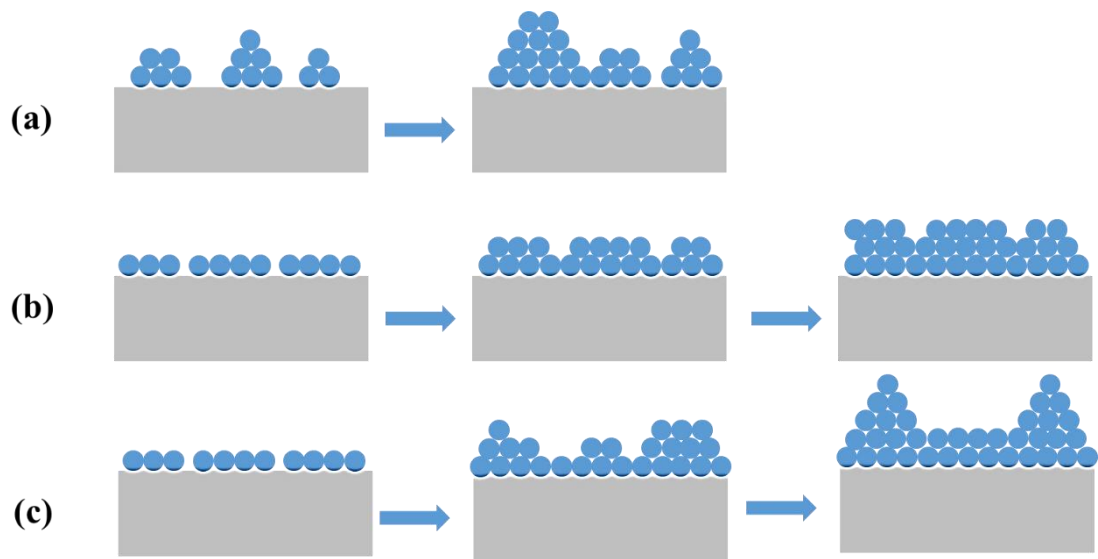


Figure 1.11 Typical growth modes (a) Volmer-Weber (island), (b) Frank-Van der Merwe (layer-by-layer), and (c) Stranski-Krastanov growth. (Figure from <sup>91</sup>)

Figure 1.12 shows the schematic diagram of what happens during the initial stage of nucleation. First, a nucleus forms on a substrate. The wettability of the island on the

substrate is defined by the difference in interfacial energy between substrate-vapor ( $\gamma_{sv}$ ) and film-substrate ( $\gamma_{fs}$ ) which results in the observed wetting angle,  $\theta$  between the film-vapor ( $\gamma_{fv}$ ) and film-substrate.

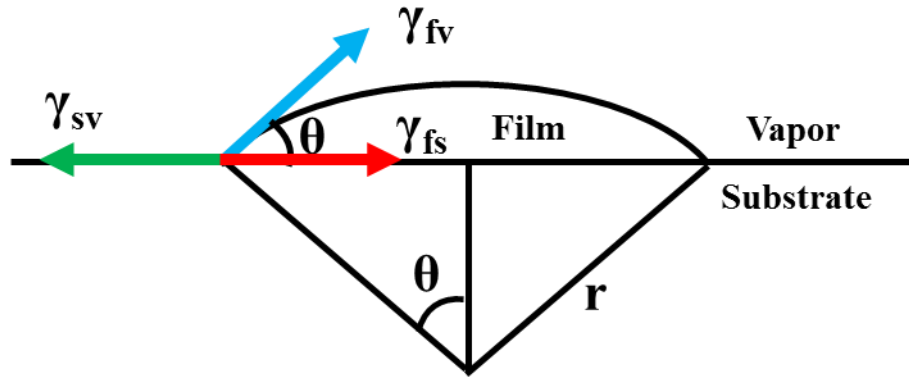


Figure 1.12 Cluster nucleation during deposition process.

The wetting angle is directly related to interfacial energy by the following equation:

$$\gamma_{sv} = \gamma_{sf} + \gamma_{fv} \cos \theta \quad (1.5).$$

From equation (1.5), the higher the difference in interfacial energy between  $\gamma_{sv}$  and  $\gamma_{sf}$ , the lower the wetting angle will be and vice versa. Thermodynamically, a big difference in interfacial energy means the substrate-film formation energy is much lower compared to the substrate-vapor energy, thus it is energetically favorable for ad-atoms to wet the substrate and spread more evenly. Figure 1.13 shows some examples of the possible VAN structures. In short, phase formation in the films is a function of both thermodynamic and epitaxial stability.

In VAN structures, there are generally two types of growth that contribute to its vertical structure namely nucleation and growth and spinodal decomposition. In nucleation and growth modes, species forming different phases coalesce into nuclei on the surface of the substrate during the initial stage of deposition followed by subsequent arrival of the same atomic species, forming vertical pillar. In spinodal decomposition however, atomic species from both phases are deposited simulatenously on the substrate

as solid solution, followed by phase-separation upon cooling from deposition temperature (typically 700 – 800 °C). In Figure 1.13, different textures such as horizontal, vertical, or mixed alignment phase-separated structures have been grown epitaxially using either nucleation and growth or spinodal decomposition.<sup>28</sup>

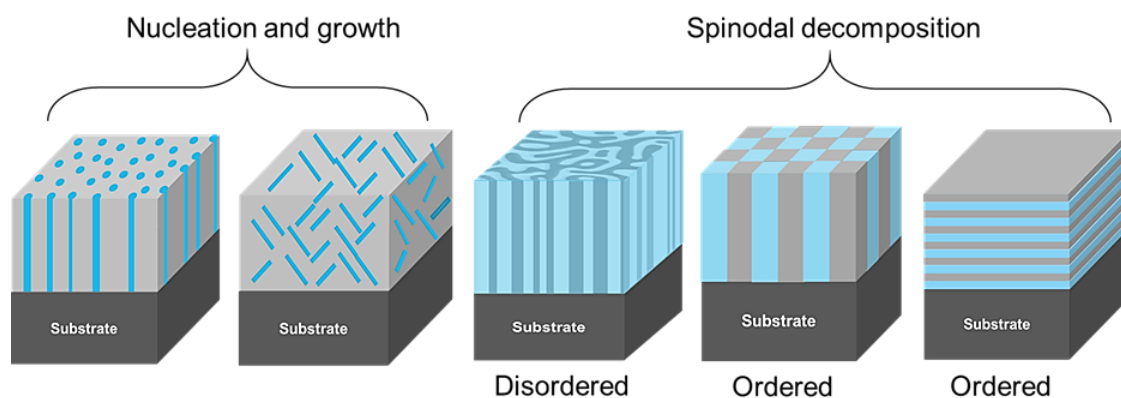


Figure 1.13. Schematic structures of various nanocomposite architectures categorized by its growth mechanisms as well as ordered/disordered nature of the structure. (Figure from <sup>29</sup>)

How the phases are distributed depends both on the vertical interface and on horizontal (between substrate and film phase) epitaxial stabilization, kinetics, and the ratios of the two phases.<sup>92</sup> For epitaxially directed self-assembly, it is desirable that one phase in the film is crystallographically matched to the substrate so that it can nucleate and grow epitaxially. This phase has the tendency to form the matrix, even if it is the slight minority phase. The second phase does not need to have good crystallographic matching with the substrate, but instead it is stabilized by the epitaxial strain from vertical interface with the matrix phase. This phase normally forms the pillar phase. In other words, depending on surface energy considerations and the relative concentrations of the two components in the film, the pillar phase may or may not seed its growth on the substrate.

With sufficient kinetics and material fraction, the pillar phase always aligns vertically with the matrix forming vertical interfaces with little intermixing. The matrix and pillar can both be functional phases whose functional properties are of interest.

Here, the phases couple to one another via strain or charge-coupling of properties at the interfaces.<sup>3, 54-55</sup> Alternatively, just one of the phases may be the active phase with functional properties, with the other phase being the passive, strain controlling phase, acting simply to mechanically stabilize or tune the strain state of the active phase.<sup>30</sup>

For nucleation and growth, largely immiscible materials need to be chosen, whereas the opposite is true for spinodal decomposition. In the spinodal case, solid-solution mixing is required at high temperature, followed by one of the phases separating out of the solid solution upon cooling. The schematic phase diagram showing miscibility gap, is shown in Figure 1.14, highlighted in the shaded area.

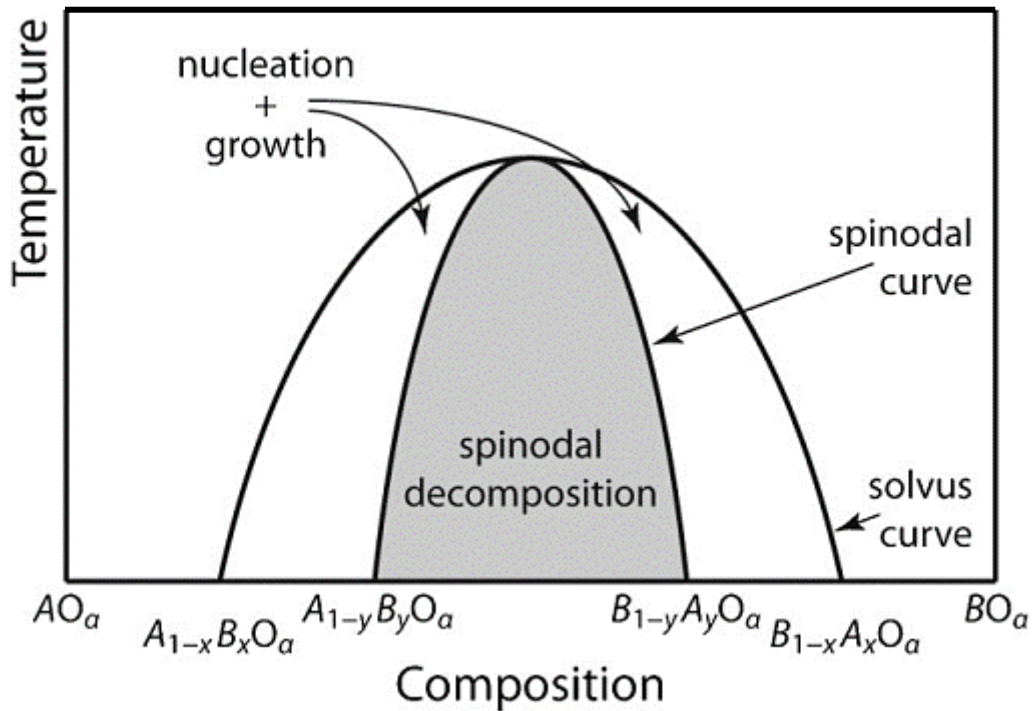


Figure 1.14 Energy diagram showing miscibility gap that facilitates spinodal decomposition. (Figure from <sup>28</sup>)

For example, one can select a starting composition with the correct mixture of A and B species. Upon cooling, both of the species are no longer solid soluble with each other, thus forming separate phases,  $A_{1-y}B_yO_a$  and  $B_{1-y}A_yO_a$ . A and B here represent metal/rare-earth elements. Whether a laterally or vertically ordered spinodally

decomposed structure or random one forms depends on the crystallographic relation between the decomposing phases, and between the phases and the substrate, as well as their growth kinetics.<sup>93</sup> Hence, if the phases are crystallographically similar and sufficient time (e.g. slow growth rate) is allowed for epitaxial growth arrangements, spatially ordered structures can form. Conversely, if phases are structurally dissimilar or if insufficient time is allowed for separation (e.g. fast growth rate), large-area disordered structures form.<sup>94</sup> It is worth noting that to date, only few ordered spinodal structures have been achieved in electronic materials.<sup>95-96</sup> On the other hand, in Figure 1.14, for nucleation and growth to happen, the starting mixture at high temperature must fall outside the  $A_{1-y}B_yO_\alpha - B_{1-y}A_yO_\alpha$  composition range. This will result in the nucleation of a mixture of  $A_{1-x}B_xO_\alpha$  and  $A_{1-y}B_yO_\alpha$  or  $B_{1-y}A_yO_\alpha$  and  $B_{1-x}A_xO_\alpha$  phases, depending on starting composition.

The process for nucleation and growth for VAN structure is schematically shown in Figure 1.15. Initially, islands of phase containing A cation and phase containing B cation nucleate alternately and spread throughout the entire substrate. Subsequently, due to lower interfacial energy between like atomic species in both phases, ad-atoms of A and B will preferentially grow on existing phase containing A and B cations, respectively. This results in formation of VAN films. From an interfacial energy point of view, it can be deduced that the interfacial energy controls the column width as well. During the initial stage of island formation, if the difference between the interfacial energy of substrate-vapor and substrate-film is small, the wetting angle will be larger, leading to smaller islands spread across the substrate and vice versa. Smaller islands means the resulting column width will also be smaller as well. In other words, the closer the interfacial energy between substrate-island to substrate-vapor, the smaller will be the column width.

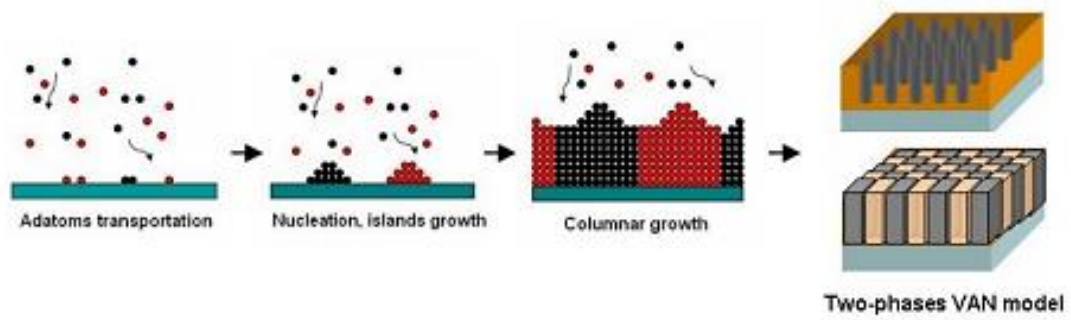


Figure 1.15 Schematic illustration of the growth process of vertically aligned nanocomposite. (Figure from <sup>97</sup>)

# Chapter 2 Fabrication Process

## 2.1. Thin Film Deposition Techniques

Many oxide thin films deposition techniques involve use of a vacuum. For vacuum-based deposition techniques, there are basically two types of thin films deposition, either through physical process in physical vapor deposition (PVD), such as evaporation method, or through chemical methods in chemical vapor deposition (CVD), such as gas- and liquid-phase chemical process. There are also a number of processes that combine physical and chemical reactions such as glow discharges and reactive sputtering.

For physical vapor deposition (PVD), techniques such as electron-beam evaporation, molecular beam epitaxy (MBE), pulsed laser deposition (PLD) and sputtering are widely used to achieve high film quality. Those techniques come with relatively simple set up and can give good surface coverage and smooth surface. PVD techniques can be used to grow almost all materials and can generally provide good film stoichiometry for complex materials, given the right growth condition. Chemical vapor deposition (CVD) techniques on the other hand, depend mainly on chemical reactions and surface absorptions during deposition. In CVD systems, vapor gases (precursors) are introduced into the deposition chamber before undergoing reaction on or near the surface of the substrate that results in film formation. Based on the pressure level as well as chemical species involved, CVD techniques can be generally classified into low-pressure CVD, plasma-enhanced CVD, metal-organic CVD and atomic layer deposition (ALD). Generally in vacuum deposition systems, the film density, microstructures, stoichiometry as well as other properties can be controlled by adjusting the deposition parameters.

Besides the vacuum based techniques, there are other thin films deposition techniques such as liquid phase epitaxy (LPE) and solution-based techniques (sol-gel and polymer assisted deposition). These techniques are cost effective because they do not require vacuum system. They are widely used in more scalable applications where the film microstructure is not of paramount importance.

Our study will focus mainly on PLD as well as sputtering. PLD is the one of the most popular methods for oxide thin film growth due to the high quality epitaxy that it can produce as well as relatively faster process as compared to MBE or RF sputtering. Sputtering, on the other hand, generally offers more scalable growth of thin films and has much better thickness uniformity over large area as compared to PLD. However, it is not a popular method for growing VAN thin films due to the generally lower epitaxial film quality as compared to PLD. The subsequent sections in this chapter will present an overview of PLD as well as sputtering separately. The similarities and differences between the two methods will be compared in the later part of this dissertation (chapter 6).

## 2.2 Pulsed Laser Deposition (PLD)

Pulsed laser deposition (PLD) is a vacuum based physical vapor deposition process that has some similarities to molecular beam epitaxy (MBE) and some with sputter deposition. PLD is popular mainly due to its simple set-up for its vacuum system (thus enabling the versatility in using multiple vacuum chambers that share one laser source through beam-splitter), stoichiometric deposition of films with multi-components under optimized conditions, fine control of thin film deposition in terms of film surface and crystallinity as well as possibility of integration with characterization equipments such as reflection high-energy electron diffraction (RHEED) and x-ray photoelectron spectroscopy (XPS). This section gives an overview of PLD process as well as important deposition parameters that can be controlled in PLD from sub-section 2.2.1 to 2.2.6.

In PLD, as schematically shown in Figure 2.1, a laser is focused onto a target that consists of the elements to be deposited. Due to the sufficiently high energy density of the laser pulse, a small amount of materials is ablated from the surface of the target, creating a plasma. The ablated material that is ejected from the target then travels in a normal direction to the target surface in a highly directed plume. The ablation plume provides the flux of atomic species for film growth. For multi-species inorganics, PLD has proven remarkably effective at yielding epitaxial films. In this case, ablation conditions are adjusted in a way that the ablation plume consists primarily of atomic, diatomic, as well as other low-mass species. This is typically achieved by selecting an ultraviolet (UV) laser wavelength (e.g. KrF excimer 248 nm laser) with small spot size and nanosecond pulse width that can be strongly absorbed by a small volume of the target species. The absorbed laser then exfoliates target species from the surface to create a plasma plume.

PLD is particularly attractive for complex material film growth because of the ease of stoichiometric transfer of target material as well as compatibility with wide range of

background pressure ranging from ultrahigh vacuum (UHV) to tens of Pa. In addition, multiphase films can be deposited with PLD using single mixed stoichiometric target or with multiple targets with pure phases.

A major drawback of PLD is that the thickness distribution from a highly directed and narrow plume is non-uniform. Consequently, the sample size for PLD growth is typically confined to about 5 – 10 mm area. One way to circumvent this drawback is to raster scan the ablation laser over the target while rotating the substrate. This can produce uniform film coverage over large areas. The state-of-the-art commercial PLD has been able to produce uniform deposition up to 8 inches in diameter. Such system, although feasible, is very expensive to be used for commercial applications.<sup>98</sup>

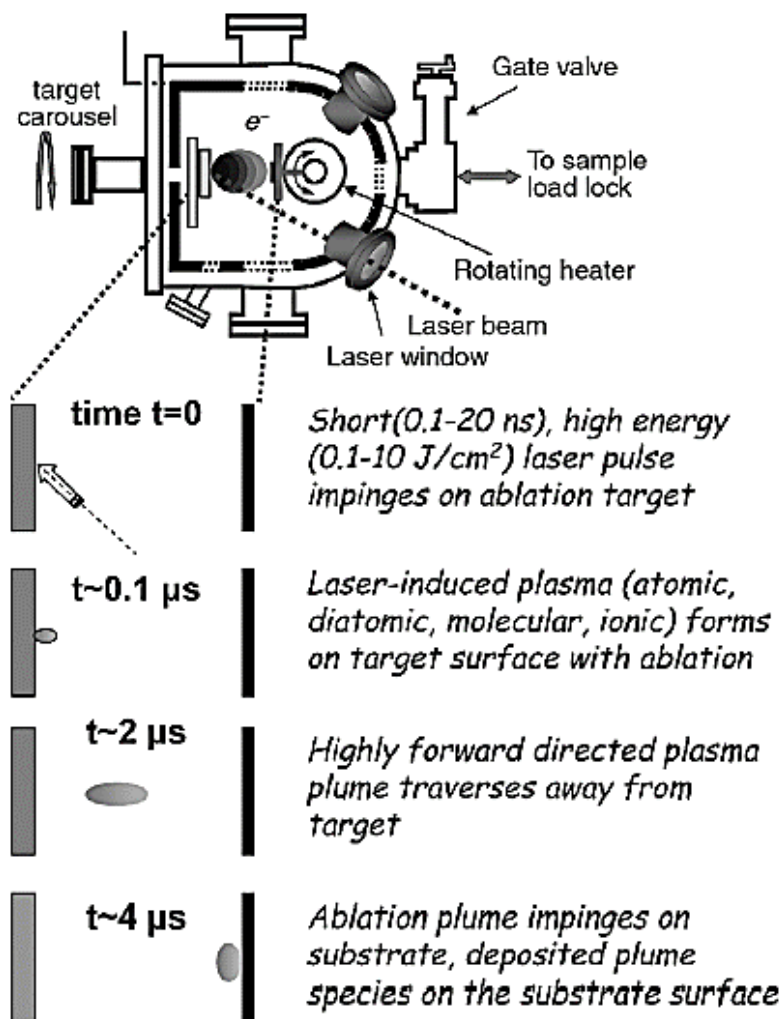


Figure 2.1. Schematic of PLD deposition process.(Figure from <sup>98</sup>)

### **2.2.1. Laser Fluence (Energy Density)**

The ability of PLD to realize stoichiometric transfer of material from multi-species target arises from the non-equilibrium nature of the ablation process itself. When the laser fluence (energy density) is low, the laser pulse would simply heat the target, resulting in the ejection of species due to thermal evaporation instead. In this case, the composition of the ejected species from a multi-species target would depend on the vapor pressures of each species. As the laser fluence is increased, an ablation threshold is reached where laser energy absorption is higher than the energy needed for evaporation. An ideal growth parameter should have a laser fluence above the ablation threshold, which is dependent on the absorption coefficient of the material and is thus laser wavelength dependent. At even higher fluences, absorption by the ablated species occurs, which results in the formation of plasma at the target surface. Thus, with high enough laser fluence (typically from about  $1 \text{ J/cm}^2$ ), vaporization that is not dependent on the vapor pressures of the constituent cations can be achieved and there is almost no selectivity of species ejected from the target surface (e.g. all species are ejected at the same time). Therefore, high laser fluence, together with other optimized parameters that will be discussed subsequently, results in stoichiometric transfer from target to film.

### **2.2.2. Background Gas Pressure**

Apart from laser fluence, a background gas is often required during PLD process. There are two primary purposes of introducing background gas. First, the formation of multi-species thin film often involve a reactive species (e.g., oxygen for oxides) as a component of the plasma. The amount of gas needed for phase formation depends on the thermodynamic stability and oxidation state of the desired phase. Interaction of atomic species with the background gas often produces molecular species in the ablation plume which facilitate phase formation. In addition to stabilizing the stoichiometry of film growth, the background gas serves another purpose to reduce the kinetic energies of the ablated species. Higher pressure generally leads to lower kinetic

energy of ablated species. At low background gas pressure, kinetic energies on the order of several tens of electron volts can be observed. At higher pressure, a background gas can reduce the plume energies to less than 1 eV.

Additionally, increasing background gas pressure generally results in lower deposition rate because ablated species undergoes more collisions and scattering along the way from target to substrate, which may results in less species arriving at the substrate. In relation to target-substrate distance, increasing pressure has similar effect as increasing the target-substrate distance on the deposition rate. Therefore, understanding the interdependency between various deposition parameters is essential to optimize the growth parameter in PLD.

### **2.2.3. Target Materials**

For the deposition of multi-species materials, target selection can have significant impact on film growth process and properties, including particulate density, film epitaxy, phase formation, as well as deposition rate. As a minimum requirement, ablation requires a target material with high optical absorption coefficient at the selected laser wavelength. The most useful range of laser wavelengths for PLD falls between 200 nm and 400 nm. This is due to the fact that most materials used for deposition have strong absorption at that range. As the laser wavelength gets shorter in the range, the scattering coefficients tend to increase, and the penetration depths into the target materials are correspondingly reduced. This is favorable to ablate thin layers from the surface (200 nm penetration depth) of the target materials. KrF (248 nm), XeCl (308 nm) and Nd:YAG (532 nm or 355 nm) laser are among the popular choices in the PLD community.<sup>98</sup> In addition, the target material does not need to have the same phase as that of the desired film. Assuming stoichiometric transfer and negligible evaporation from the film surface, only the target cation stoichiometry need be similar to that of the films. For ceramic targets, one prefers target materials that are dense so as to reduce particulates formation during the ablation process. Apart from polycrystalline ceramic targets, the use of single crystals as ablation targets has been investigated and shown to be effective

in further reduction of particulate densities.<sup>98</sup> However, it is worth mentioning that the use of single crystal as target material is not without problem. For instance, single crystal  $\text{Al}_2\text{O}_3$  was reported to have insufficient optical absorption for the ablation process. For deposition of soft materials, including biological materials, the target might be the material of interest or the material embedded in a matrix of an optically absorbing substance that does not deposit but yields an efficient ablation process.

#### **2.2.4. Target – Substrate Distance**

As mentioned earlier, for the PLD ablation process, the plasma plume has a spatial distribution and the atomic species are non-uniformly distributed within the ablation plume due to its highly forward-directed nature. The implication of the non-uniformity within the plasma plume is that the energy and stoichiometry of the arriving species varies with the variation of target to substrate distance. Generally, a large target-substrate distance results in film with uniform thickness and less strain. Besides, in complex oxide deposition, multiple atomic species are involved. As different atomic size and masses are scattered differently, the film composition can also be affected by altering target-substrate distance.<sup>99</sup> In addition, if the distance is too far away, some species in the plasma plume may undergo more scattering and thus reduces the deposition rate which also affects film thickness and quality.<sup>100</sup>

As discussed in section 2.2.2, although increasing background gas pressure has similar effect as increasing target-substrate distance, the two parameters are not identical and has to be independently adjusted. For instance, to maintain good thickness uniformity in the film, it is generally more effective to increase target-substrate distance rather than increasing background gas pressure. Therefore, careful control of each parameter is required to reach an optimal distance that results in uniform film thickness while maintaining good stoichiometry and phase.

#### **2.2.5. Laser Repetition Rate and Deposition Rate**

High deposition rate is another feature of PLD as compared to MBE or RF

sputtering. By adjusting the laser repetition rate, very high deposition rate on substrate can be achieved. This value is generally higher than those of other physical vapor deposition (PVD) techniques such as RF sputter deposition and molecular beam epitaxy (MBE), which have typical deposition rates of 0.1 to 1 Å/s. Besides controlling the deposition rate, the laser repetition rate has implications for the nucleation and growth processes. During the time interval between laser pulses, which is determined by the pulse repetition rate, the ad-atoms rearrange on the surface by migration and subsequent incorporation through nucleation and growth. This rearrangement can be considered as an anneal process. Because of the instantaneous deposition during laser pulse duration, two basic processes, that is, random deposition (nucleation) and growth through ad-atom re-arrangements are separated in time, which is again unique for PLD.<sup>101</sup>

Lastly, in some cases, laser repetition rate has direct implication on the physical properties of the film. For instance, S.B. Lee et al observed that increasing laser repetition rate generally results in higher electrical resistance of the resulting films. This can be associated with the lack of diffusion time in between two deposition pulses, which results in poorer crystallinity of the film and thus higher resistivity.<sup>102</sup>

### **2.2.6. Substrate Temperature**

Besides all the parameters mentioned earlier, for epitaxial film deposition, the substrate is heated to a temperature ranging from 500 to 1000 °C, depending on materials. Higher substrate temperature generally leads to more effective ad-atom diffusion on the substrate surface, which results in better crystallinity and epitaxial quality. However, this does not apply for all cases. For instance, at high temperatures, the oxidation state of some materials will change from one state to another. This may result in undesirable phase formation on the film. In addition, non-stoichiometry may result for oxides that has volatile species, such as the case for BiFeO<sub>3</sub>. Due to the volatile nature of Bi, the optimal deposition temperature of BiFeO<sub>3</sub> is optimally deposited at 670°C compared to most other oxide materials which are normally deposited at substrate temperature of at least 700°C.<sup>103</sup>

In order to obtain optimized growth parameters for a particular material, systematic and careful tuning of deposition parameters has to be done. In addition, all these parameters are not mutually exclusive. For instance, the overall deposition rate is directly related to target-substrate distance, laser fluence and laser repetition rate while it can be indirectly affected by background gas pressure as well as the density of the target material.

## 2.3 Sputter Deposition

In this work, RF (radio frequency) magnetron sputter deposition is also used for the growth of epitaxial VAN films. A good understanding of sputtering process, especially in relation and in contrast to PLD process is thus critical for the success of depositing VAN films using sputtering. Sputtering is a process by which an energetic particle strikes a surface with sufficient energy that one or more of the surface atoms is ejected from the surface. The incident particle could be an ion, an atom, or an alpha particle, although for most practical purposes ions (typically inert gas ions such as  $\text{Ar}^+$ ) are used. The sputter yield is defined as the ratio of the number of emitted atoms to the number of incident particles. Similar to PLD, sputtering is the ejection of (mostly neutral) atoms from a target material surface. However, unlike PLD, the ejection of atoms from target happens as a result of energetic particle bombardment, normally  $\text{Ar}^+$ . The sputtered materials then arrives at the substrate as neutral species. During sputter deposition, a plasma between target material and substrate is maintained through energetic collision of atomic and ionic species as well as electrons. It is noteworthy that the plasma in PLD is very different in nature compared to the one in sputter deposition. The main difference between PLD and sputtering plasma lies in the highly non-uniform, directed nature of plasma in PLD whereas plasma in sputtering is generally maintained over a large volume and is relatively more uniform.

Based on the nature of the power supply used, sputtering can be generally classified into DC and RF sputtering. In addition, due to the slow rate of RF sputtering, sometimes magnetic field is introduced to increase the sputter rate by more effective ionization as well as better utilization of the sputter target.

### 2.3.1. DC Sputtering

In DC sputtering, a DC diode of simply an anode and a cathode is placed within a vacuum system. Under suitable pressure and voltage conditions, a discharge can be formed between the two electrodes. The minimum voltage for the discharge is a

function of the pressure and the electrode spacing. For instance, two electrodes of a few cm in size, separated by 50 cm and in a vacuum of 100 mTorr might require 600 V to form a plasma. In sputter deposition, plasma is sustained by free charged particles (e.g. Ar<sup>+</sup> and electrons). The ion density and electron density in the bulk plasma are roughly equal. Hence, the net charge in plasma is zero and the plasma is often called quasi-neutral.<sup>104</sup>

As shown in Equation 2.1, the applied sputter power is the function of voltage across the cathode and anode as well as the current from cathode to anode. For a given power, the electric field between cathode and anode is expressed in Equation 2.2. Under an external electrical field  $E$ , a charged particle is accelerated and gains energy. Equation 2.3 shows that at any given time, the particle velocity is inversely proportional to its mass ( $v \propto 1/m$ ).

$$P = V I \quad (2.1)$$

$$V = Ed \quad (2.2)$$

$$m \frac{dv}{dt} = qE \rightarrow v(t) = \frac{qEt}{m} \quad (2.3)$$

where P: power, V: voltage, I: current, E: electric field, d: cathode-anode distance, v: particle velocity, m: particle mass, t: time and q: particle charge.

As a consequence of the inverse relationship between particle mass and velocity, the kinetic energy of lighter particle is higher than that of heavier particle, as shown in Equation 2.4.

$$E_K \propto mv^2 \rightarrow E_K \propto m \left(\frac{1}{m}\right)^2 \propto \frac{1}{m} \quad (2.4)$$

Where  $E_K$  : kinetic energy

The above equations are simplified by ignoring collisions encountered by particles to illustrate that particle velocity is inversely proportional to its mass. In real plasma, the particle reaches an equilibrium velocity at steady state due to collisions with other particles.

Because the electron's mass is much smaller than an atom (hence possess higher

kinetic energy), most of the electrical power from the power supply is transferred to the electron kinetic energy. As shown in Figure 2.2, ions from the plasma are accelerated to the negative electrode (the cathode), and electrons are collected at the anode. The discharge is sustained by secondary electrons that are emitted from the cathode during ion bombardment. These secondary electrons are accelerated into the plasma, gaining enough energy to ionize a few atoms into ions along the way, before they are collected at the anode.

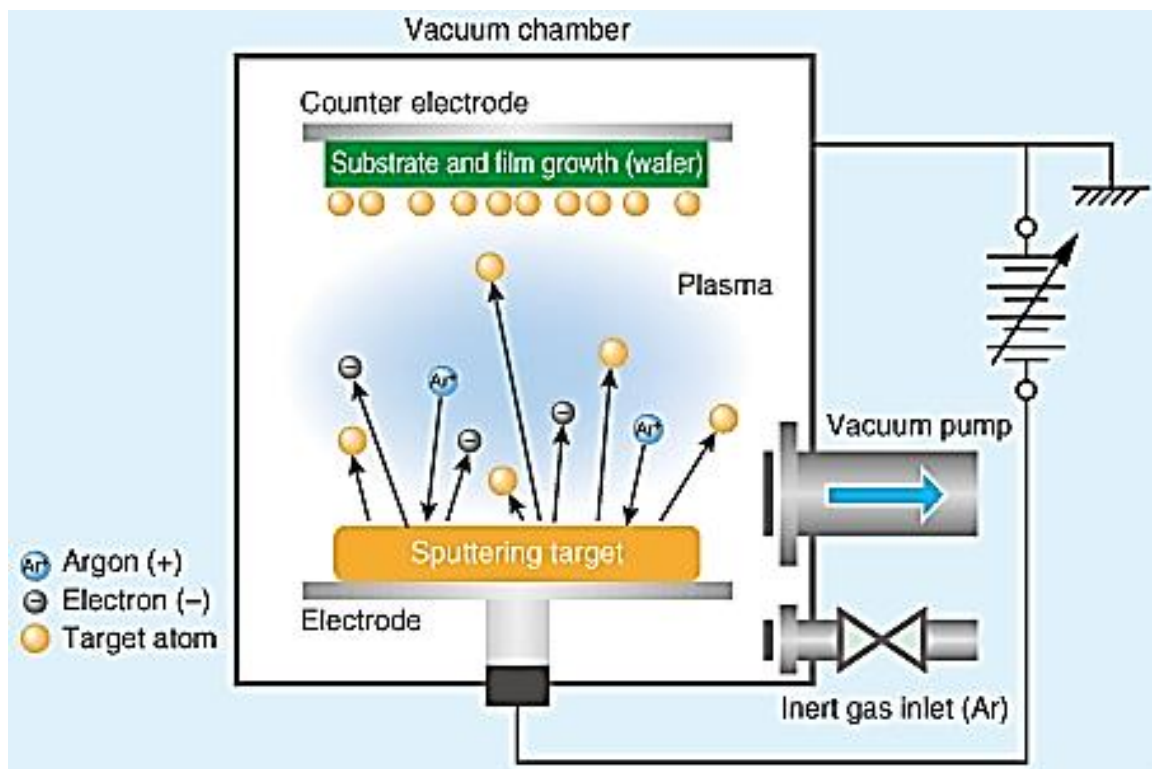


Figure 2.2. Schematic showing sputter deposition process. (Figure from [http://www.m-system.co.jp/newsletter/182/clip\\_contents.html](http://www.m-system.co.jp/newsletter/182/clip_contents.html))

The cross sectional area for electron impact ionization of the gas in the chamber is fairly small and energy dependent.<sup>105</sup> Therefore in a DC sputtering it is usually necessary to operate at fairly high pressures (0.2 to 2 Torr) to have any reasonable ion current. The high pressure results in poor transport of the sputtered atoms away from the cathode due to many collisions along its path and subsequently a very low deposition rate. A second problem arises when the cathode is insulating, such as the case of oxide deposition. Since there is little current flow from the insulating cathode, the sputter etching and deposition process effectively stops. This would occur either if

the cathode were constructed from an insulator, or if a metallic cathode was operated in the presence of sufficient oxygen, and thus over time have a thin oxide layer formed on its surface. Therefore, to avoid the problem of insulating sputter target, RF (radio frequency) sputtering is used.

### **2.3.2. RF Sputtering**

A simple variation of the DC sputtering results in a solution to the two fundamental problems (high deposition pressure and insulating target) mentioned earlier. Instead of applying a DC voltage to the cathode, an AC voltage is applied. In this setup, the ion current density can be increased and concerns with the charging of insulating cathodes are eliminated. The most common AC frequency used is in radio frequency of 13.56 MHz, which is why this technology is often known as RF sputtering. In addition, other frequencies from 60 Hz up to 100 MHz have also been used. The applied RF voltage to the cathode, typically on the order of several kV, results in a plasma that essentially oscillates at the same frequency. Due to their relatively light weight, electrons in the plasma have better response to the alternating electric field compared to heavier ions. Thus, electrons tend to gain additional energy from the oscillation, in a way that has been compared to "surfing" on the applied electric "waves".<sup>106</sup> In this way, energy is coupled into the electron population, which results in more ionization by the high energy tail of the electron distribution (roughly a Maxwell-Boltzmann distribution). The higher ionization means a higher ion current at the same applied power compared to the one in DC sputtering.

Another key advantage of RF sputtering is that the cathode receives no net current from the plasma. Due to the slow response to the alternating electric field, the incident ions from one part of the RF cycle are compensated for by the incident electrons from the other part of the cycle. In this sense, the cathode and anode switch polarity in each RF cycle, resulting in no net current or charging of the cathode (hence there is less heating at the cathode compared to in DC sputtering). In addition, because electrons in a plasma move much more rapidly than ions, the electron bombardment rate of the

cathode during the positive part of the RF cycle can greatly exceed the ion flux during the negative half-cycle. If the cathode is capacitively coupled to the power supply, the net negative charge will start to look like a net negative potential on the cathode.

Effectively, the DC bias of the cathode begins to drift to the negative voltage with each succeeding RF cycle. As this occurs, the fraction of time that the cathode is positive with respect to the anode decreases and the net number of collected electrons decreases, as illustrated in Figure 2.3. Eventually this process reaches equilibrium after just a few cycles with a net DC bias, which is just slightly less than half the applied peak-to-peak RF voltage. This net DC bias is also called self-bias.

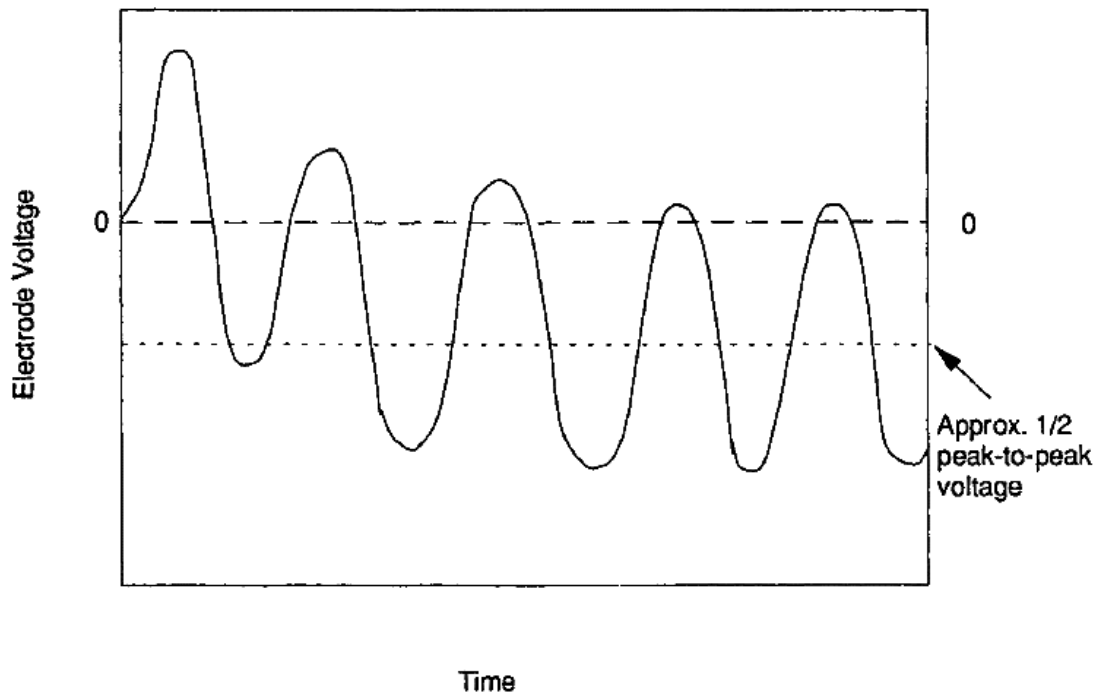


Figure 2.3. Self-bias (net DC bias) voltage build up during RF sputter deposition.(Figure from <sup>107</sup>)

Since the ions effectively do not respond to the 13.56 MHz alternating voltages (due to their heavy mass, they cannot respond to frequencies above a few hundred kHz), they respond to the average DC bias of the cathode. In RF sputtering, the ion energy is generally described by the DC bias because the potential of the plasma is usually close

to zero. In short, the negative DC bias built up on the cathode effectively attracts positive ions (e.g.  $\text{Ar}^+$ ) to bombard the sputter target, resulting in sputtered atoms.

RF sputtering is most commonly used for the sputtering of insulating materials such as oxides (silicon dioxide, titanium dioxide, aluminum oxide, etc.) and also for the sputtering of polymers, such as polyimide. Since sputtered material is mostly emitted in the form of atoms, rather than compounds or molecules, it is often necessary to add additional reactive gas such as oxygen or nitrogen during the sputter deposition of oxides or nitrides, respectively. This can be categorized as reactive sputtering, which is described in more detail later.

### 2.3.3. Magnetron sputtering

A magnetron is a cathode that can be operated either in a DC or AC mode, although the vast majority are operated in DC. A schematic showing side view and top view of sputter target cathode of magnetron sputtering is shown in Figure 2.4. The magnetron uses the basic effect that electrons respond to magnetic fields by the simple relation:

$$F = qV \times B \quad (2.1),$$

where  $q$  is the electron charge,  $v$  its velocity, and  $B$  the magnetic field.

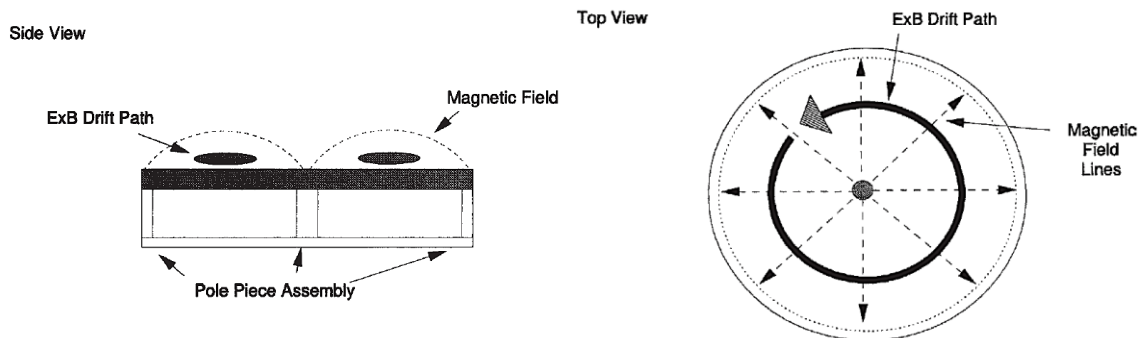


Figure 2.4. Schematic of magnetron sputtering.(Figure from <sup>108</sup>)

In the plasma, electrons moving in magnetic field are subject to Lorentz forces. The direction of force acts at the right angles to the electron velocity, which results in a spiral path for electrons from cathode to anode instead of a straight line when magnetic

field is absent. Since the spiral path that electron takes is significantly longer compared to straight path from cathode to anode, every electron thus has a significantly higher probability to collide with a background gas atoms and ionize them. This results in higher plasma densities at constant applied power (e.g. more efficient ionization process). In addition to the presence of magnetic field, in magnetron sputtering, the drift path for the electrons is configured by careful tuning of magnetic field direction such that it closes on itself, often in the form of a loop (Figure 2.4). The closed path allows electrons to travel around the drift path several times.<sup>109</sup> This results in a high degree of efficiency of coupling the electron energy to the plasma which in turn results in very low discharge voltages, high currents (amperes), and most importantly, a significantly higher sputter rates.

In this work, we will focus on RF Magnetron sputtering which has the ability to grow non-conductive materials yet at the same time has higher deposition rate than RF sputtering. Exploratory work using sputter deposition to grow VAN structure will be presented in details in Chapter 6.

#### **2.3.4. Reactive Sputtering**

Reactive sputtering is a process in which the atoms sputtered from cathode combine with background gas molecules at the sample surface to form a compound. Common examples are the sputtering of Al metal with oxygen gas as background sputter gas to form aluminum oxide, or the sputtering of Ti in the presence of nitrogen to form titanium nitride. In general, the formation of a compound film occurs at the sample surface, not in the gas phase or plasma. However, this leads to a problem in that the metallic cathode is experiencing roughly the same environment as the depositing film. Therefore, the presence of reactive gas can potentially result in reaction on cathode surface as well.

This process can be examined phenomenologically by considering a metal cathode sputtering with initial pure inert gas species, such as Ar. The films that are deposited are purely metallic and generally the deposition rate can be rather high. However, if a small amount of oxygen is then added to the chamber, it is immediately incorporated into the depositing film. It is actually very difficult to observe the effects of introducing small amounts of oxygen because the deposition rate is unchanged, the discharge voltage on the cathode does not change, and the pressure does not change. No oxygen is visible on a mass spectrometer as well. The first reaction from user is to check to make sure the flow controller is working, because it appears as if nothing is happening. The films, which are very reactive, are effectively absorbing all the reactive gas present. If the reactive gas flow is increased, up to a critical gas flow rate, virtually all the reactive gas is still incorporated into the depositing films, the films are at this point becoming saturated with the reactive species and are approaching their terminal (and usually desired) composition.

Above the critical gas flow rate, however, the films become completely saturated with the reacted gas and any additional reactive gas introduced into the chamber will react with the magnetron cathode, changing the cathode surface from metallic to compound, which generally has a much lower sputter yield. This results in a rapid reduction of the sputter rate, and as a result a rapid reduction in the ability of the deposited films to further absorb the reactive species. The system thus goes through an irreversible transition at this critical flow: The deposition rate drops sharply, the discharge voltage changes due to the different nature of compound surface of the cathode, and the reactive species is now no longer totally absorbed by the deposited films because the supply rate of sputtered atoms has dropped significantly.<sup>107</sup> In short, reactive sputtering requires very delicate control of deposition parameters (especially reactive gas flow rate) to achieve the right stoichiometric composition while preventing the reaction at the cathode surface.

### 2.3.5. Deposition Parameters of RF Magnetron Sputtering

Similar to PLD, there are some important sputter deposition parameters that have direct effect on film structure and property. This section introduces the overview of common parameters in sputter deposition of oxide materials such as total gas pressure, substrate temperature, sputter power, Ar/O<sub>2</sub> ratio as well as target-substrate distance. A more detailed discussion of the influence of deposition parameter on film structure will be presented in chapter 6 in relation to the attempt to grow VAN structure using sputtering.

One of the earliest model that links thin film deposition parameters to the microstructures of the films was from the work by John. A. Thornton in 1987.<sup>110</sup> In the work, Thornton famously classified the resulting film structure into 4 zones in a range of deposition temperature and pressure. So called Thornton's zone model provides useful guidance for thin film deposition. Although the original work was done using sputtering, this model is not only relevant to sputtering, it also applies to other physical depositions such as PLD. Figure 2.5 shows the schematic diagram of Thornton's zone model.

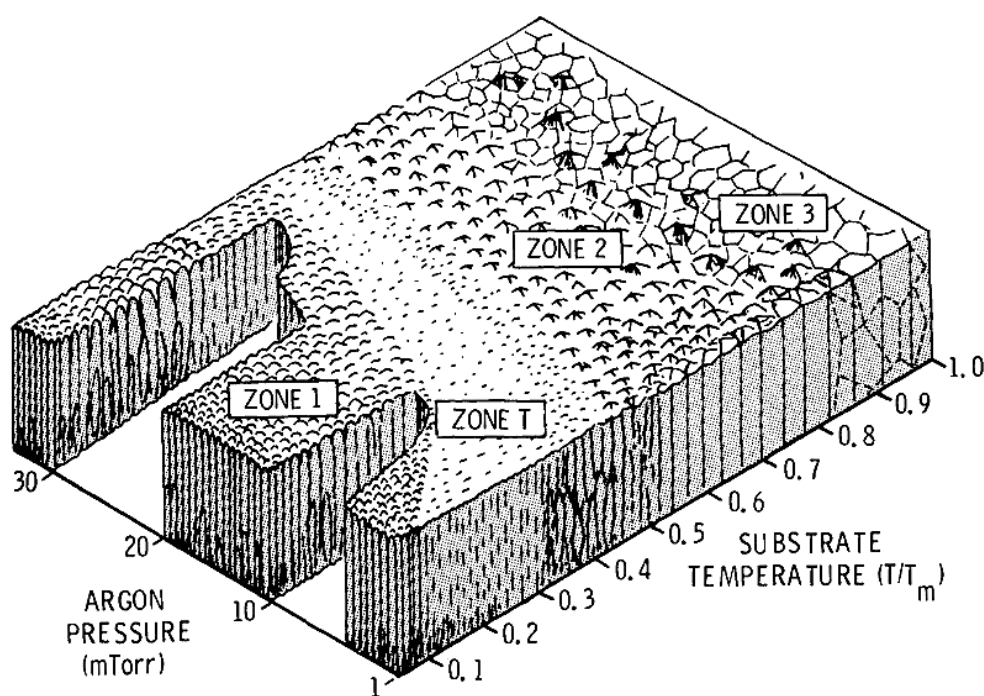


Figure 2.5. Schematic of magnetron sputtering. (Figure from <sup>110</sup>)

As shown in Figure 2.5, film microstructure can be classified into 4 different zones namely zone 1, zone T, zone 2 and zone 3. Two deposition parameters, argon pressure (mTorr) and substrate temperature with respect to melting point of the material ( $T/T_m$ ) are plotted on each of the horizontal axis, respectively.

In order to discuss the effect of substrate temperature and pressure on film structure, it is useful to describe film growth in three steps. The first step involves the transport of sputtered species to the substrate. The second step involves the adsorption and surface diffusion of sputtered species on the substrate. The final step involves the movement of atoms to their final positions within the lattice by bulk diffusion and solid state reactions. In zone 1 ( $T/T_m < 0.3$ ), at low substrate temperature, the surface diffusion of arriving atomic species is minimal. This results in porous structure with tapered crystallites separated by voids. At slightly higher temperature, zone T can be associated with densely packed fibrous grains with less porosity than zone 1. Increasing temperature gives the atomic species higher energy to overcome surface diffusion activation energy, hence more densely packed structures is formed. Besides increasing temperature, one can get a relatively more dense structure in zone T by decreasing the argon pressure. At lower argon pressure, the sputtered atomic species undergoes less collision along the path from cathode to anode, resulting in higher arrival velocity on the substrate which gives it enough energy for surface diffusion.

At even higher temperature from the zone T range, zone 2 is defined by oriented columnar grains with grain boundaries. Surface diffusion becomes dominant in this zone, as evidenced by increasing grain width with increasing temperature. Likewise, besides increasing temperature, lowering argon pressure results in similar effect of increasing grain width. However, it is worth noting that in zone 2, lowering argon pressure is less effective compared to the case of zone 1 and zone T.

Finally, further increasing substrate temperature from zone 2 results in zone 3 ( $T/T_m > 0.8$ ). Zone 3 is characterized by recrystallization and grain growth, which

results in large grain structure. The ease of bulk diffusion due to high temperature enables grains to recrystallize and hence improves crystallinity. With respect to attempt to grow VAN film in this work, zone 3 is the most desirable as it promotes good epitaxial quality with less defects compared to other zones. Besides, high surface temperature allows atomic bulk diffusion for atomic species, which is the prerequisite for VAN film growth.

Besides substrate temperature and argon gas pressure, finding a good ratio of Ar/O<sub>2</sub> mixture during the sputtering process is also important. On one hand, for deposition to be effective, there has to be enough Ar to bombard the cathode target. On the other hand, the presence of O<sub>2</sub> gas is important to maintain oxygen stoichiometry in oxide deposition. Lastly, film structural quality also depends on deposition rate, which can be controlled by target-substrate distance as well as sputter power. Higher sputter power or nearer target-substrate distance generally results in higher deposition rate.

# Chapter 3 Experimental and Characterization Techniques

This chapter presents an introduction and basic working principles of all experimental and characterization techniques used in this work. The details of experimental parameters of any particular technique will be discussed together in the result chapters (e.g. chapter 4, 5 and 6) when the technique is used.

## 3.1 XRD

XRD (X-ray diffraction) is a powerful and non-destructive method in crystalline/semi-crystalline material analysis. It is widely used in phase identification, crystal structure and orientation, epitaxy determination, as well as strain analysis. X-ray are electromagnetic radiations with wavelength in the range between 0.05 – 0.25 nm.<sup>111</sup> In this work, *Panalytical X'Pert Pro* high resolution XRD with PreFIX module and Cu K $\alpha$  source, with the wavelength 0.154 nm was used to characterize our films. This section describes the working principle and information obtained from various scan modes used in this work.

In a crystalline lattice, atoms are periodically arranged in a long-range order. The wavelengths of X-rays is chosen to be of similar magnitude as the interatomic distances. In this case, the atoms are analogous to the diffraction gratings for X-rays. When the incident X-ray beam is coherently scattered by the atoms, there is bound to be constructive interference at some specific angle which corresponds to the diffraction peaks observed in an XRD pattern. In general, the XRD pattern is a plot of diffraction intensity over a range of diffraction angles. The scan angle depends on the scanning modes. It can be  $2\theta$  in a  $2\theta$ - $\omega$  scan, or  $\omega$  in  $\omega$  scan. The peak intensity is related to the structure of the material, the orientation, crystallinity, and other instrumental parameters.

Figure 3.1 shows the schematic diagram of X-ray diffraction process. Atoms in the

crystal are aligned in such a way that they are oriented on the parallel planes labeled as A, B, C with the inter-planar spacing of  $d$ , and the incident X-ray wavelength  $\lambda$ . The incident angle is defined as  $\theta$ , which is called the Bragg angle. Incident beam 1 is diffracted by the atom to beam 1', and same occurs for other parallel beams.

In order for diffraction to occur, an essential condition must be fulfilled. For instance, in order for the diffracted beam 1' and 2' to have constructive interference, the differences in the X-ray paths must be  $n\lambda$ , where  $n$  is an integral. In this case, the difference in the X-ray path length can be simply expressed as  $2d\sin\theta$ . Therefore, this essential condition can be written as:

$$2d\sin\theta = n\lambda \quad (3.1).$$

This equation is also called Bragg's equation.

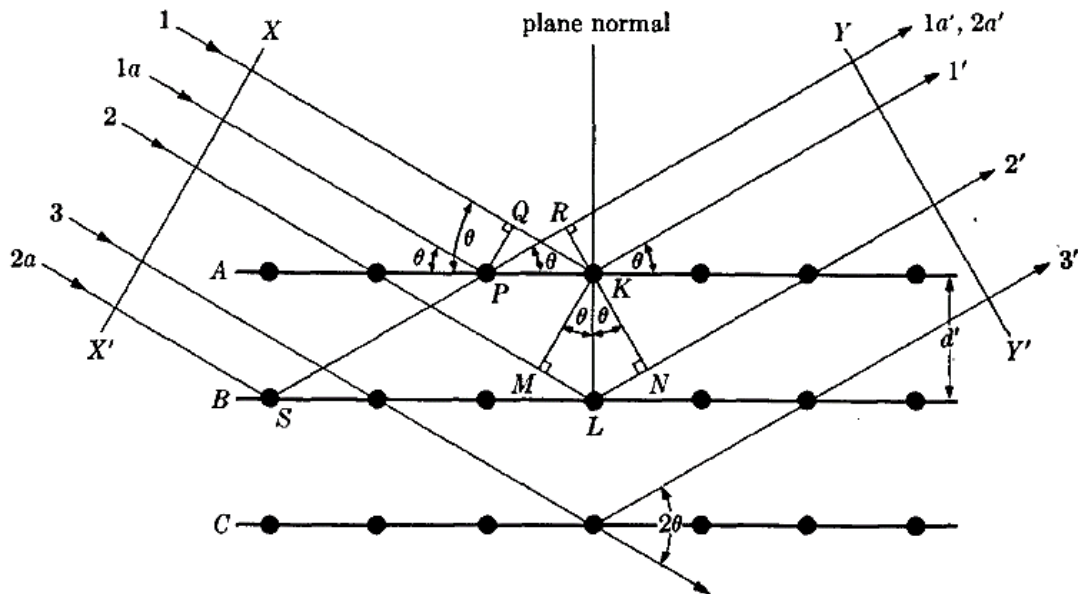


Figure 3.1 Diffraction of X-rays by a crystal. (Figure from <sup>111</sup>)

The commonly used XRD modes in this diffractometer such as  $2\theta$ -  $\omega$  scans,  $\omega$  scans (rocking curves), Phi-scans, and reciprocal space map (RSM) will be discussed below.

### 3.1.1. $2\theta - \omega$ Scans

$2\theta - \omega$  is a symmetric scan, which means that the incoming X-ray and the diffracted X-ray are of the same angle with respect to sample normal direction. From the plot of diffraction intensity vs.  $2\theta$ , the  $d$ -spacing can be extracted from the peak position using the Bragg equation. It contains information on the lattice parameter (*out-of-plane*), which can be influenced by compositional change or strain. Although  $2\theta - \omega$  scan is normally used for phase identification, it can also be used to estimate the lattice mismatch induced strain between film and substrate, the film orientation, and even film thickness using X-ray reflectivity (XRR) mode at low diffraction angle (e.g.  $2\theta < 5^\circ$ ). In this work, this scanning mode is primarily used for phase identification. A phase is defined as a specific set of chemical and atomic arrangement with a unique spacing, thus each phase has a unique diffracted pattern. The relative intensity of diffracted peaks and their positions can be used to match with the reference patterns so that the phase can be determined. Miller indices ( $hkl$ ) can be used to identify different planes and orientations.

The working principle of  $2\theta - \omega$  scan is illustrated in Figure 3.2, where  $\omega$  is the incident angle,  $2\theta$  is the angle between detector and the X-ray,  $S$  is the diffraction vector which bisects the incident beam and the diffracted beam. In this mode,  $\omega$  is set to follow the value of  $2\theta$ , with a small offset which is used to align the diffraction vector to be parallel with the sample plane normal.

If properly aligned, an epitaxial film or single crystal only have one family of diffraction peaks. For a polycrystalline sample, there are a large number of crystallites with random orientations. Therefore, all possible diffraction peaks from the sample can be observed, albeit with lower intensity compared to aligned sample.

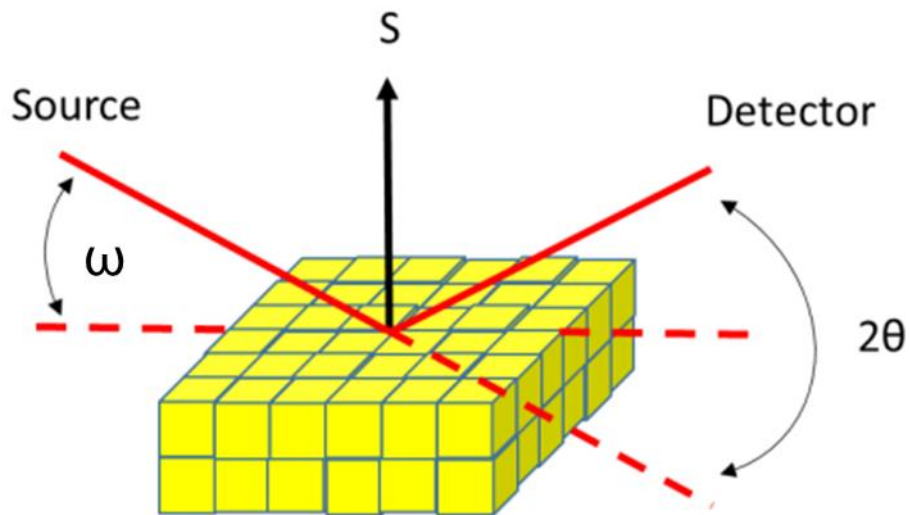


Figure 3.2 Schematic drawing of  $2\theta$ - $\omega$  scan.

### 3.1.2. $\omega$ Scan (Rocking Curve)

Rocking curve or  $\omega$  scan is a plot of intensity vs.  $\omega$ , which is also called rocking curve. In this mode, the detector is fixed at a specific angle  $2\theta$  while the incoming X-ray beam angle  $\omega$  is scanned through a range of angles, usually over a few degrees, as schematically illustrated in Figure 3.3.

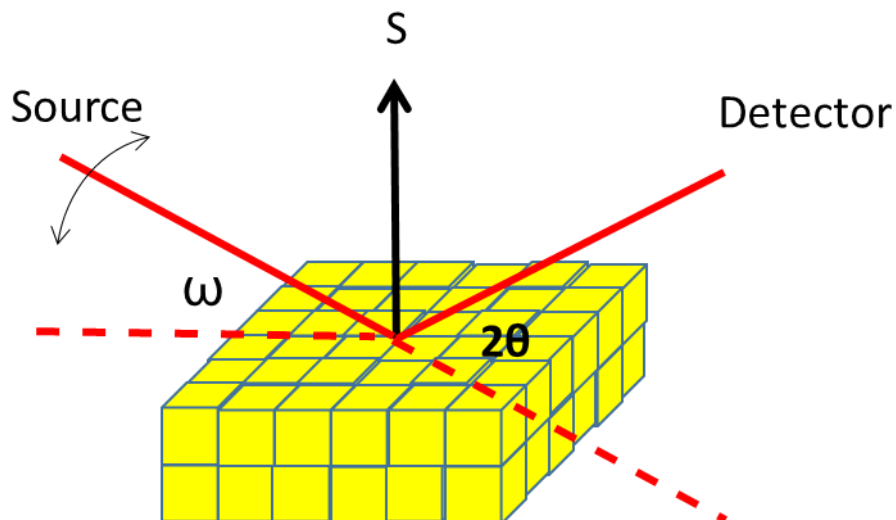


Figure 3.3 Schematic drawing of  $\omega$  scan.

Ideally, a well-aligned high quality crystal will have a very sharp rocking curve with a small full width half maximum (FWHM), notwithstanding broadening from the instrument. In thin films, there are bound to be defects like dislocation, misorientation and inhomogeneity. These defects cause disruptions in the originally parallel atomic planes, and thus resulting in the broadening of the rocking curve.

### 3.1.3. Phi Scans

For thin film analysis, phi ( $\Phi$ ) scan is usually used to measure the *in-plane* orientation of the thin film with respect to the substrate. As shown in Figure 3.4, this is done by scanning the  $\Phi$  angles over  $360^\circ$  range while measuring the intensity of a specific planar orientation, with other parameters such as  $\omega$ ,  $2\theta$ , and  $\chi$  (chi) being constant. The resulting Phi scan can be analyzed to determine the *in-plane* orientation of the film with respect to the substrate. In addition, the crystal symmetry in the *in-plane* direction can also be determined from Phi-scan. For instance, a cubic unit cell will have four equally-spaced peaks reflected in the phi scans when it is scanned over  $360^\circ$ .

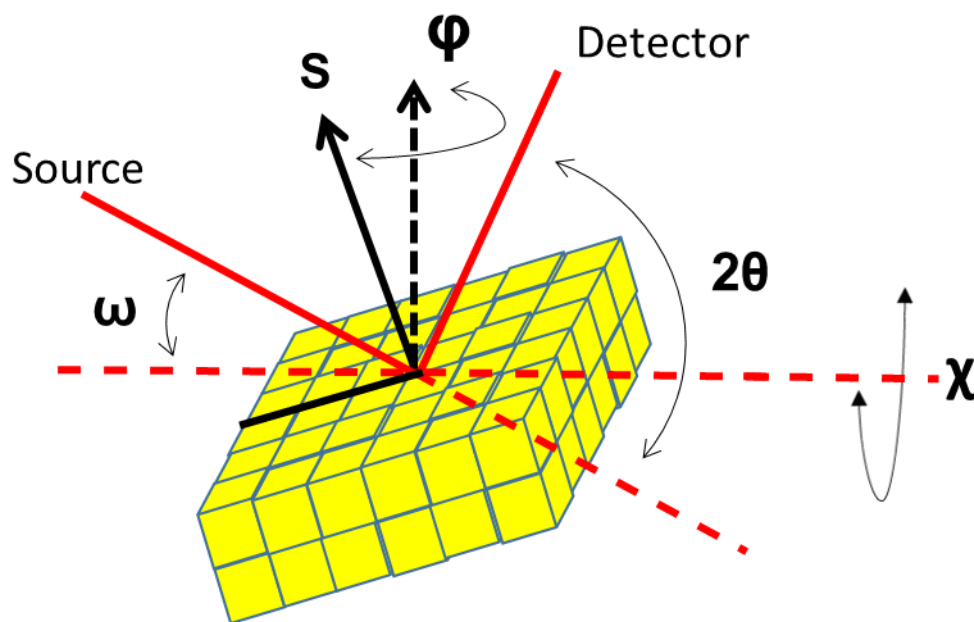


Figure 3.4 Schematic drawing of  $\Phi$  scan with  $\omega$ ,  $2\theta$ , and  $\chi$  (chi) being constant.

### 3.1.4. Reciprocal Space Map (RSM)

A reciprocal space map is basically a two-axis asymmetric scan. It is schematically shown in Figure 3.5. In a sense, it is a 2-dimensional scan. It consists of many sets of  $2\theta$ - $\omega$  scans with a fixed value of  $\omega$  over a range of  $\omega$ . RSM map is frequently used in strain analysis and is usually presented in a contour map, with  $Q_x$  and  $Q_z$  (reciprocal space lattice parameter) being the axis. The diffractometer angles can be converted to reciprocal space using the following equation:

$$Q_x = \frac{\cos \omega - \cos(2\theta - \omega)}{\lambda} \quad (3.2),$$

$$Q_z = \frac{\sin \omega + \sin(2\theta - \omega)}{\lambda} \quad (3.3).$$

Apart from strain analysis, RSM indicates the crystalline quality of the observed phase as well. For example, a relatively pointed and sharp peak indicates high epitaxial quality film and vice versa. Lastly, crystal structure information is also reflected in the reciprocal space map scan. For instance, a monoclinic unit cell will result in double peak (peak twinning) in the resulting map.

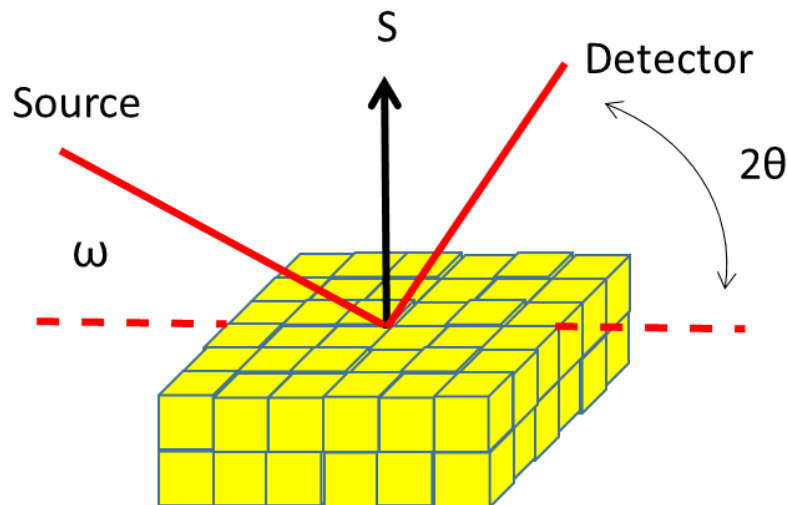


Figure 3.5 Schematic drawing of the RSM configuration.

## 3.2. AFM

The surface topography of thin films can be characterized by AFM on the scale from micrometer down to sub-micrometer range. The basic working principle is illustrated in Figure 3.6. The sample surface is scanned with a cantilever with an atomically sharp tip. The cantilever motion is controlled by a piezoelectric actuator using an active feedback loop that receives its signal from a laser reflected off the top of the cantilever near to the cantilever tip. When the tip is close enough to the sample surface, the cantilever can be deflected due to the interaction between the cantilever tip and the sample. The deflection is then monitored by a diode laser which reflected off the back of the cantilever towards a photodetector. The photodetector is used to monitor as well as amplify the cantilever deflection. A surface topography image can therefore be built up. A feedback circuit loop is used to control the tip-sample distance in order to maintain a constant force and avoid damage the tip or the sample.<sup>112</sup> The AFM measurements in this work were carried out on the AFM: Multimode SPM Nanoscope III. The data analysis was carried out using software WSxM 5.0.<sup>113</sup>

Depending on the situation, forces that are measured in AFM include the mechanical contact force, van der Waals forces, magnetic forces (magnetic force microscope, MFM), chemical bonding, electrostatic forces, *etc.* Some of the most commonly used AFM modes for oxide thin films characterizations are contact mode, tapping mode as well as piezoresponse force microscopy (PFM).

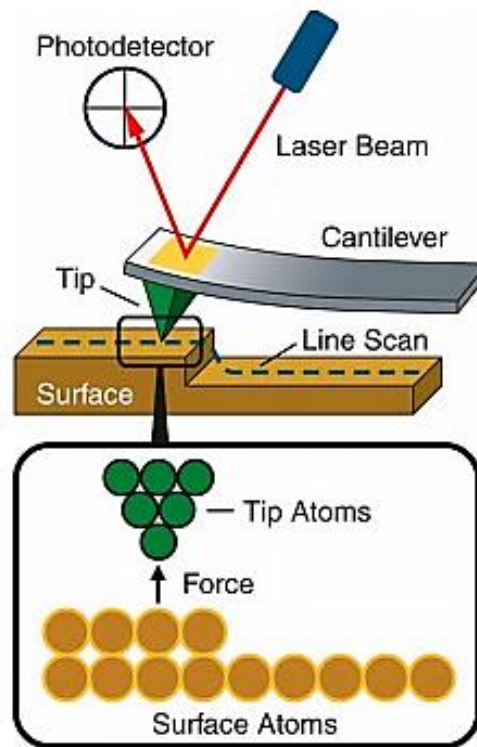


Figure 3.6. A schematic picture of the AFM working principle. (Figure from <http://www.keysight.com/main/editorial.jsp?cc=IT&lc=ita&ckey=1774141&nid=-33986.0&id=1774141>)

### 3.2.1. Contact Mode

As the name suggests, in contact mode the AFM tip scans the sample in contact with the surface during the scanning. The cantilever is "dragged" across the sample surface and the contours of the surface are traced directly using the deflection of the cantilever. One drawback of the tip remaining in contact with the sample is that large lateral forces can be exerted on the sample as the tip is scanned over the sample. These large forces can result in deformed tip and damaged samples. The contact mode works reasonably well for rigid materials with rough surface.

### 3.2.2. Tapping Mode

One of the most commonly used working modes in AFM is the tapping mode. In this mode, the cantilever is driven slightly below its resonance frequency with the tip

near the surface of the sample, making contact with the sample at the bottom of its swing. During scanning, when the tip is still far from the sample surface, the cantilever oscillates at a constant amplitude. When the tip is brought closer to the sample surface, the Coulombic and van der Waals interactions impede the movement of the cantilever. As a result, the effective resonance frequency and the oscillation amplitude of the cantilever is dampened when the tip draws nearer to the sample surface. The amplitude would first gradually reduce, followed by an abrupt drop when the tip-sample distance is close enough that the tip completely stuck to the sample surface. During normal operation, the gradual change in the oscillation amplitude is used to reflect the tip-sample distance. A feedback circuit is used to keep the oscillation amplitude constant so that neither the tip nor the sample would be damaged.<sup>112</sup>

### **3.2.3. Piezoresponse Force Microscopy (PFM)**

PFM is a commonly used method for measuring the ferroelectric domain switching at nanoscale. An agilent 5500 atomic force microscope equipped with piezoresponse force mode was used to obtain piezoelectric response domain imaging and quantitative piezo response phase as well as amplitudes of the films. In piezo response domain imaging,  $\pm 10$  V external voltage were applied through the conductive tip at an excitation frequency of 10 kHz over the scanning area. The phase and amplitude of the local piezo response were detected while mapping out the local piezo domain configurations. In this work, multiple domain switching with different scan areas were performed using Olympus AC240TM Platinum coating Silicon probe. The force constant of the cantilever is 2 N/m and the resonant frequency is 70 kHz. The tip size is approximately  $28 \text{ nm} \pm 10 \text{ nm}$ .

## **3.3. Superconducting Quantum Interference Device (SQUID)**

SQUID has been widely used to measure magnetic properties of material. The SQUID working principle is based on Josephson effect on two parallel Josephson

junctions consisting of two identical superconductors separated by a thin insulating layer. The device allows a change of magnetic flux which induced additional voltage in the junction to be measured. The flux which associated by Josephson junctions is quantized in units of flux quantum  $\phi_0 = 2.07 \times 10^{-15} \text{ T.m}^2$ , which is the smallest change of flux that can be detected. Figure 3.7 illustrates the working principle of SQUID.

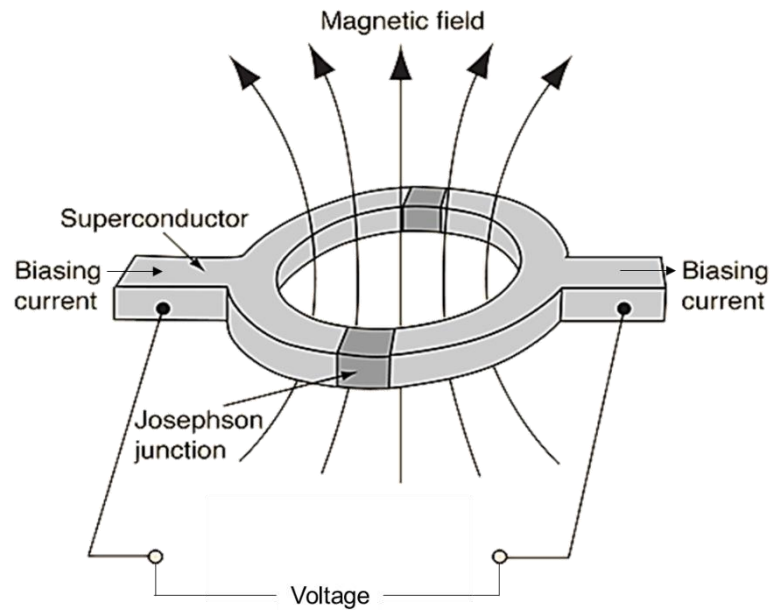


Figure 3.7. A schematic of the SQUID setup showing two identical superconductor separated by thin insulating layers of Josephson junction (<http://hydrogen.physik.uni-wuppertal.de/hyperphysics/hyperphysics/hbase/solids/squid.html>)

SQUID is operated with a constant bias current, thus the measured voltage oscillates with the phase changes between the two junctions, which depends upon the change in the magnetic flux. Detecting this circulating current enables the use of the SQUID as a magnetometer. In this work, the temperature dependence of magnetisation (M vs T) was determined using a superconducting quantum interference device (SQUID) magnetometer (Quantum Design, MPMS).

### 3.4. Ferroelectric Properties

The total electric flux density D in a ferroelectric system comprises of both the

linear dielectric component and the nonlinear ferroelectric polarization. When the ferroelectric is subject to an electric field, the change in  $D$  gives a displacement current density

This current is integrated to obtain  $D$ . The measured  $D$  is plotted versus the applied electric field  $E$ . This plot is commonly called the  $P$ - $E$  plot as the contribution from the linear dielectric response is very small compared to the ferroelectric polarization.

The ferroelectric properties of the samples were investigated using a Radiant Technology Precision Premium II tester. Two identical bipolar triangular waveforms were used successively for the measurement (Figure 3.8). The first wave was to preset the ferroelectric to  $-P_r$  (remnant polarization) state. The second wave was used to measure the hysteresis loop.

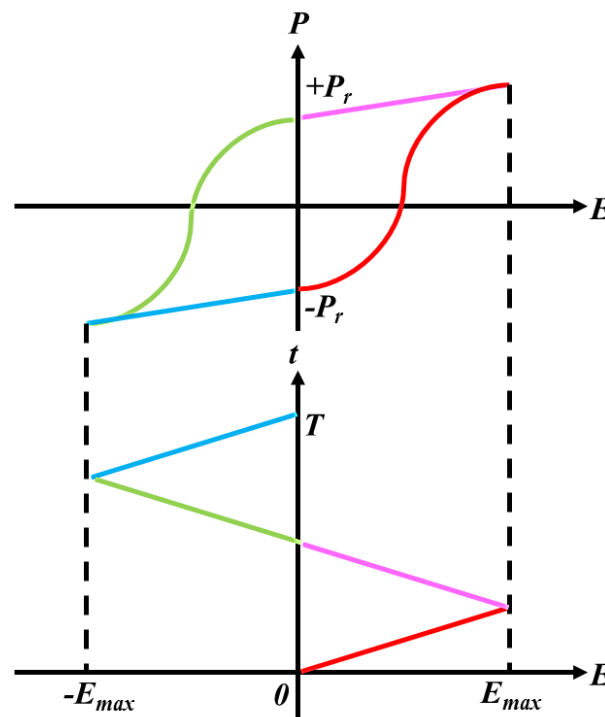


Figure 3.8. (a) Ferroelectric hysteresis (b) The input wave form.  $T$  represents the measurement period. Colored segments represents the correlation between the input wave form and the resulting hysteresis loop segment.  $E$  represents the applied electric field.  $P_r$  represents remnant polarization.

This system was also used for the poling of VAN films. In this case, a uni-polar triangular waveform was used with the maximum voltage larger than the coercive field (the magnitude of electric field required to erase the remnant polarization). The pulse period was about 0.1 ms. The use of the short electrical pulse was to prevent damages to the VAN films that could occur when conventional DC poling was used.

### **3.5. Field Emission Scanning Electron Microscope (FESEM)**

Conventional optical microscopy may not be able to resolve features on the order of nanometers due to the fundamental diffraction limit of visible light wavelength. Electrons can attain sub-nm wavelength when accelerated with a few kV voltage and thus resulting in much higher spatial resolutions. Among the many electron microscopy techniques, SEM is routinely employed for the observation of the micro-structures of semiconductor and MEMS devices. SEM scans across the sample surface with a collimated electron beam, which generates secondary electrons from the sample surface among other products. In the most common case the secondary electrons are collected and processed to form an image of the sample surface. The contrast of the image is mainly caused by the topography of the sample. The advantage of using secondary electrons is its smaller generation volume and thus it provides higher resolution than back scattered electrons. In addition, it is not a strong function of the atomic  $Z$  number and thus will not cause appreciable contrast from the variations of atomic species. It is important to note that although the electron beam diameter on a field emission SEM is on the order of 0.1 nm, their resolution is not as sharp as 0.1 nm, but rather it is in the range of about 1 nm due to the secondary electron (electron generated from sample by the incoming electron beam from the SEM) generation volumes. The generation volume of the secondary electrons in an insulator such as a ferroelectric film is usually a few tens of nanometers in depth and thus can affect the SEM image. As a result, the images of the same surface can look different depending on the particular parameters used. It is important to understand the influence of the different parameters on the SEM image. Although higher acceleration voltage produces electrons with smaller wavelength, the interaction volume is also increased and unwanted signals such as back scattered electrons will be increased. This often results in degraded image. Charging and sample damage might also be resulted. As a result, it is often desirable to use smaller accelerating voltage, especially on insulating or relatively smooth samples.

Other parameters can also be adjusted for optimum image quality. The resolution can be enhanced by using smaller objective aperture and smaller probe current, even though it may result in grainy image due to charging. The working distance can also be reduced to improve resolution, but at a price of shallower depth of field. Tilting the sample can improve contrast by enhancing the secondary electron emission due to larger interaction area between incoming primary electron beam with the sample. It is often necessary to optimize these parameters to obtain good SEM images of insulating ferroelectric thin films. In this project a JSM-6700F FESEM from JOEL Ltd. was used for the characterization of VAN samples. Samples were normally coated with gold prior to the observation to minimize the charging effects.

### **3.6. Transmission Electron Microscopy (TEM) and Scanning Transmission Electron Microscopy (STEM)**

TEM and STEM provide detailed information in analyzing the crystallographic structure of a material, its phase morphologies, as well as misfit dislocation to the atomic level. The TEM and STEM characterizations in this study were performed at Texas A&M University, USA by Dr. Zhang Wenrui and Dr. Li Leigang as well as in Los Alamos National Laboratory by Dr. Jia Quanxi. Both the cross sectional TEM and STEM images were captured using a Tecnai G2 F20 Field Emission TEM that operated at 200 kV. This system allowed a point to point resolution of 0.27 nm. The nanocomposite films were prepared using conventional slicing, grinding, polishing and ion thinning in order to reduce the thickness for electron transparency. At first glance, TEM and STEM appear to be very similar in the imaging functions. But they provide different mode of images and information. TEM produces the conventional bright field, dark field as well as high resolution images. STEM offers clear Z-contrast images which enable elemental mapping contrast due to its ability to be raster scanned across the specimen. Besides the morphological imaging, the selected area electron diffraction (SAED) were collected as well.

# Chapter 4 3-D Strain States in $(\text{Ba}_{0.6}\text{Sr}_{0.4}\text{TiO}_3)_{1-x} - (\text{Sm}_2\text{O}_3)_x$ and Its Influence on Ferroelectricity

## 4.1 Introduction

Vertically aligned nanocomposite thin films are proving to be increasingly important for creating advanced multifunctional oxide thin films with new properties.<sup>28</sup> In these composites, new phenomena also occur giving a very powerful way to tune device functionality. Very high ferroelectric Curie temperatures,<sup>30</sup> strongly improved dielectric tunability,<sup>48</sup> reducing dielectric loss,<sup>52</sup> enhanced multiferroic coupling,<sup>54</sup> photostriction-magnetic coupling,<sup>55</sup> strongly enhanced current densities in superconductors,<sup>67</sup> new kinds of memristor devices,<sup>102</sup> and strongly enhanced ionic conduction at lower temperatures have all been reported.<sup>114-115</sup>

However, the understanding and origin of unusual strain states in nanocomposite films have not been explored to date. On the other hand, strain is critical to tuning the properties of strongly correlated metal oxide films where bond lengths and bond angles strongly influence the wide-ranging functional phenomena. What is known is that compared to planar thin films, the strain in vertical nanocomposites does not relax when the film grows thicker. This is due to the fact that vertical lattice epitaxy between the phases dominates the strain state of the system, making the substrate contribution *insignificant* above a few 10's of nm where the substrate induced strain relaxes.<sup>4</sup> What is not known is how and why strain arise in nanocomposite films. In a previous study in the group, it was shown that auxetic-like 3D strain was observed in nanocomposite microactuator films of  $(\text{BaTiO}_3)_{0.5}-(\text{Sm}_2\text{O}_3)_{0.5}$ . Auxetic material is a phenomenon in which the poisson's ratio is positive instead of negative as in the case for most materials. The implication of auxetic-like properties is that when tensile (compressive) strain is applied to the material in one direction (e.g. *in-plane*), it will result in an expansion

(contraction) in its perpendicular direction (e.g. *out-of-plane*), which is opposite to the elastic behavior of most materials. The transverse piezoelectric coefficient,  $d_{31}$ , in the films was positive instead of negative as observed in the conventional thin film case. Also, at room temperature, its magnitude of  $d_{31}$  was found to be  $> 200 \text{ pm V}^{-1}$  which exceeded the values of PZT films.<sup>116</sup> In a similar system of  $(\text{Ba}_{0.6}\text{Sr}_{0.4}\text{TiO}_3)_{0.25}\text{-(Sm}_2\text{O}_3)_{0.75}$ , it was shown that both tunability and dielectric loss could be simultaneously improved which is in contrast to the case for standard  $\text{Ba}_{0.6}\text{Sr}_{0.4}\text{TiO}_3$ . Again, unusual strain states were thought to be responsible.<sup>48</sup>

In this work, we explored the strain states in the  $(\text{Ba}_{0.6}\text{Sr}_{0.4}\text{TiO}_3)_{1-x}(\text{Sm}_2\text{O}_3)_x$  thin film system. The system is ideal from the chemical point of view because there is minimal intermixing between the two component phases.<sup>102</sup> The films and preliminary XRD and ferroelectric data of this material system was collected by Dr. Oon Jew Lee, a former student in the group, but it was not systematically analyzed. In this work, the XRD and ferroelectric data was verified experimentally from the available samples and analyzed systematically. *Panalytical* X'Pert Pro high resolution XRD with PreFIX module and Cu  $K\alpha$  source, with the wavelength 0.154 nm was used to characterize our films. The XRD work was done using  $2\theta$ - $\omega$  scan as well as reciprocal space mapping (RSM) to study various strain states in the film both in the in-plane and out-of-plane directions. To ensure consistency, the scanning step size was fixed at  $0.02^\circ$  while the scanning time per step was fixed at 1 second for all XRD scans on all samples. TEM and SEM characterization was done by Prof. Haiyan Wang's lab in Texas A&M University in the U.S. In addition, AFM and PFM was done using AFM: Multimode SPM Nanoscope III with scanning resolution of 512 lines per scan and scanning area ranging from 100 nm to 1 $\mu\text{m}$ . The data analysis of AFM and PFM were carried out using WSxM 5.0 software. Lastly, the ferroelectric loop was characterized using agilent 4294A with loop frequency of 10 kHz and maximum applied field of 300 kV/cm. The waveform used for ferroelectric hysteresis measurement was the standard triangular waveform with preset loop and preset delay of 1 ms. Unless otherwise mentioned, all experiments were carried out at room temperature.

A model which incorporates thermal expansion mismatch and lattice mismatch strain between the phases was used to understand how and why the *in-plane* and *out-of-plane* lattice parameters vary with  $x$  in the way they do. Finally, the ferroelectric properties of the films were probed and the enhanced properties observed explained in terms of the strain states observed.

## **4.2 3D Auxetic-like Strain in $(\text{Ba}_{0.6}\text{Sr}_{0.4}\text{TiO}_3)_{1-x}-(\text{Sm}_2\text{O}_3)_x$ VAN**

The BSTO-  $\text{Sm}_2\text{O}_3$  VAN thin films were fabricated from 5 different ceramic targets of  $(\text{BSTO})_{1-x}-(\text{Sm}_2\text{O}_3)_x$  with  $x = 0.00, 0.25, 0.50, 0.75,$  and  $1.00$ . First the  $\text{Ba}_{0.6}\text{Sr}_{0.4}\text{TiO}_3$  powder was synthesized by mixing 99.99% pure  $\text{BaTiO}_3$  and  $\text{SrTiO}_3$  with 99.99%  $\text{Sm}_2\text{O}_3$  powder. The targets were then made by mixing and grinding  $\text{Ba}_{0.6}\text{Sr}_{0.4}\text{TiO}_3$  and  $\text{Sm}_2\text{O}_3$  powders followed by cold pressing into pellet with 1 inch diameter using force equivalent to 5 tons of weight for 30 minutes. The pellet was then sintered at  $1300\text{ }^\circ\text{C}$  for 12 hours. Pulsed laser deposition (PLD) using a KrF excimer laser with 1 Hz repetition rate, a laser fluence of  $\sim 2\text{ J/cm}^2$ , and an oxygen pressure of 20 Pa was used to grow the films. The films were grown onto (001) single crystal  $\text{SrTiO}_3$  (STO) substrates with 30 nm thick buffer layers of  $\text{SrRuO}_3$  (SRO). The SRO layers were first deposited off-axis (in which the laser plume direction is parallel to the substrate surface instead of normal to substrate surface as in the case of most other depositions) at  $700\text{ }^\circ\text{C}$  and then the BSTO-  $\text{Sm}_2\text{O}_3$  deposited at  $800\text{ }^\circ\text{C}$ . After deposition, the samples were cooled to room temperature with a cooling rate of  $10\text{ }^\circ\text{C}/\text{min}$  in 1 mbar oxygen atmosphere to prevent formation of oxygen vacancies. No other special growth measures had to be taken to make the films self-assemble into a structure composed of “vertical nanopillars of one phase in a matrix of the other phase” with a high level of epitaxy. BSTO-  $\text{Sm}_2\text{O}_3$  film thicknesses of 300 nm, 600 nm, and 1000 nm were grown based on the 5 different compositions mentioned earlier.

For  $x = 0.25$  and  $0.50$ , the BSTO forms the matrix and the  $\text{Sm}_2\text{O}_3$  forms the columns, whereas for  $x = 0.75$ , the  $\text{Sm}_2\text{O}_3$  forms the matrix and the BSTO forms the columns.<sup>48</sup> TEM images of  $(\text{BSTO})_{1-x}-(\text{Sm}_2\text{O}_3)_x$  films comparing lower and higher  $x$  values, where the BSTO either forms the matrix ( $x = 0.25$  and  $0.50$ ) or the columns ( $x = 0.75$ ), are shown in Figure. 4.1 (a), (b) and (c), respectively.

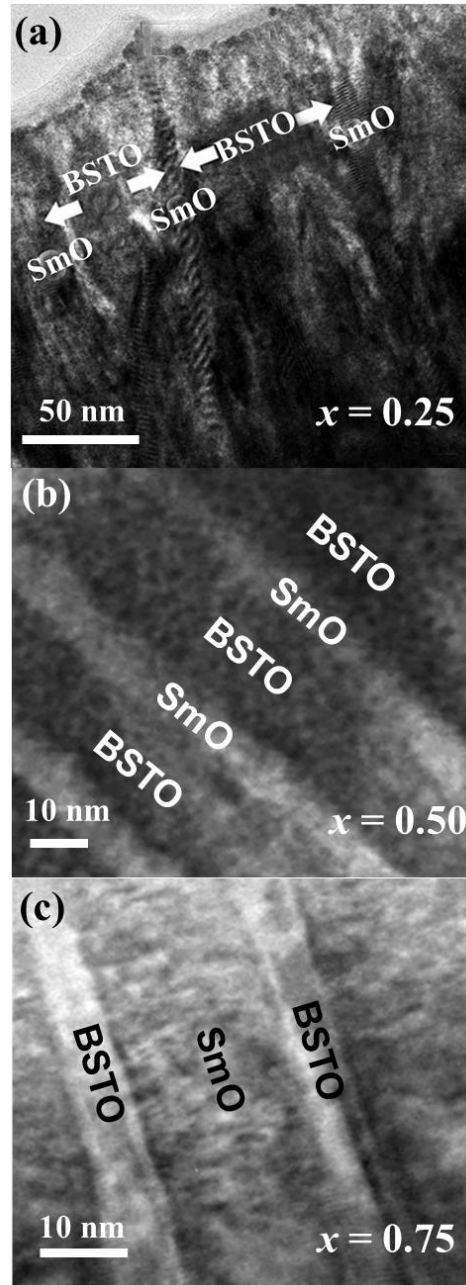


Figure 4.1. Microstructures of  $(\text{BSTO})_{1-x}-(\text{Sm}_2\text{O}_3)_x$  nanocomposite films for different  $x$  values. Transmission electron micrographs for (a)  $x = 0.25$ , (b)  $x = 0.50$  and (c)  $x = 0.75$ . (Figure from <sup>27</sup>)

Figure 4.2 is a sketch of the microstructure of the  $x = 0.25$  and  $0.50$  films. The column diameters are  $\sim 10$  nm with 10 - 80 nm spacing, depending on  $x$ . The SEM plan view image in the inset of Figure 4.2 clearly reveals the vertically aligned nano-columns of  $\sim 10$  nm width embedded in a film matrix.<sup>27</sup>

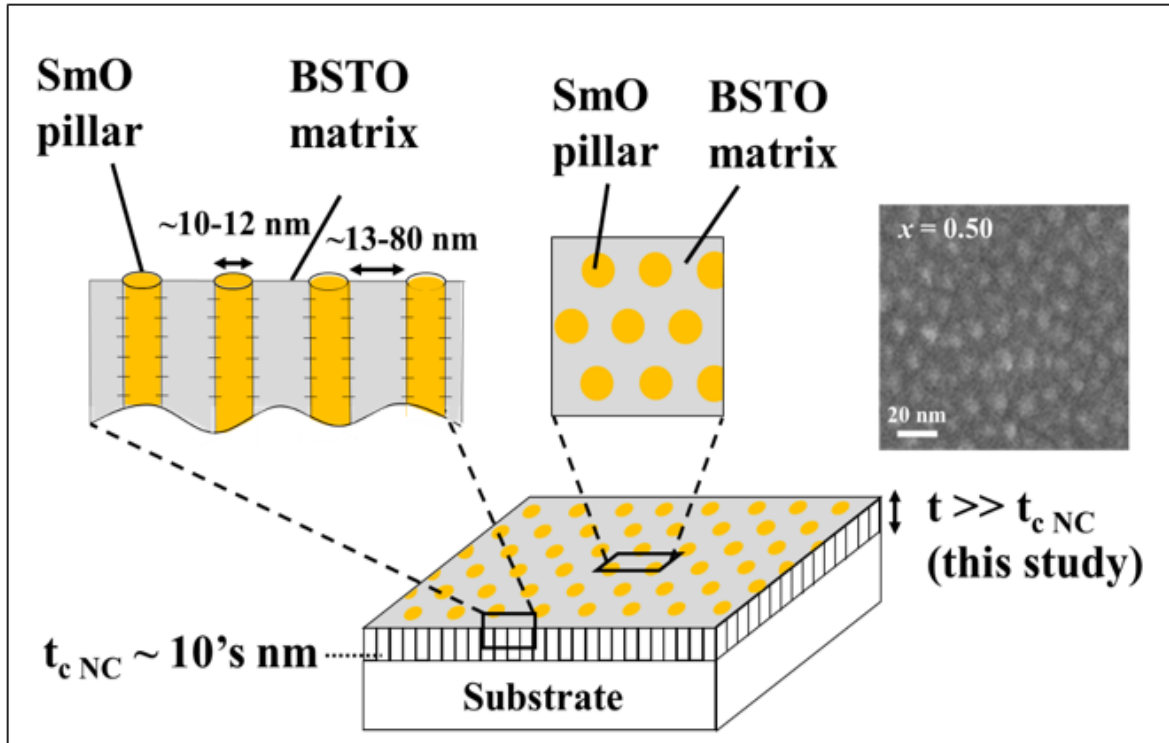


Figure 4.2. Schematic diagram showing nanocomposite structure for BSTO matrix and  $\text{Sm}_2\text{O}_3$  pillar, and plan view SEM image of surface of  $x = 0.50$  film revealing nanopillars. (The TEM work is undertaken courtesy of Prof. Haiyan Wang's group from Texas A&M University). (Figure from <sup>27</sup>)

As shown in an earlier paper from the group,<sup>48</sup> the epitaxial relationship of the BSTO and  $\text{Sm}_2\text{O}_3$  phases on the SRO/STO substrate can be denoted based on the lattice matching as  $(002)\text{BSTO} // (004) \text{Sm}_2\text{O}_3 // (002)\text{SRO} // (002)\text{STO}$  in the *out-of-plane* direction and  $(020)\text{BSTO} // (220) \text{Sm}_2\text{O}_3 // (020)\text{SRO} // (020)\text{STO}$  in the *in-plane* direction. The  $[220]$  direction of  $\text{Sm}_2\text{O}_3$  phase is parallel to the  $[020]$  of the STO substrate phase because the unit cell of  $\text{Sm}_2\text{O}_3$  grows  $45^\circ$  rotated relative to the STO unit cell. This rotation is energetically favorable as it enables  $\text{Sm}_2\text{O}_3$  lattice matching

of  $1.0927 \text{ nm} \times \sqrt{2} = 1.5453 \text{ nm}$  with 4 unit cells of STO [100] ( $4 \times 0.3905 \text{ nm} = 1.5620 \text{ nm}$ ) in STO.<sup>4</sup> The lattice parameters of the films were determined from a combination of XRD reciprocal space maps (RSMs) of the asymmetric (113) reflections and  $2\theta - \omega$  scans of the symmetric (00l) peaks. Figure 4.3 shows the symmetric (00l) peaks from  $2\theta - \omega$  scans and Figure 4.4. shows the asymmetric (113) reflections of STO and BSTO as well as (048) reflections of  $\text{Sm}_2\text{O}_3$  peaks.

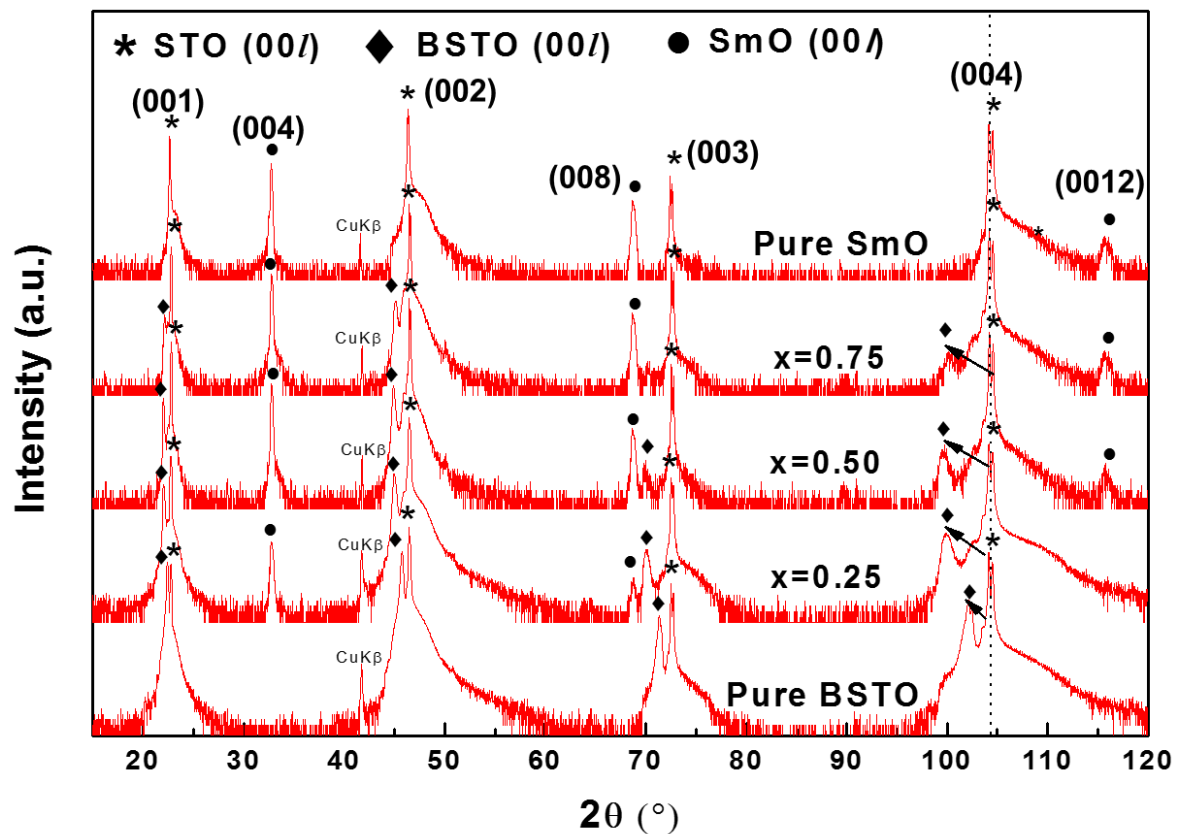


Figure 4.3.  $2\theta - \omega$  scans showing symmetric (00l) peaks of BSTO-  $\text{Sm}_2\text{O}_3$  VAN with various  $\text{Sm}_2\text{O}_3$  fraction,  $x$ . The *out-of-plane* strain of the BSTO phase is determined from the high angle peak BSTO (004) as it increases the accuracy in determining lattice parameter.<sup>117</sup>

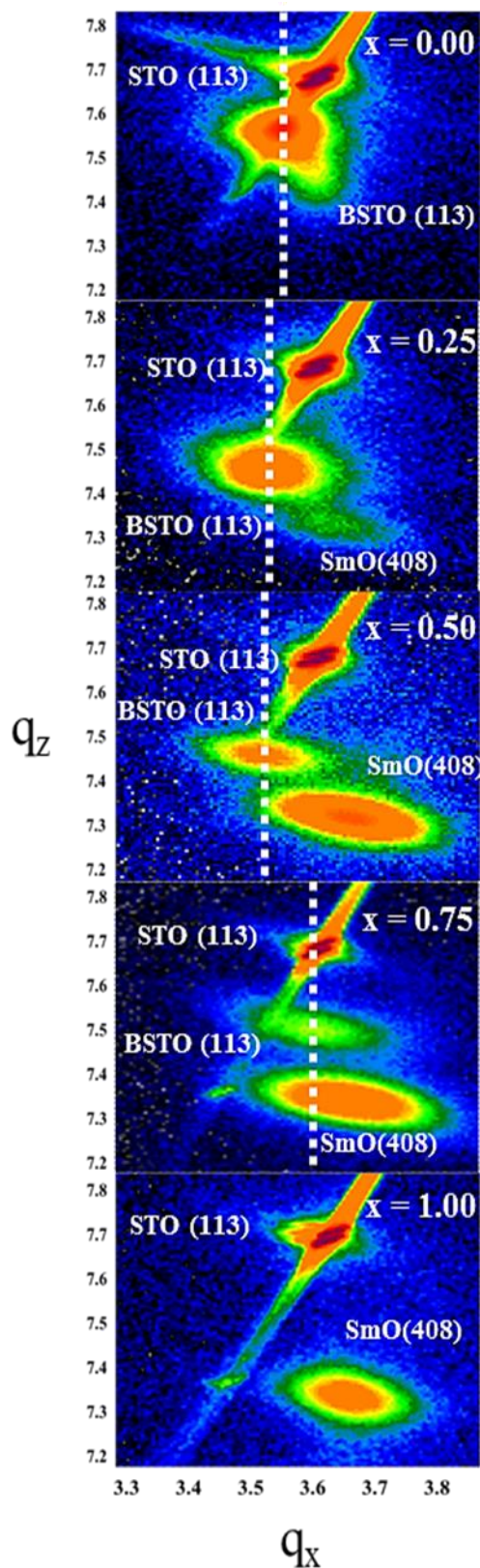


Figure 4.4. Reciprocal space maps of  $(\text{BSTO})_{1-x}-(\text{Sm}_2\text{O}_3)_x$  nanocomposite films showing the (113) perovskite peaks of STO and BSTO as well as (048) peaks of  $\text{Sm}_2\text{O}_3$ , with compositions ranging from pure BSTO ( $x = 0.00$ ) to pure  $\text{Sm}_2\text{O}_3$  ( $x = 1.00$ ). The dotted line represents the  $q_x$  of the centre of BSTO peaks. (Figure from <sup>27</sup>)

The analysis assumes that the BSTO is tetragonal which is expected from the literature.<sup>48</sup> Concentrating first on the RSMs and *in-plane* parameters, we focus on the position of the BSTO (113) peaks along  $q_x$ . In RSM,  $q_x$  and  $q_z$  represents the reciprocal lattice parameter of the material under study. Essentially, it is a mathematical way to represent the lattice spacing between reflected atomic planes in a material. Larger values of  $q$  represents smaller lattice spacing and vice versa. The position of the centers of these peaks along  $q_x$  is shown by the white dashed lines and they indicate how the *in-plane* lattice parameters change with  $x$ . Figure 4.5 is a plot to quantify the degree of shifting of BSTO(113) peak from its unstrained position. In relation to Figure 4.4, At  $x = 0.00$ , a broad BSTO (113) peak is observed and it is located more towards the left side compared to the STO (113) peak, indicative of a fully relaxed film, and an *in-plane* lattice parameter of BSTO which is larger than STO. The full relaxation is expected for a film of this large thickness. As  $x$  increases from 0.00 to 0.25, the (113) peaks are shifted markedly to the further left indicating a strong tensile strain *in-plane*. The peak is also sharpened. Together these findings indicate that there is progressively increased strain control of the BSTO by the  $\text{Sm}_2\text{O}_3$  phase with increasing  $x$ . For  $x = 0.50$ , the peak remains in approximately the same position in  $q_x$  as at  $x = 0.25$  but is sharpened much further (especially in the  $q_z$  direction) indicative of full strain control of BSTO by the  $\text{Sm}_2\text{O}_3$  phase through the vertical interface. This is consistent with the BSTO lateral spacing between the pillars decreasing from  $\sim 80$  nm to  $\sim 10$ -15 nm, thereby allowing for full vertical epitaxial strain control in the BSTO, i.e., insufficient lateral dimension of BSTO to allow for stress relaxation. As the  $\text{Sm}_2\text{O}_3$  fraction is increased from  $x = 0.50$  to  $x = 0.75$ , the BSTO (113) peak position shifts strongly to the right, being at a similar position to the STO substrate peak. At this large  $x$  value, the  $\text{Sm}_2\text{O}_3$  film forms the matrix with the BSTO forming the nanocolumns of  $\sim 10$  nm size in the  $\text{Sm}_2\text{O}_3$  (Figure 4.2). The BSTO pillars are under compressive strain *in-plane* which represents a complete switch from the tensile strain found when the BSTO is the matrix for  $x = 0.25$  and 0.50.

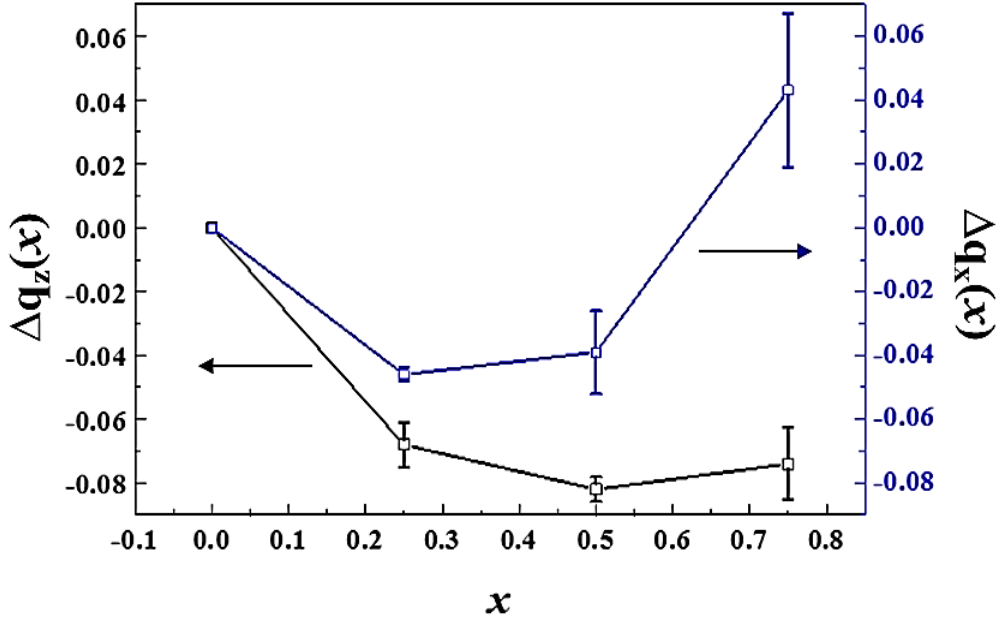


Figure 4.5. *In-plane* and *out-of-plane* shift ( $\Delta q_x$  and  $\Delta q_z$ ) of the (113) BSTO reciprocal peak positions for different  $x$  values with respect to  $x = 0.00$ . (Figure from <sup>27</sup>)

The *out-of-plane*  $c$  lattice parameters of the BSTO phase were obtained from the  $2\theta - \omega$  scans (Figure 4.3). There was a clear increase in *out-of-plane* lattice parameter,  $c$ , with  $x$ . This trend is also observed from downward shift of the (113) BSTO peak centers in the RSMs with increasing  $x$ . The *in-plane* lattice parameters,  $a$ , were calculated based on the (113) peak positions in the RSM scans. Both  $a$  and  $c$  lattice parameters are plotted as a function of  $x$  and thickness (300 nm - 1000 nm) in Figure 4.6. The bulk cubic BSTO lattice parameter is also included for comparison. Across the entire thickness range, the pure BSTO ( $x = 0.00$ ) films are fully relaxed, as confirmed by their lattice parameter values being the same as the bulk values for BSTO. This result is expected since at 300 nm and above, the films are no longer under epitaxial strain control by the substrate, i.e., all the films are well above the critical thickness and are relaxed. On the other hand, for all  $x$  values  $>0.00$  and for all thicknesses, the  $c$  axis is larger than the bulk value, and hence, the BSTO is always in tension *out-of-plane*. The *out-of-plane* expansion results from vertical strain control of the BSTO (elastic modulus  $\sim 80$  GPa) by the stiffer  $\text{Sm}_2\text{O}_3$  (elastic modulus  $\sim 220$  GPa).<sup>118-119</sup>

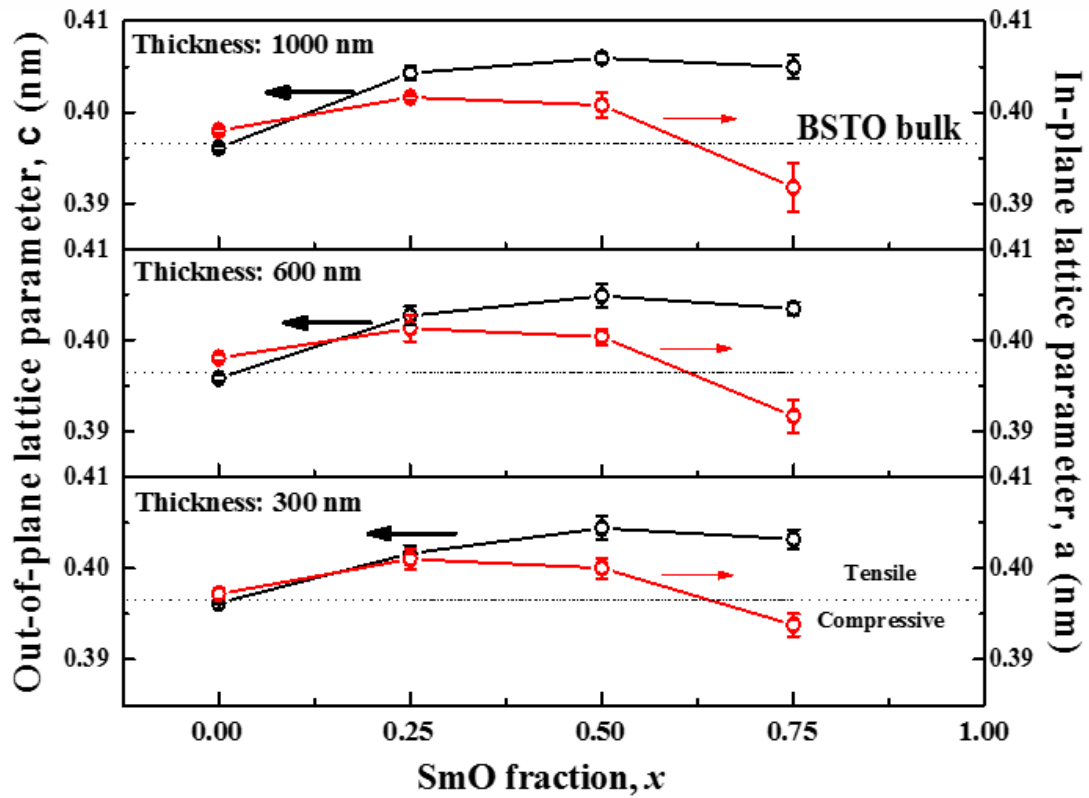


Figure 4.6. *Out-of-plane* and *in-plane* lattice parameters of BSTO for various thicknesses versus  $x$ . (Figure from <sup>27</sup>)

Looking now at the *in-plane* lattice parameters of BSTO, as already discussed qualitatively for the RSMs of Figure 4.4, we see that with increasing  $x$ , the *in-plane* parameters of the BSTO increase rapidly upon introduction of a moderate fraction ( $x = 0.25$ ) of  $\text{Sm}_2\text{O}_3$  into the films, but then stay approximately the same from  $x = 0.25$  to  $x = 0.50$ . For both these  $x$  values, the  $\text{Sm}_2\text{O}_3$  phase is in the form of strain-controlling nanopillars in the BSTO matrix. Since both  $a$  and  $c$  are expanded for these compositions, the films are exhibiting an auxetic-like behavior. Depending on  $x$  and film thickness, the tensile strain level can be as high as 2.4% for  $x = 0.50$  and 1000 nm thickness. Indeed, the vertical strain state is highest in the thickest films, which is opposite to the case of plain films where strain relaxes upon thickness increase. This is a unique feature of nanocomposite films.<sup>30</sup> At  $x = 0.75$ , the *in-plane* parameter decreases markedly and

now the BSTO appears to be in slight compression. As already mentioned, at this  $x$  value, the BSTO forms fine nanopillars ( $\sim 10$  nm) embedded within a  $\text{Sm}_2\text{O}_3$  matrix, the lateral thickness of  $\text{Sm}_2\text{O}_3$  between the pillars being  $\sim 40$  nm (Figure 4.2).

## 4.3 Origin of Plane Strain States in $(\text{Ba}_{0.6}\text{Sr}_{0.4}\text{TiO}_3)_{1-x}-(\text{Sm}_2\text{O}_3)_x$ VAN

### 4.3.1. For $x = 0.25$ and $x = 0.50$

In order to understand the observed unusual auxetic-like effect in the films, we employ a simple model to calculate the BSTO lattice parameter. To determine the *out-of-plane*  $c$  parameter, we consider the vertical lattice parameter control of the BSTO phase by the  $\text{Sm}_2\text{O}_3$ , and to determine the *in-plane*  $a$  parameter, we consider the *in-plane* thermal shrinkage as well as elastic behavior of the film upon cooling after growth.

First we consider the *out-of-plane* strain in the BSTO. We first note that the influence of the substrate on the *out-of-plane* strain in the nanocomposite case is negligible. This is because the film thicknesses studied here ( $>300$  nm) are all above the critical thickness for the nanocomposite,  $t_{cNC}$ , which is a few 10's of nm thickness,<sup>4</sup> as shown in Figure 4.2.  $t_{cNC}$  depends on the vertical column/matrix area relative to the substrate/film area. Above  $t_{cNC}$ , the vertical column/matrix area exceeds the substrate/film area and then the substrate does not determine the strain state of the film. Instead, the stiffer phase in the VAN determines the strain state of the softer phase. We note that the critical thickness for standard planar films (or superlattices),  $t_{cPL}$ , above which the film strain is relaxed and is no longer fixed by epitaxy control from the substrate, is much larger than for nanocomposite films. The value of  $t_{cPL}$  is  $\sim 100$  nm.<sup>28</sup>

120

The *out-of-plane* strain in the BSTO is dominated by vertical epitaxy between it and the  $\text{Sm}_2\text{O}_3$ , no matter whether the  $x$  value is high or low: the BSTO phase is strained by the much stiffer  $\text{Sm}_2\text{O}_3$  pillars. Domain matching epitaxy (DME) determines how many lattices of the respective phases match with one another and this controls the overall strain level.<sup>4</sup> From Figure 4.6, it is observed that for all film thicknesses, the

*out-of-plane* lattice parameter increases with  $x$ . This is explained by the lateral size of the BSTO decreasing with increasing  $x$ , which means the  $\text{Sm}_2\text{O}_3$  can exert a greater influence on the BSTO with less strain relaxation taking place. We do not calculate the variation of the *out-of-plane* lattice parameter with  $x$  as it is not easy to predict the extent of strain relaxation with  $x$ .

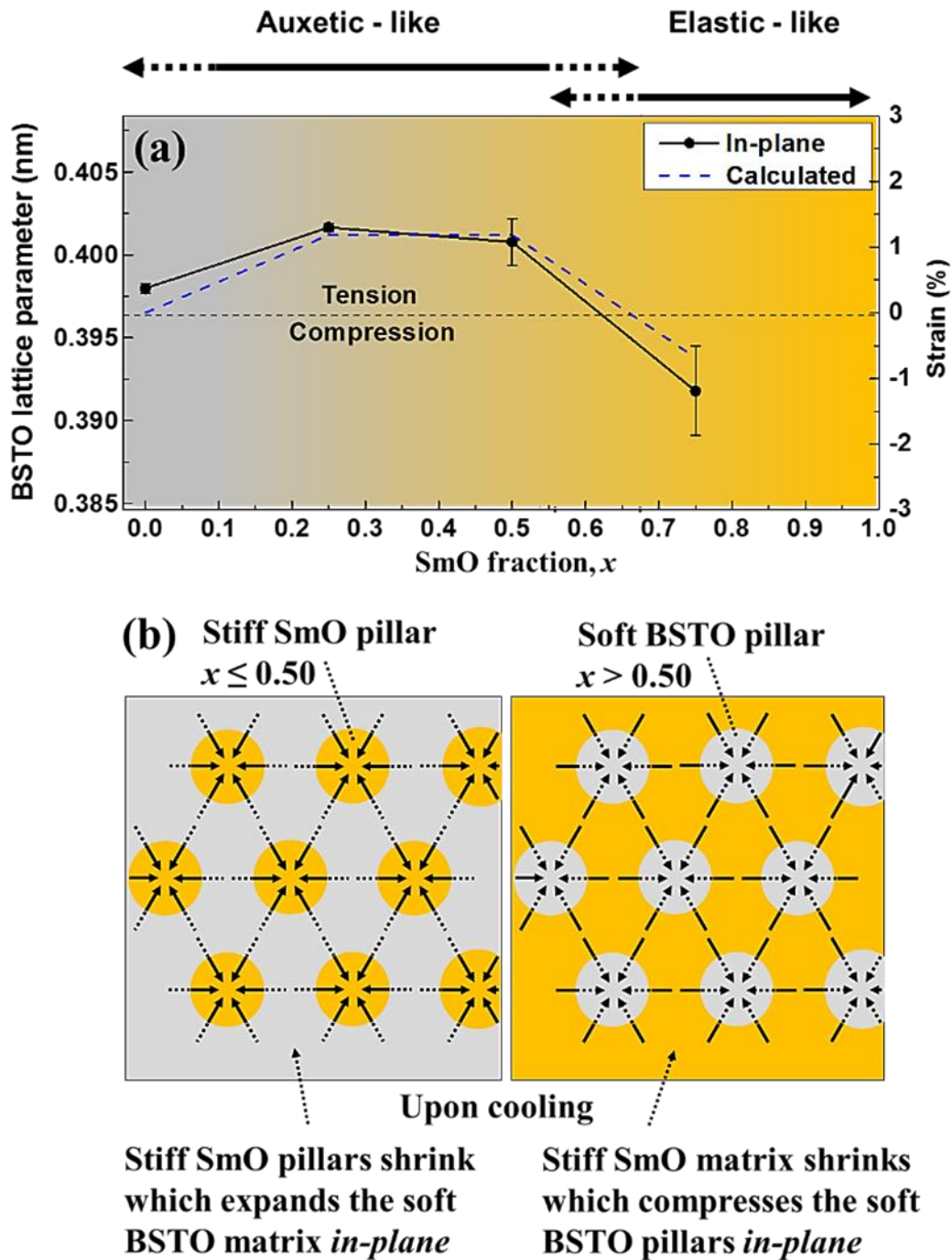


Figure 4.7 (a) Experimental and modelled values of BSTO *in-plane* lattice parameter (left hand axis) and corresponding *in-plane* strain (right hand axis) versus  $x$  for the 1000

nm thickness nanocomposite films. (b) Schematic diagram showing the  $\text{Sm}_2\text{O}_3$  thermal shrinkage effect on the *in-plane* BSTO strain upon cooling films from the growth temperature. Low  $x$  (left image) and high  $x$  (right image). (Figure from <sup>27</sup>)

In planar multilayers, the substrate controls the *in-plane* lattice parameters with the *out-of-plane* lattice parameters controlled by the resulting elastic deformation in accordance with Poisson effect. For the nanocomposite films, a very different situation occurs. At above  $t_{cNC}$  (i.e. at all the film thicknesses of this study), as previously mentioned, the substrate does not play a role in setting the lattice parameters.

Next, we consider the *in-plane* strain in the BSTO. Upon cooling, from the growth temperature, the BSTO thermal shrinkage is very close to STO, and hence, the room temperature BSTO lattice parameters will not be influenced by the substrate. This is confirmed by the  $x = 0.00$  lattice parameters being the same as the bulk values (Figure 4.7 (a)). Subsequently, it is important to consider the influence of the  $\text{Sm}_2\text{O}_3$  nanopillars on the *in-plane* strain of BSTO. The soft BSTO matrix is “epitaxially anchored” everywhere by the dense, stiff, scaffold  $\text{Sm}_2\text{O}_3$  pillars of spacing  $\sim 80$  nm ( $x = 0.25$ ) and  $\sim 10$ - $15$  nm ( $x = 0.50$ ), embedded in the matrix. In other words, the BSTO and  $\text{Sm}_2\text{O}_3$  are “glued,” together with the stiffer  $\text{Sm}_2\text{O}_3$  controlling the behavior of the softer BSTO.

The pillars’ contraction is not limited to or by the substrate contraction since the area that each pillar has with the substrate is minimal compared to their length which is significantly above  $t_{cNC}$ . Hence, upon cooling from the growth temperature, the  $\text{Sm}_2\text{O}_3$  pillars can contract more freely than BSTO because of its higher stiffness. The epitaxial anchoring of the BSTO to the  $\text{Sm}_2\text{O}_3$  will mean that BSTO is prevented from contracting (as shown schematically in Figure 4.7 (b)). Thus, there is an *in-plane* expansion of the BSTO lattice of exactly opposite magnitude to the contraction of the  $\text{Sm}_2\text{O}_3$ ;

$$\epsilon_{//\text{BSTO}} = -\epsilon_{//\text{Sm}_2\text{O}_3}; \quad \epsilon_{//\text{Sm}_2\text{O}_3} = \alpha(\text{Sm}_2\text{O}_3)\Delta T \quad (4.1),$$

with  $\epsilon_{//\text{BSTO}}$  is the *in-plane* strain in the BSTO phase,  $\epsilon_{//\text{Sm}_2\text{O}_3}$  is the *in-plane* strain in the  $\text{Sm}_2\text{O}_3$ ,  $\alpha_{\text{Sm}_2\text{O}_3}$  is the coefficient of thermal expansion of the  $\text{Sm}_2\text{O}_3$  phase<sup>121</sup> which is  $8.8 \times 10^{-6} \text{ K}^{-1}$  and  $\Delta T$  is taken to be  $-775 \text{ K}$ , i.e., the difference between the growth temperature and room temperature. Hence,  $\epsilon_{//\text{BSTO}} = 8.8 \times 10^{-6} \text{ K}^{-1} \times 775 = 0.68\%$ .

Furthermore, the expansion of the BSTO by the  $\text{Sm}_2\text{O}_3$  (both *in-plane* and *out-of-plane*) will prevent the cubic to tetragonal phase transformation in BSTO from taking place which would normally occur near room temperature for BSTO of this composition.<sup>122</sup> The absence of a phase transformation leads to a correction of *in-plane* lattice parameter expansion of  $\sim +0.50\%$ , i.e., the opposite sign of the normal contraction of the *in-plane* lattice parameters upon cooling through ferroelectric  $T_C$ .<sup>123</sup> We note that for  $x$  values between 0.00 and 0.25, the distance between  $\text{Sm}_2\text{O}_3$  nanopillars will become too large to allow the anchoring to be effective at all places in the BSTO matrix. Hence, at places far away from the  $\text{Sm}_2\text{O}_3$  pillars, the BSTO will be relaxed and the auxetic-like effect will then not occur.

The above two calculated *in-plane* expansions of the BSTO, i.e. (1) the thermal contraction of the  $\text{Sm}_2\text{O}_3$ , and (2) the absence of the cubic to tetragonal phase transition, giving (1+2), the total *in-plane* expansion of the BSTO, are given in Table 4.1, together with the sum of these two expansions, and the measured values. The calculated and measured *in-plane* lattice parameters (for the 1000 nm film) are also shown in Figure 4.4 (a). The calculated total *in-plane* strain values compare favorably to the measured values.

$x$	$\varepsilon_{\parallel \text{BSTO}} (-\alpha \text{ Sm}_2\text{O}_3 \Delta T)$	Tetragonal-cubic correction ( $c/a=1.01$ )	Calculated <i>in-plane</i> strain	Measured <i>in-plane</i> strain	Calculated BSTO <i>in-plane</i> lattice parameter (Å)	Measured BSTO <i>in-plane</i> lattice parameter (Å)
0.25	0.68%	0.50%	1.18%	$1.31 \pm 0.07\%$	4.012	$4.017 \pm 0.003$
0.50	0.68%	0.50%	1.18%	$1.08 \pm 0.35\%$	4.012	$4.008 \pm 0.014$
0.75	-0.68%	N/A	-0.68%	$-1.19 \pm 0.68\%$	3.938	$3.918 \pm 0.027$

Table 4.1. Experimental and calculated value of the *in-plane* BSTO lattice parameters in  $(\text{BSTO})_{1-x}(\text{Sm}_2\text{O}_3)_x$  nanocomposite thin film. The calculated BSTO *in-plane* lattice parameters were from thermal expansion mismatch with  $\text{Sm}_2\text{O}_3$  as well as the absence of ferroelectric (cubic to tetragonal) phase transition. (Table from <sup>27</sup>)

- 
- STO lattice parameters  $a = b = c = 3.905 \text{ \AA}$  (JCPDS 35-0734)
  - BSTO lattice parameters  $a = b = c = 3.965 \text{ \AA}$  (JCPDS 34-0411)
  - $\text{Sm}_2\text{O}_3$  lattice parameters  $a = b = c = 10.927 \text{ \AA}$  (JCPDS 15-0813)

We note that in the *out-of-plane* direction, upon cooling there will also be some contraction of the BSTO lattice owing to the  $\text{Sm}_2\text{O}_3$  contraction and the higher stiffness  $\text{Sm}_2\text{O}_3$  forcing the BSTO to follow it, just as for the *in-plane* case. Overall, however, the *c*-axis lattice parameter will still be expanded considerably from the DME vertical epitaxy strain.

#### 4.3.2. For $x = 0.75$

At  $x = 0.75$ , the BSTO now forms the nanocolumns (of  $\sim 10 \text{ nm}$  diameter) and the  $\text{Sm}_2\text{O}_3$  forms the matrix (Figure 4.1 (c)). In all the film thicknesses, the  $\text{Sm}_2\text{O}_3$  has its fully relaxed bulk lattice parameter, i.e.,  $1.0927 \text{ nm}$ . This bulk lattice parameter is

expected since although the film is a nanocomposite, it will not have any additional strain influence from the BSTO pillars since they are softer than the matrix. Also, the films have thickness above  $t_{cPL}$ , and so, full strain relaxation is expected. This is very different to the mirror situation of the  $x = 0.25$  composition where BSTO is the matrix and does not relax to the bulk lattice parameter because the stiff  $\text{Sm}_2\text{O}_3$  pillars control the behavior of the matrix, as discussed above. The *in-plane* strain in the BSTO nanopillars will be equivalent to the thermal shrinkage strain from the enveloping, stiffer  $\text{Sm}_2\text{O}_3$  matrix which radially squeezes the pillars upon cooling of the film after growth (see schematic diagram in Figure 4.7 (b)). Here, since the BSTO pillar is already in *out-of-plane* tension and *in-plane* compression (tetragonal), the cubic to tetragonal phase transition is not prevented from occurring as in the  $x = 0.25$  and 0.50 cases. The overall BSTO compression is therefore just  $\varepsilon_{//\text{BSTO}} = \varepsilon_{//\text{Sm}_2\text{O}_3} = \alpha_{\text{Sm}_2\text{O}_3} \Delta T = -0.68\%$ . The value is consistent with the measured parameter as shown in Table 4.1.

## 4.4 Ferroelectric Properties

In this section, the ferroelectric properties of the BSTO-  $\text{Sm}_2\text{O}_3$  films are discussed. Figure 4.8 shows the P-E hysteresis loops of the pure  $\text{Sm}_2\text{O}_3$  with 300 nm thickness and Figure 4.9 shows the hysteresis loops for BSTO-  $\text{Sm}_2\text{O}_3$  films with various compositions compared to pure BSTO and  $\text{Sm}_2\text{O}_3$  films of similar thickness. The saturation polarization,  $P_s$ , of the BSTO-  $\text{Sm}_2\text{O}_3$  nanocomposite films (taken at 300 kV/cm and normalized by the area of BSTO in each film) increases monotonically with an increase of  $x$  in the order,  $P_s, x = 0.75 \gg P_s, x = 0.50 \gg P_s, x = 0.25 \gg P_s, x = 0$ . At higher film thickness, the required voltage to achieve the same level of electric field was beyond the capability of the instrument and hence only data from 300 nm was shown. As expected, the pure  $\text{Sm}_2\text{O}_3$  films are not ferroelectric (Figure 4.8) and hence do not contribute to the ferroelectric polarization of the BSTO-  $\text{Sm}_2\text{O}_3$  nanocomposite films. The  $P_s, x = 0$  (pure BSTO) value is similar to the literature for similar-composition BSTO films.<sup>122</sup> The  $P_s, x = 0.75$  value is much higher than BSTO or BTO films from the literature (by almost 300%).<sup>124</sup>

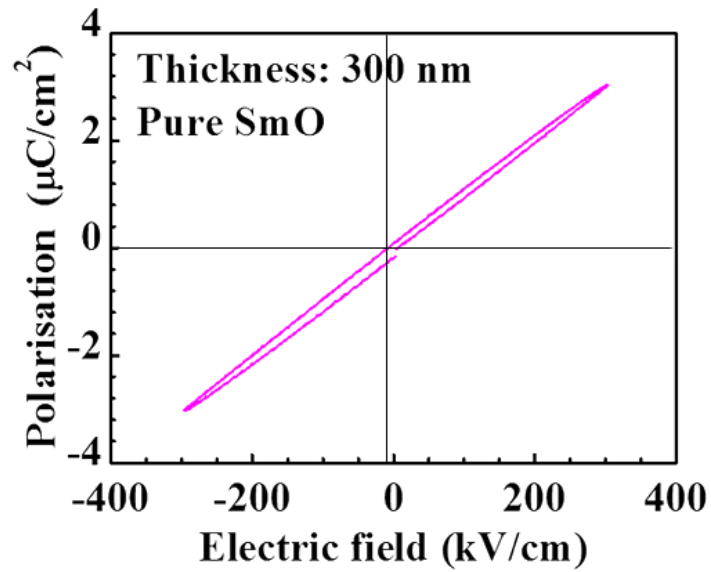


Figure 4.8 P-E hysteresis loop for pure  $\text{Sm}_2\text{O}_3$  film with 300 nm thickness. (Figure from <sup>27)</sup>)

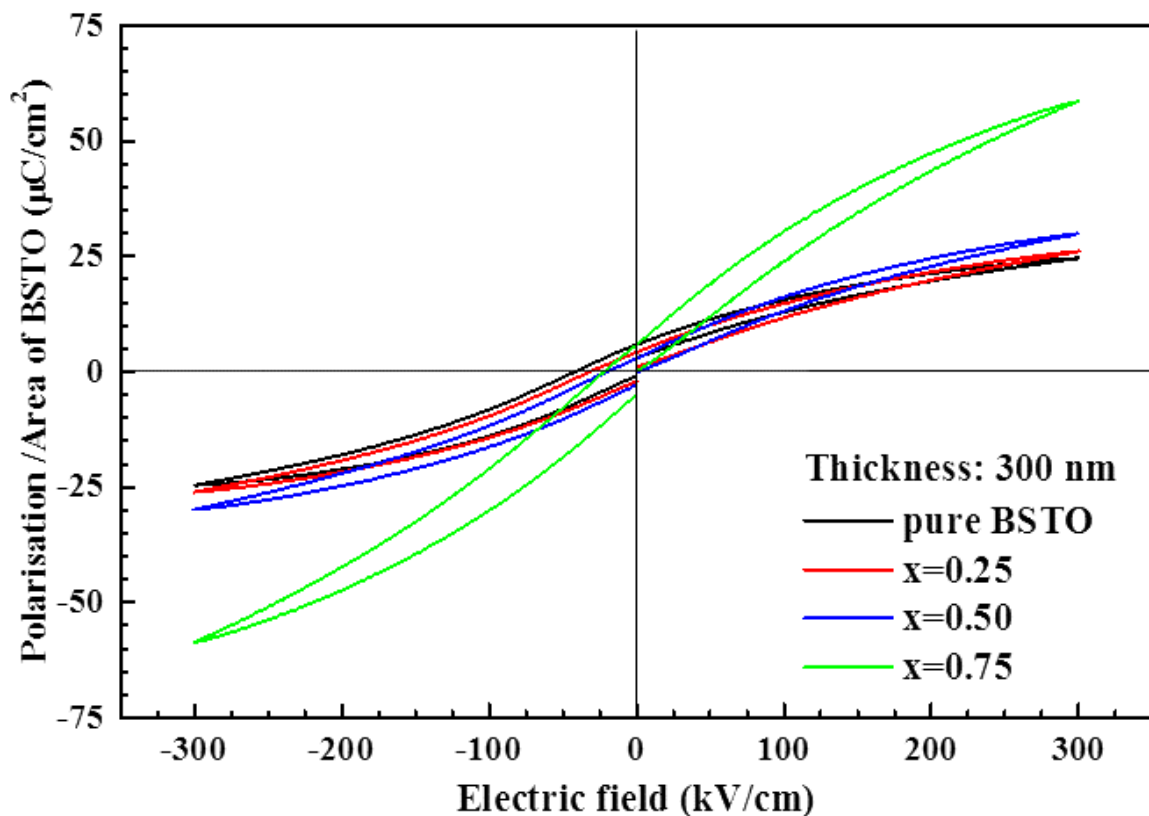


Figure 4.9. Polarization versus electric field hysteresis loops for  $(\text{BSTO})_{1-x}-(\text{Sm}_2\text{O}_3)_x$  films for different  $x$  values. (Figure from <sup>27)</sup>)

Since the *out-of-plane* lattice strain is similar for  $x = 0.50$  and  $x = 0.75$  but since  $P_s$  is much larger for  $x = 0.75$ , it is clear the magnitude of  $P_s$  does not depend on the *out-of-plane* tension alone, but also the *in-plane* compression of BSTO. The nanoscale nature of the BSTO, combined with the large *in-plane* compression, are clearly important additional factors for enhancing  $P_s$ .

We recall that for  $x = 0.75$ , we have clean, highly tetragonally distorted,  $\sim 10$  nm nanopillars, which results in high tetragonality ( $c/a$  ratio). Whereas at  $x = 0.50$ , we have an auxetic-like strained BSTO matrix with a high density of  $\text{Sm}_2\text{O}_3$  nanopillars penetrating it. The expansion of the BSTO for  $x = 0.25$  and  $0.50$  has the additional effect of preventing a bulk-like phase transition from cubic to tetragonal in the BSTO from occurring. Having said that, a relatively low polarization value was still observed. This is because although the abrupt phase transition that manifests in abrupt lattice parameter change was absent, the lattice structures of the BSTO films in those compositions are not perfect cubic, as shown in Figure 4.6 in which the in-plane and out-of-plane lattice parameters are at different values, albeit only small differences (tetragonality).

Atomic-force microscopy (AFM) was used to study the topography of the nanocomposite film, as shown in Figure 4.10 (a) which shows nano-pillars of around 10 nm width. Piezo-response force microscopy (PFM) measurements with multiple poling confirm the strong ferroelectric nature of the BSTO-  $\text{Sm}_2\text{O}_3$ ,  $x = 0.75$  films. The *out-of-plane* piezo-response phase contrast images (shown in Figure 4.10 (b)) are observed with multiple switching when an AC modulating voltage of  $\pm 5$  V and DC bias of  $\pm 10$  V (Figure 4.10 (c)) were applied to the SRO bottom electrode at an excitation frequency of 10 kHz. The  $45^\circ$  rotated dark and bright regions with various scan areas of  $8 \mu\text{m} \times 8 \mu\text{m}$ ,  $5 \mu\text{m} \times 5 \mu\text{m}$ , and  $2 \mu\text{m} \times 2 \mu\text{m}$  show the domain reorientations corresponding to  $-10$  V and  $+10$  V. This observation supports the strong ferroelectric polarization measured in the P-E loops (Figure 4.9). It is also important to note that the phase contrast image in Figure 4.10 (b) has a much larger area ( $8 \mu\text{m} \times 8 \mu\text{m}$ ,  $5 \mu\text{m} \times 5 \mu\text{m}$ , and  $2 \mu\text{m} \times 2 \mu\text{m}$ ) compared to the pillar size which is  $\sim 10$  nm in width. This

confirms that the phase contrast image is due to real piezoelectric response from the poled BSTO phase rather than leakage current through the grain boundaries between nano-pillars and matrix.

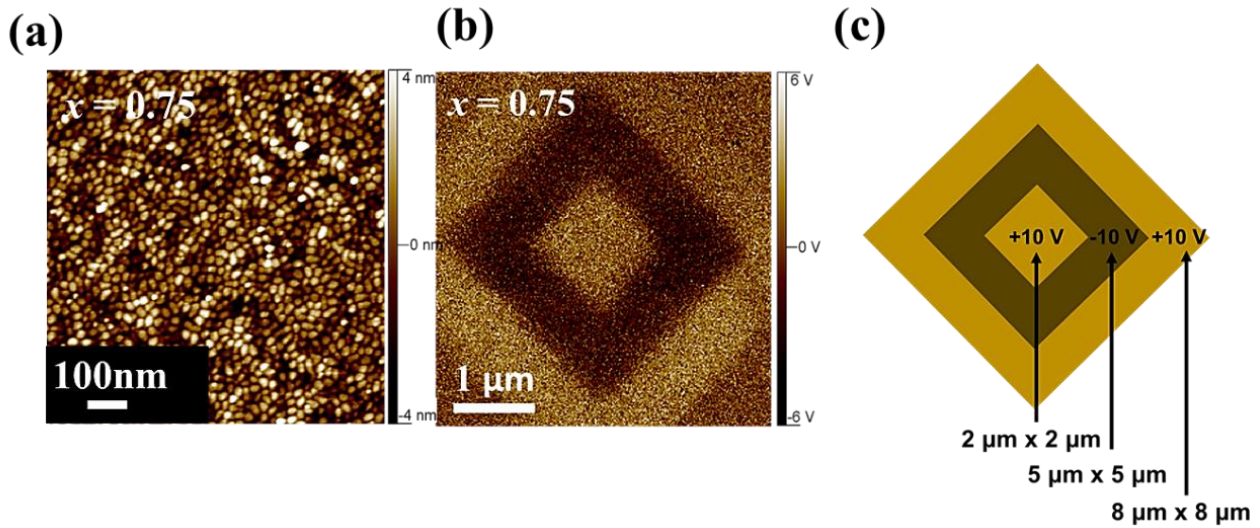


Figure 4.10. (a) AFM topography image of  $x = 0.75$  film with  $1 \mu\text{m} \times 1 \mu\text{m}$  scan area, (b) piezoresponse phase image of  $x = 0.75$  film with multiple polings with different scan areas, and (c) schematic of the multiple poling areas with an applied DC bias of  $\pm 10$  V. (AFM and piezoresponse phase image experiment was conducted with the help of Dr. Ahmed Kursumovic) (Figure from <sup>27</sup>)

In summary, strain states for films of 300 nm, 600 nm and 1000 nm thick heteroepitaxial nanocomposite of  $(\text{Ba}_{0.6}\text{Sr}_{0.4}\text{TiO}_3)_{1-x}-(\text{Sm}_2\text{O}_3)_x$  on  $\text{SrTiO}_3$  were studied.<sup>27</sup> Unusual auxetic-like tensile strain was observed for  $x = 0.25$  and  $x = 0.50$ , whereas elastic-like strain was observed for  $x = 0.75$  which results in high tetragonality. The *in-plane* strain and lattice parameters of BSTO were modeled by considering the influence that the stiff  $\text{Sm}_2\text{O}_3$  has on the softer BSTO upon cooling the films from the growth temperature. Very good agreement was found between calculation and experiment. For  $x = 0.25$  and  $0.50$ , the BSTO matrix is expanded *in-plane* as a result of the thermal shrinkage of the stiff  $\text{Sm}_2\text{O}_3$  nanopillars which are epitaxially anchored to

the BSTO matrix and hence control its expansion/contraction. The expansion of the BSTO prevents the cubic to tetragonal phase transition in the BSTO from occurring. Overall, the BSTO lattice is expanded both *in-plane* and *out-of-plane*, the *out-of-plane* lattice parameter being determined by vertical heteroepitaxial straining of the BSTO by the Sm<sub>2</sub>O<sub>3</sub>. For  $x = 0.75$ , the Sm<sub>2</sub>O<sub>3</sub> forms the matrix and the BSTO forms the pillars, and it acts to “squeeze” the nanopillars *in-plane*. Hence, for  $x = 0.75$ , the BSTO shrinks *in-plane*, while it is still expanded *out-of-plane* as before. Owing to this high *out-of-plane* tension and *in-plane* compression, the BSTO shows a very high  $P_s$ ,  $x = 0.75$  value of  $\sim 60 \mu\text{C}/\text{cm}^2$  for a 300 nm film thickness, much higher than standard single layer BSTO or BTO films. All in all, we have demonstrated a very simple way to create unusual auxetic-like strain states in strongly correlated thin film metal oxides, thus allowing for radically new and different physical properties to be engineered into them.

# Chapter 5 Turning Antiferromagnetic SSMO into A Ferromagnetic Using VAN

## 5.1. Magnetism and Magneto-Transport

Magnetism is a property of materials at atomic or sub-atomic level upon an application of magnetic field. The basic definition of magnetism lies in the orbital and spin motions of electrons and the interaction among the electrons. In fact, all matter is magnetic and some materials are much more magnetic than others. The main distinction between how matter interacts with magnetic fields corresponds to the interaction of atomic magnetic moments. There are a few materials which are naturally magnetic and can be turned into magnets. For example, iron, hematite, magnetite and ionized gases.<sup>125</sup>

The theory of magnetism is a very broad field, and is based upon the idea of the quantum mechanical exchange energy which causes electrons with parallel spins to have lower energy than anti-parallel spins. Paramagnetism, which is the case for most elements, exhibit an internally induced magnetic field in reaction to external magnetic field, resulting in a weak attraction to external magnetic field. Diamagnetism, on the other hand, involves repulsion of an external magnetic field by inducing an internal magnetic field in the opposite direction. The internal field in paramagnetism and diamagnetism is non-existent when the external magnetic field is removed.

Ferromagnetic materials exhibit parallel alignment of magnetic moments resulting in large net magnetization even in the absence of a magnetic field. Anti-ferromagnetism represents the case of all sub-lattice moments are exactly equal but opposite and the net moment is zero.

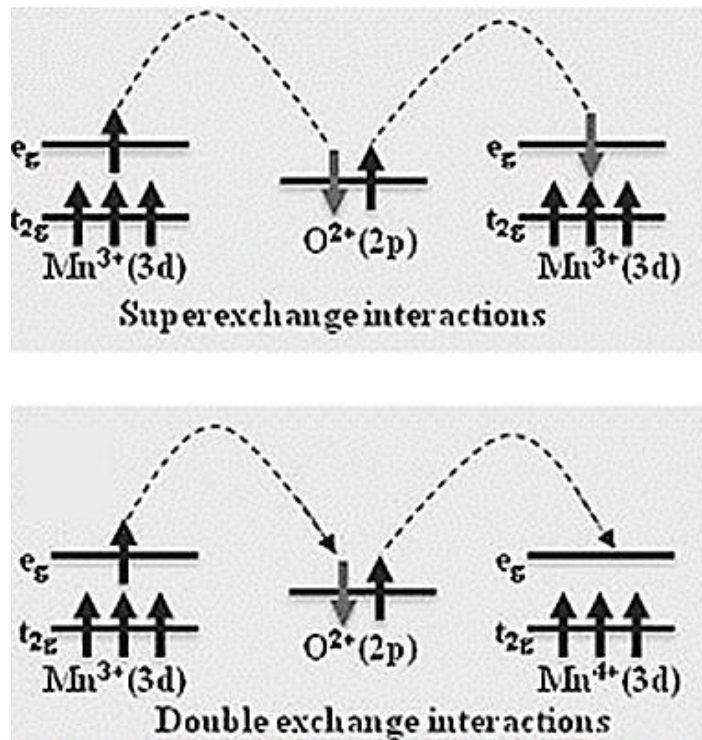


Figure 5.1. Schematic illustrations of superexchange and double exchange magnetic coupling in oxides (Figure from <sup>126</sup>)

There are a number of fundamental ideas of coupling in magnetic oxide materials that have been developed to address how indirect exchange interacts through nonmagnetic ions like oxygen. Classic models including super-exchange, double exchange and RKKY coupling are shown in Figure 5.1. The super-exchange model describes the normally short range exchange interaction can extend to a longer range.<sup>127</sup> Figure 5.1 (a) shows the example of the compound  $\text{LaMnO}_3$ . Here, oxygen bonding leads to an anti-parallel spin alignment of nearest neighboring Mn ions in  $\text{LaMnO}_3$ . Double exchange describes the magnetic coupling of A site doped  $\text{ABO}_3$  type perovskites (like Sr or Ca doped  $\text{LaMnO}_3$ ) which is called mixed valence compounds.<sup>128</sup> In these materials, as shown in Figure 5.1 (b), electrons on the Mn sites jumps back and forth across the oxygen and the electrons delocalized over the entire Mn-O-Mn. This model can explain magnetic structures with identical Mn ions and further ferromagnetic alignments. The RKKY coupling represents the case where magnetic ions are too far apart to interact with each other, and the local moment will

induce a spin polarization in surrounding conduction electron sea.<sup>97</sup>

Many ferro- and ferri-magnetic oxides are half-metallic, which essentially behaves like a conductor to electrons of particular spin direction while at the same time behaves like an insulator to electrons of opposite spin direction. They are therefore very interesting candidates for studying the magneto-transport phenomena. After the intense work on high temperature superconductor cuprates in the late 80's, where researchers learnt to grow high quality films, in the mid-1990s, the technology was adapted to mixed-valence perovskite manganese oxides, where similar high quality epitaxial films were grown. These manganese oxides have remarkable inter-related structural, magnetic and transport properties induced by the mixed valence of the Mn<sup>3+</sup> and Mn<sup>4+</sup> ions. Historically they led to new physical concepts such as double exchange and the Jahn-Teller effect.<sup>129</sup> The new phenomena of colossal magnetoresistance (CMR), and low field magnetoresistance (LFMR) were discovered where electrical resistivity changed with the application of magnetic field, as well as optically-induced magnetic phase transitions. The CMR effect is attributed to the ratio of the Mn<sup>3+</sup> and Mn<sup>4+</sup> ions in the perovskite and is sensitive to the partial doping of the trivalent rare-earth ion by divalent alkaline-earth cation. The doped perovskite manganites have strong correlations between the structure and electronic magnetic phases. Structurally, the electronic and magnetic properties are related to the tolerance factor which is basically the size ratio of the anion-oxygen bond to the cation-oxygen bond of the BO<sub>6</sub> octahedra in the perovskite structure. The tolerance factor can be defined as:

$$t = \frac{d_{A-O}}{\sqrt{2}d_{B-O}} = \frac{\langle r_A \rangle + r_o}{\sqrt{2}(\langle r_B \rangle + r_o)} \quad (5.1).$$

Equation 5.1 simply shows that the tolerance factor is the ratio of the size of A and B atomic size in ABO<sub>3</sub> perovskite. Tolerance factor value of  $t > 1.00$  simply means that the B cation is too small, which means it can be off-centered. Consequently, B-site off centering results in ferroelectricity (for example, in ferroelectric BaTiO<sub>3</sub>, Ti atoms is smaller than Ba atom, resulting in the off centering possibility of Ti atom which is located at the centre of the BO<sub>6</sub> octahedra). For  $t = 1.00$  (0.98-1.00), the cubic structure

is obtained, such as in the case of  $\text{CaTiO}_3$ . On the other hand, for  $t < 1.00$ , when the B cation is too large, rotation of octahedral can occur, which results in distortion from cubic to orthorhombic structure. In addition, the B-O-B bond angle is a direct function of tolerance factor. Lower  $t$  results in lower bond angle. In other words, the tolerance factor dictates the distortion in the  $\text{MnO}_6$  octahedra.

In manganites, one of the most studied lattice distortions is the deformation of the  $\text{MnO}_6$  octahedron called the Jahn-Teller effect. It describes the lifting of degeneracy due to the orbital-lattice interaction in the  $\text{MnO}_6$  octahedral which is the basic building blocks of the manganites. It tends to occur spontaneously as the lattice distortion grows. Therefore, it can be easily understood that chemical substitution can be used to tune the tolerance factor which in turn determine the magnetic and electronic properties. Besides cation and anion radii, structural distortion is also dependent on doping level, temperature and pressure.

Unlike conventional methods which uses either chemical substitution in perovskites or strain engineering using thin film, VAN offers a very interesting and novel way of tuning the magnetic and electronic properties in perovskite manganites because of the different nature of the strain states that can be induced in VAN films compared to planar epitaxial films. In this chapter, we will show that the complex antiferromagnetic insulator  $\text{Sm}_{0.34}\text{Sr}_{0.66}\text{MnO}_3$  whose properties are very hard to control in thin films because the properties are so sensitive to strain, can be turned into a ferromagnetic insulator (FMI) by using  $\text{Sm}_2\text{O}_3$  as strain controlling phase in VAN architecture. This ability to create a FMI has not be shown before in standard planar films. Before going into strain tuning of magnetic properties using the VAN structure, ferromagnetic insulators will be first introduced.

## 5.2. Ferromagnetic Insulators

Ferromagnetic insulators (FMIs) are of great research interest due to the rare combination of ferromagnetism and insulating characteristics which are needed for oxide spintronics and multiferroics.<sup>130-132</sup> FMIs can be used in spin-filter barriers in magnetic tunnel junctions (MTJs). They are also important parent compounds for creating multiferroics, in which the coexistence of ferromagnetism and ferroelectricity leads to magneto-dielectric coupling.<sup>133-136</sup>

There are few spin-filter materials with very high efficiency. EuS and EuSe are rare examples, but the low ferromagnetic  $T_C$  (16.6 K for EuS and 4.6 K for EuSe) of these materials limits their application to liquid helium temperatures.<sup>134, 137</sup> In order to realize higher temperature applications, EuO has been investigated (ferromagnetic  $T_C$  of 69 K). Nevertheless, the challenging growth conditions hinder its use.<sup>138</sup> Other promising candidates with high ferromagnetic  $T_C$  include ferrites, but these are not without their own problems. For instance, rare-earth nitrides suffer from stability problems due to their rapid oxidation in air<sup>139</sup> while ferrites, although having above room temperature ferromagnetic  $T_C$ , have complex spinel structures, making it difficult for their integration into tunnel hetero-structures made of half-metallic ferromagnetic perovskites such as  $\text{La}_{0.67}\text{Sr}_{0.33}\text{MnO}_3$ .<sup>140</sup> Consequently, new practical FMIs are strongly needed. Perovskites are excellent candidates as they are chemically and structurally compatible with numerous oxide electrodes.<sup>141</sup>

Transition metal oxide perovskites are interesting because of their wide variety of structural, magnetic and transport properties.<sup>142-143</sup> For example,  $\text{RE}_{1-x}\text{AE}_x\text{MnO}_3$  (RE and AE represent a trivalent rare earth and a divalent alkaline earth element, respectively) systems exhibit a very rich electronic and magnetic phase diagram due to strong coupling between the charge, orbital and spin degrees of freedom.<sup>144-145</sup> However, only very few insulating perovskite manganites are ferromagnetic. Notable exceptions are  $\text{BiMnO}_3$  and  $\text{La}_{0.1}\text{Bi}_{0.9}\text{MnO}_3$  with ferromagnetic  $T_C$  of around 100 K. However, the

growth of these materials is nontrivial.<sup>146-147</sup>

$\text{Sm}_{1-x}\text{Sr}_x\text{MnO}_3$  (SSMO), with  $x = 0.1$  to  $x = 0.3$ , is another potential perovskite FMI with a maximum ferromagnetic  $T_C$  of  $\sim 100$  K in bulk.<sup>148</sup> The phase diagram of SSMO is shown in Figure 5.2.

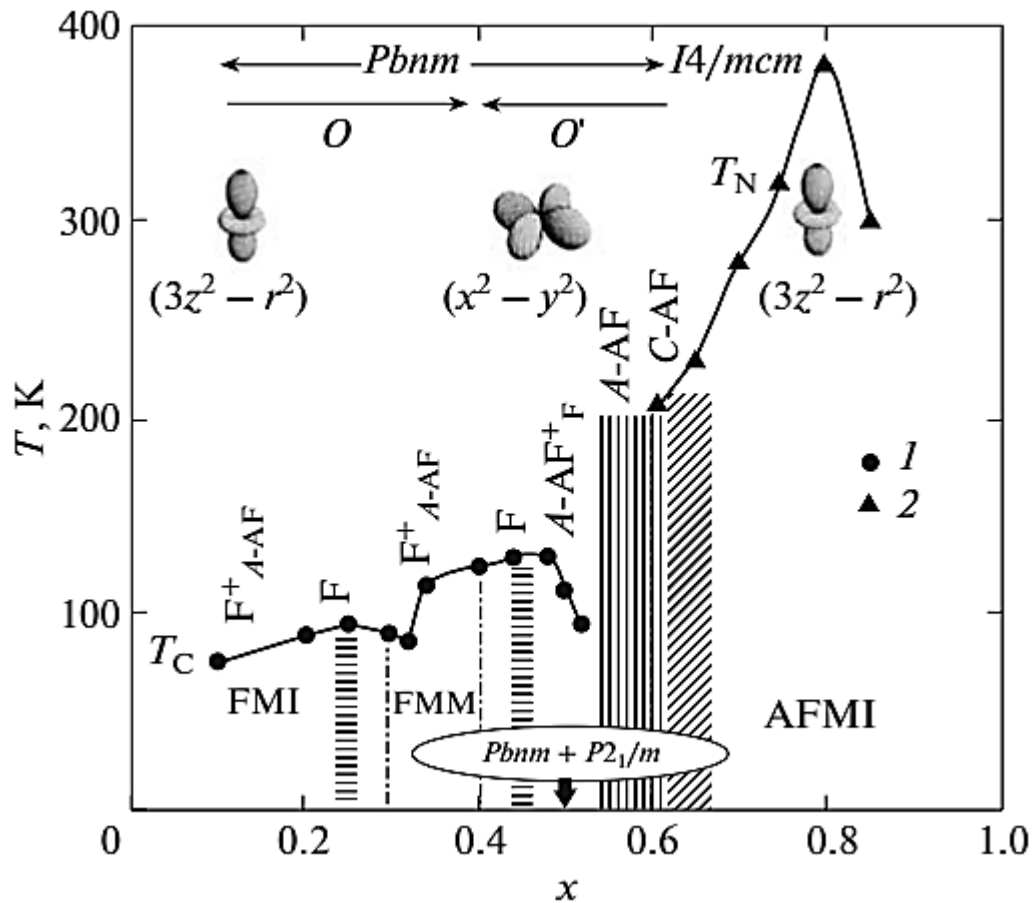


Figure 5.2. Magnetic and structural phase diagram of  $\text{Sm}_{1-x}\text{Sr}_x\text{MnO}_3$  system. (Figure from <sup>149</sup>)

In the figure, points 1 and 2 represent ferromagnetic  $T_C$  and antiferromagnetic  $T_N$  (Néel temperature – temperature above which antiferromagnetic becomes paramagnetic). FMI stands for ferromagnetic insulator; FMM for ferromagnetic metal and AFMI, for antiferromagnetic insulator. The vertical inscriptions correspond to the neutron diffraction data: F is ferromagnet; A-AF is A-type (*in-plane* spin ordering) antiferromagnet; C-AF is C-type (*out-of-plane* spin ordering) antiferromagnet; and

$F^+A$ -AF and  $A$ -AF $^+F$  are phase separated magnetic systems with a mixture of ferromagnetism and antiferromagnetism in which the FM and AFM phases dominate, respectively. The dashed areas correspond to homogeneous magnetic states: FM (horizontal hatching),  $A$ -AF (vertical hatching), and  $C$ -AF (diagonal hatching). Different types of crystal structure  $Pbnm$  ( $O$  and  $O'$ ) and  $I4/mcm$  (at all temperatures) and a mixture  $Pbnm + P2_1/m$  (only at low temperatures) are also indicated. The supposed types of orbital ordering in AFM phases ( $3z^2 - r^2$ ) and  $(x^2 - y^2)$  are shown schematically.

Recently, spin filter tunnel junctions based on SSMO were fabricated into devices,<sup>150</sup> giving 75% spin polarization. However, the junctions operated mainly at a low temperature of 5 K.<sup>151</sup> Thus despite the promising bulk properties, in strained films wide deviations in the ferromagnetic properties result.<sup>152-157</sup> Indeed, the physical properties of SSMO, of low band width, have great sensitivity to both strain and composition.<sup>158</sup> Even with minimization of substrate-induced strain using buffer layers and highly lattice matching substrates, properties are very different from the bulk values because of incomplete strain relaxation and also possibly because of oxygen vacancy strain-accommodating defects.<sup>159</sup> More recently, studies have focused on several perovskite systems where strain enhanced ferromagnetic  $T_C$ .<sup>160-163</sup> However, again strain relaxation with the film thickness leads to non-uniform properties through the film.<sup>164</sup>

As shown in Figure 5.2, the SSMO system is very sensitive to composition, which makes it interesting to explore the effect of strain on a particular composition of this material. Therefore, we believe that there is great possibility to use VAN films to create a stable ferromagnetic insulating phase which is not susceptible to substrate strain, which can be formed easily and which has uniform properties through the thickness. As shown in Chapter 4 above, in VAN films strain is controlled in the matrix by using a stiff strain-controlling second phase pillar in the film to control the out-of-plane strain.<sup>4</sup> As before with the BSTO and BTO film cases, strain-controlling pillars of

$\text{Sm}_2\text{O}_3$  are optimum to use since they are much stiffer than the SSMO matrix in which they could be grown ( $E_{\text{Sm}_2\text{O}_3} = 240 \text{ GPa}$  vs.  $E_{\text{SSMO}} = 130\text{--}160 \text{ GPa}$ , where  $E$  is the average elastic modulus).<sup>119, 165</sup>

Again, as we showed in Chapter 4, in VAN films in the less-stiff matrix the *out-of-plane* strain is controlled by vertical epitaxy, while the in-plane strain is determined by a combination of heteroepitaxy with the substrate as well by elastic interactions with the stiff nanopillars. Hence the relative mechanical properties (e.g. elastic moduli and thermal expansion coefficients) of the two materials in the composite film are important for controlling the in-plane strain.<sup>27</sup> Overall, a uniform and unconventional strain state can be induced in the matrix phase in thick ( $\sim\mu\text{m}$ ) nanocomposite films, something that is not possible in conventional thin films whose lattice parameters are dependent on planar epitaxy, with strain beginning to relax above just a few nm. In addition, for conventional films there is the problem of limited availability and high cost of single crystal substrates for precisely tuning lattice parameters in the films.

In our study, we wanted to explore whether strain has any effect on the magnetic properties of SSMO. Therefore, we started off with  $\text{SrMnO}_3$  and  $\text{Sm}_2\text{O}_3$  mixture to form the VAN structure. The composition ratio was chosen in such a way that it will enable SSMO with composition in the antiferromagnetic insulator region.

### 5.3. Growth of $\text{Sm}_{0.34}\text{Sr}_{0.66}\text{MnO}_3$ – $\text{Sm}_{1.64}\text{Sr}_{0.22}\text{Mn}_{0.14}\text{O}_3$ VAN Thin Films

Nanocomposite films of  $\text{Sm}_{0.34}\text{Sr}_{0.66}\text{MnO}_3$ – $\text{Sm}_{1.64}\text{Sr}_{0.22}\text{Mn}_{0.14}\text{O}_3$  were grown on the (001)  $\text{SrTiO}_3$  substrates using pulsed laser deposition (PLD). The starting target materials for PLD was prepared using a stoichiometric mixture of  $\text{Sm}_2\text{O}_3$  +  $\text{SrCO}_3$  +  $\text{MnO}_2$  powders followed by cold-pressing into 1 inch diameter pellet with 5 tons equivalent of force for 30 minutes. Subsequently, the pellet was sintered at 1100 °C for 6 hours. A Lambda Physik KrF excimer laser ( $\lambda = 248$  nm) was used for target ablation. The laser energy density was set at  $1 \text{ J cm}^{-2}$  with a target-to-substrate distance of 4.5 cm and 1 Hz pulse repetition rate. The vertical nanocomposite films were grown at 750 °C and 20 Pa oxygen pressure, followed by a short post deposition annealing at the same temperature for 30 minutes under a 100 mbar oxygen atmosphere. After growth, films were cooled down to room temperature at a cooling rate of  $10^\circ\text{C}/\text{min}$  in 1 mbar oxygen atmosphere to prevent excessive oxygen loss. The resulting thickness of the film is 120 nm.

*Panalytical X'Pert Pro* high resolution XRD with PreFIX module and Cu  $K\alpha$  source, with the wavelength 0.154 nm was used to characterize our films. The XRD work was done using  $2\theta$ - $\omega$  scan as well as reciprocal space mapping (RSM) to study various strain states in the film both in the in-plane and out-of-plane directions. To ensure consistency, the scanning step size was fixed at  $0.02^\circ$  while the scanning time per step was fixed at 1 second for all XRD scans on all samples. Morphology as well as cross-sectional images of the film were obtained by high resolution transmission electron microscopy (HRTEM) which was done by Prof. Haiyan Wang's lab in Texas A&M University in the U.S. EDS of TEM images were done by Dr. Quanxi Jia from Los Alamos National Laboratory, U.S.). Platinum contacts were deposited by sputtering to serve as the top contact for electrical measurement. Resistance vs temperature data was obtained using four point configuration in a closed-cycle He cryostat system with cooling and heating rate of  $1^\circ\text{C}/\text{min}$  and 20 mA current. Magnetic

properties were characterized using a superconducting quantum interference device (SQUID). Unless otherwise stated, all experiments were carried out in Device Materials Group Laboratory, Department of Materials Science and Metallurgy, University of Cambridge.

Figure 5.3 (top panel) shows a scanning transmission electron microscopy (STEM) image of a 120 nm thick VAN film with clear pillar phase ( $\text{Sm}_{1.64}\text{Sr}_{0.22}\text{Mn}_{0.14}\text{O}_3$ ) embedded in SSMO matrix phase ( $\text{Sm}_{0.34}\text{Sr}_{0.66}\text{MnO}_3$ ). The bottom left panel of Figure 5.3 shows a high angle annular dark field (HAADF) image, which reveals a darker SrO phase on the surface of the nanocomposite film. The presence of the surface SrO in our films is consistent with the previous studies showing Sr migration to film surfaces to give poorly crystalline precipitates.<sup>166</sup> The selected area electron diffraction (SAED) pattern in the bottom right panel of Figure 5.3 shows the highly crystalline nature of the STO substrate as well as both of the  $\text{Sm}_{1.64}\text{Sr}_{0.22}\text{Mn}_{0.14}\text{O}_3$  and SSMO phases in the film.

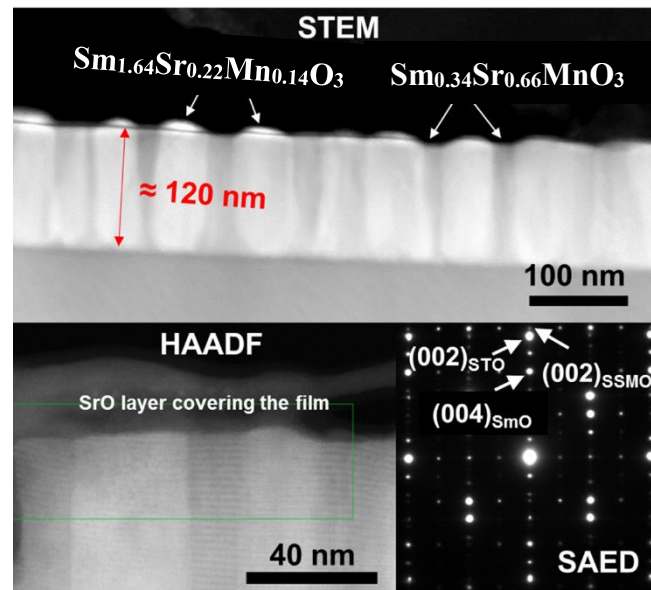


Figure 5.3 High resolution cross sectional TEM image of the nanocomposite film (top). High-angle annular dark field (HAADF) image (bottom left) as well as selected area electron diffraction (SAED) (bottom right). Figure from <sup>167</sup>.

A high resolution cross-sectional TEM image of a nanocomposite film shows a clean and sharp interface between the  $\text{Sm}_{1.64}\text{Sr}_{0.22}\text{Mn}_{0.14}\text{O}_3$  nano-pillars and the SSMO matrix (see Figure 5.4). Two different orientations of the  $\text{Sm}_{1.64}\text{Sr}_{0.22}\text{Mn}_{0.14}\text{O}_3$  nano-pillars were observed, (110) and (001) while only one orientation of SSMO was observed, (001). As shown in the schematic crystal in the lower part of Figure 5.4, the (110)  $\text{Sm}_{1.64}\text{Sr}_{0.22}\text{Mn}_{0.14}\text{O}_3$  phase was oriented with the STO substrate in-plane with the  $[110]$   $\text{Sm}_{1.64}\text{Sr}_{0.22}\text{Mn}_{0.14}\text{O}_3$   $\parallel$   $[100]$  STO. On the other hand, the (001)  $\text{Sm}_{1.64}\text{Sr}_{0.22}\text{Mn}_{0.14}\text{O}_3$  was oriented in-plane with the  $[100]$   $\text{Sm}_{1.64}\text{Sr}_{0.22}\text{Mn}_{0.14}\text{O}_3$   $\parallel$   $[100]$  STO. The SSMO phase was oriented in-plane with the  $[100]$  SSMO  $\parallel$   $[100]$  STO.

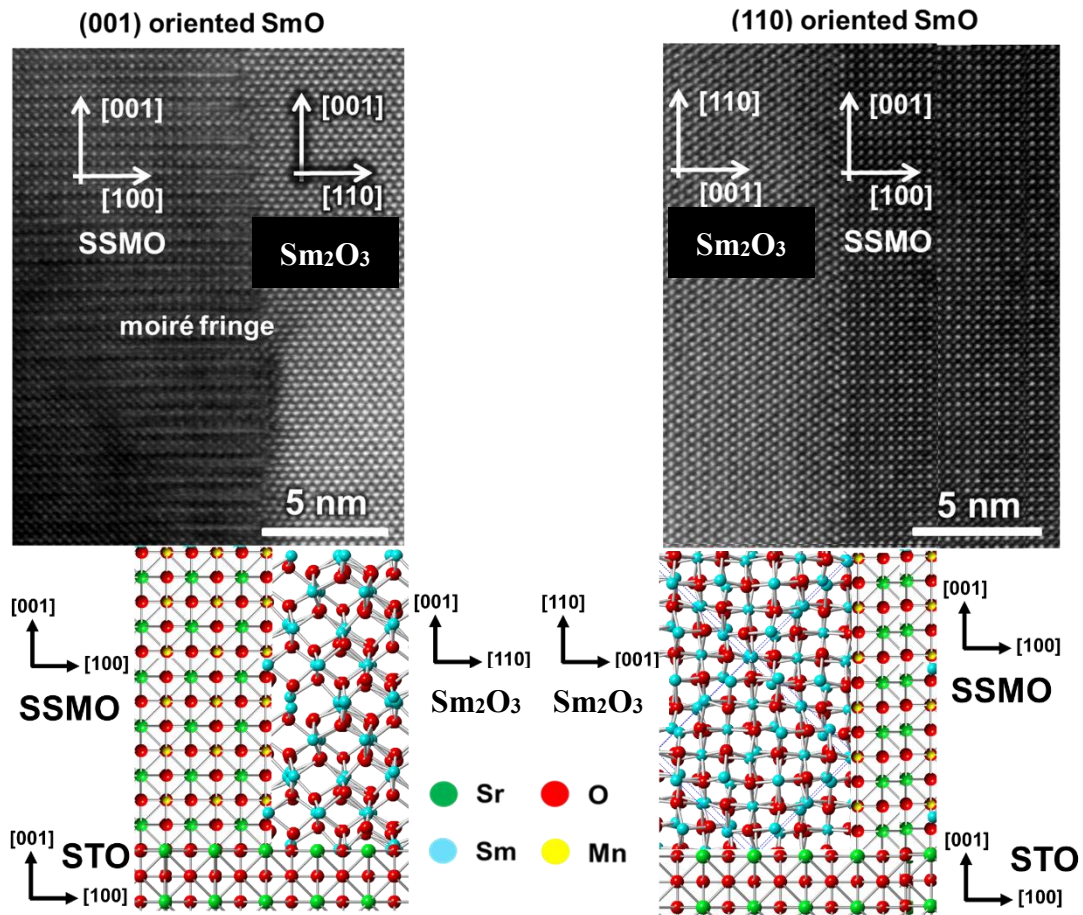


Figure 5.4. High resolution TEM image showing the interface between the nanopillar and matrix (top). Crystal orientation representation of the nanopillar and matrix as well as the substrate (bottom). (Figure from <sup>167</sup>)

The occurrence of the (110) orientation of  $\text{Sm}_{1.64}\text{Sr}_{0.22}\text{Mn}_{0.14}\text{O}_3$  in the nanocomposite film is different from the case of single phase  $\text{Sm}_{1.64}\text{Sr}_{0.22}\text{Mn}_{0.14}\text{O}_3$  films grown on the (001) STO which are typically (001) oriented.<sup>168</sup> The reason for this difference is that vertical epitaxial lattice matching between the [110]  $\text{Sm}_{1.64}\text{Sr}_{0.22}\text{Mn}_{0.14}\text{O}_3$  and the [001] SSMO (0.9% misfit) in the (110)  $\text{Sm}_{1.64}\text{Sr}_{0.22}\text{Mn}_{0.14}\text{O}_3$  films is much lower than the misfit between the [001]  $\text{Sm}_{1.64}\text{Sr}_{0.22}\text{Mn}_{0.14}\text{O}_3$  and the [001] SSMO (6.6% misfit) in the (001)  $\text{Sm}_{1.64}\text{Sr}_{0.22}\text{Mn}_{0.14}\text{O}_3$  films. Figure 5.5 shows compositional characterization of the nanocomposite films by EDS, by atomic-scale EDS, by using atomic concentration maps, and by using atomic concentration line profiles. In the EDS maps, very sharp and clean interfaces can be observed from the bright regions for both Sr and Mn in the same area, with the bright region for Sm being in the adjacent area. The atomic scale EDS maps show direct evidence of Sm substitution onto the Sr site. The atomic concentration maps and line profiles show the distinct nano-pillars of the composition  $\text{Sm}_{1.64}\text{Sr}_{0.22}\text{Mn}_{0.14}\text{O}_3$  and the matrix of the composition  $\text{Sm}_{0.34}\text{Sr}_{0.66}\text{MnO}_3$ . Hence, there is 11% of Sr and 7% of Mn substitution onto otherwise  $\text{Sm}_2\text{O}_3$  phase, resulting in  $\text{Sm}_{1.64}\text{Sr}_{0.22}\text{Mn}_{0.14}\text{O}_3$ . Similarly, there is 34% of Sm substitution onto the Sr site in otherwise  $\text{SrMnO}_3$  phase, resulting in  $\text{Sm}_{0.34}\text{Sr}_{0.66}\text{MnO}_3$ .

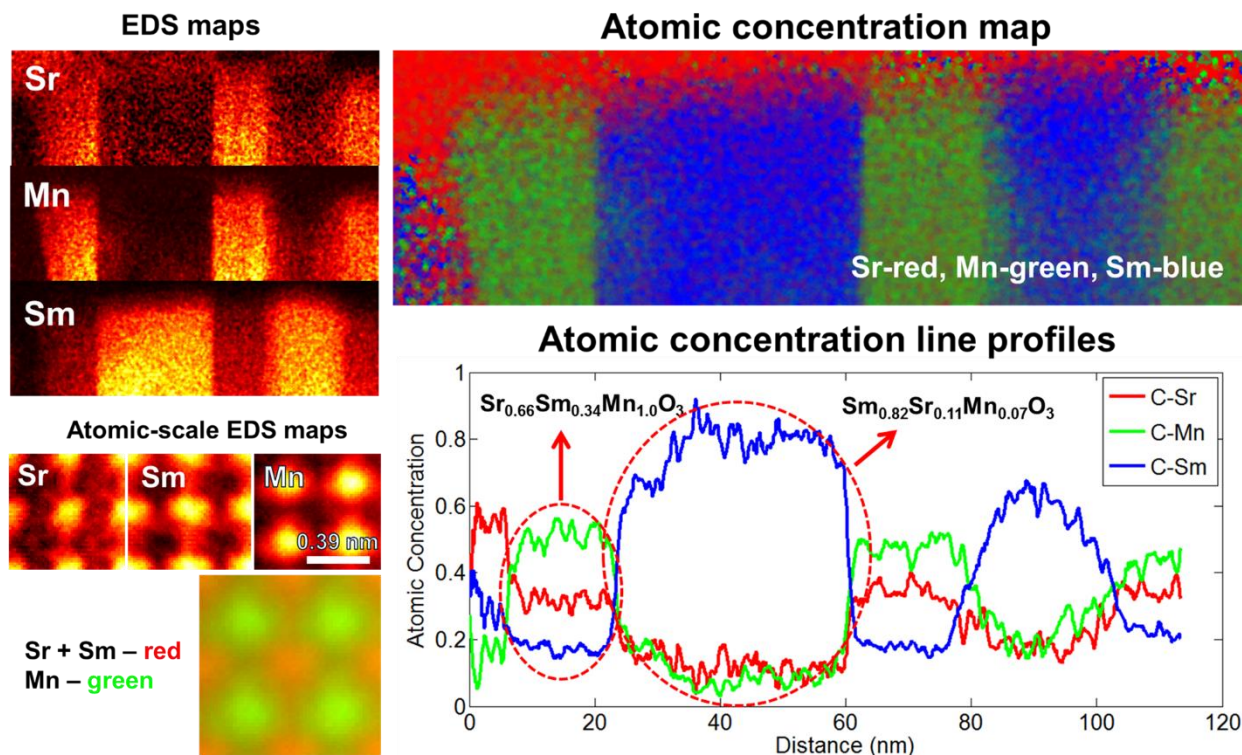


Figure 5.5. EDS map showing the compositions of the nanopillars and matrix (top left). Atomic-scale EDS maps (bottom left) showing Sr and Sm occupying the same sites in the perovskite lattice and the atomic concentration line profile (right image) showing the lateral compositions of the nanopillars and matrix. (Figure from <sup>167</sup>)

$2\theta$ - $\omega$  XRD scans of the nanocomposite films are shown in Figure 5.6. Sharp peaks of the SSMO (002) and  $\text{Sm}_{1.64}\text{Sr}_{0.22}\text{Mn}_{0.14}\text{O}_3$  (006) are observed in the Bragg–Brentano scan in Figure 5.6 (a) with some overlapping of the SSMO (002) and STO (002) peaks. No peaks associated with the (110)  $\text{Sm}_{1.64}\text{Sr}_{0.22}\text{Mn}_{0.14}\text{O}_3$  were observed due to the overlapping of the  $\text{Sm}_{1.64}\text{Sr}_{0.22}\text{Mn}_{0.14}\text{O}_3$  (440) with the STO (002) substrate peak. Owing to the poor crystallinity of the SrO phase on top of the nanocomposite film, even though it was observed in the high angle annular dark field (HAADF) image in Figure 5.3, it was also not observable by XRD in Figure 5.6. For comparison, Figure 5.6 (c) shows a  $2\theta$ - $\omega$  scan for a single phase SSMO film of the same thickness ( $\sim 100$  nm). In the  $2\theta$ - $\omega$  scan the (002) SSMO peak is at a higher  $2\theta$  value of  $48.4^\circ$  compared to  $47.6^\circ$  for the nanocomposite, indicating that the nanocomposite film has a higher  $c$  parameter than the single phase film.

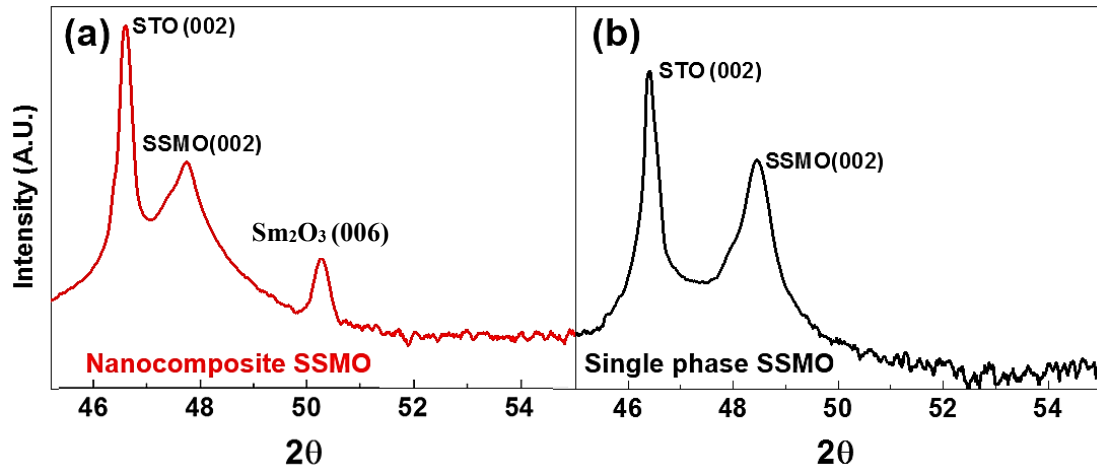


Figure 5.6 (a)  $2\theta$ - $\omega$  XRD scan of a nanocomposite film showing the presence of  $\text{Sm}_{1.64}\text{Sr}_{0.22}\text{Mn}_{0.14}\text{O}_3$  and SSMO phases and the STO substrate, all with the (001) orientation. (b)  $2\theta$ - $\omega$  XRD scan of a single phase SSMO film showing the presence of the SSMO film and the STO substrate, both with the (001) orientation. (Figure from <sup>167</sup>)

X-ray phi-scans of the STO substrate and the SSMO and  $\text{Sm}_{1.64}\text{Sr}_{0.22}\text{Mn}_{0.14}\text{O}_3$  peaks in the nanocomposite (Figure 5.7) show a cube-on-cube orientation of the SSMO on STO while the  $\text{Sm}_{1.64}\text{Sr}_{0.22}\text{Mn}_{0.14}\text{O}_3$  shows a  $45^\circ$  in-plane rotation with respect to the STO substrate, consistent with the high resolution TEM images. The phi-scan was done on (110) peaks for all phases.

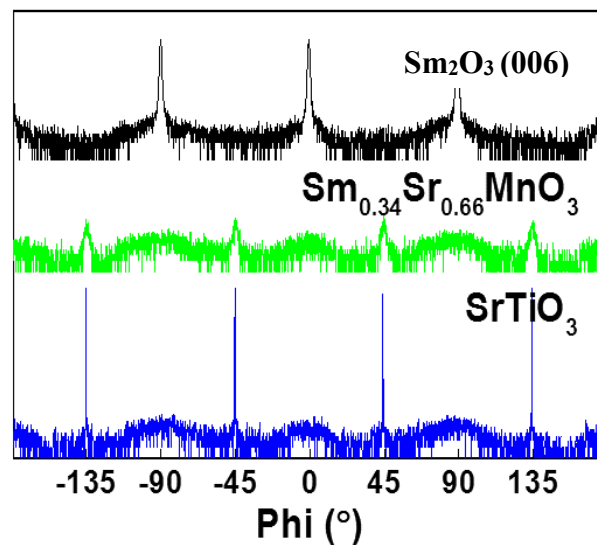


Figure 5.7. Phi-scan revealing the different *in-plane* orientations of  $\text{Sm}_{1.64}\text{Sr}_{0.22}\text{Mn}_{0.14}\text{O}_3$  and SSMO with respect to the STO substrate. (Figure from <sup>167</sup>)

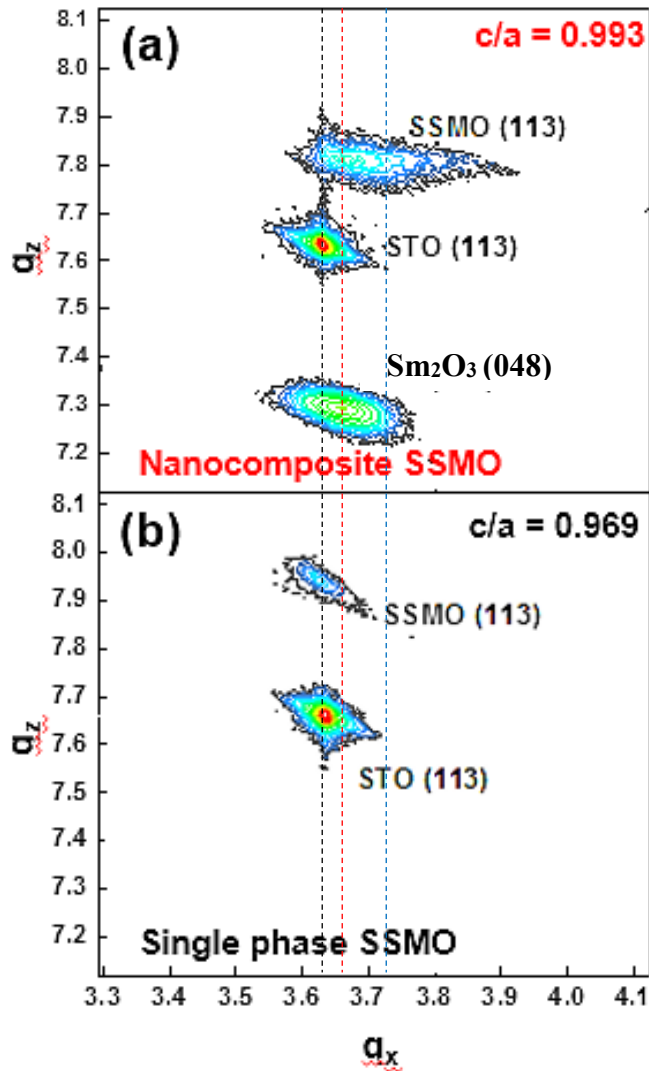


Figure 5.8. (a) RSM of the nanocomposite film with black and red vertical dashed lines indicating the center of the STO peak and SSMO peak in nanocomposite SSMO along  $q_x$ . Blue vertical dashed line indicates the bulk *in-plane* lattice parameter position of SSMO as a reference for comparison. (b) RSM of the single phase SSMO film showing close alignment along  $q_x$  of the SSMO (113) peak with the STO (113) peak as a result of epitaxial growth which causes the SSMO in-plane lattice parameter to be equivalent to the STO in-plane lattice parameter. (Figure from <sup>167</sup>)

Figure 5.8 (a) shows a reciprocal space map (RSM) of the nanocomposite film revealing the strain states of the phases in the nanocomposite film. In the figure,  $q_x$  of the SSMO (113) peak in nanocomposite is shifted to the left compared to bulk SSMO (e.g. red dashed line vs blue dashed line), indicating a higher a-axis in the

nanocomposite film compared to the bulk. Figure 5.8 (b) shows a reciprocal space map (RSM) of a single phase film. The SSMO (113) peak along  $q_x$  is displaced further from the bulk SSMO position (black dashed line vs red dashed line) and hence the a-axis is larger than the ones in the nanocomposite film as well as bulk. The different strain states obtained in the nanocomposite and single phase SSMO films are analyzed and discussed below.

Properties	$\text{Sm}_{0.34}\text{Sr}_{0.66}\text{MnO}_3$ in nanocomposite film	Single phase $\text{Sm}_{0.34}\text{Sr}_{0.66}\text{MnO}_3$ film	Bulk $\text{Sm}_{0.37}\text{Sr}_{0.63}\text{MnO}_3$ <sup>169</sup> (pseudo-cubic)
Thickness	120 nm	100 nm	N.A.
a (Å)	$3.846 \pm 0.016$	$3.876 \pm 0.009$	3.785
c (Å)	$3.819 \pm 0.008$	$3.756 \pm 0.005$	3.899
In-plane strain (%)	$1.61 \pm 0.42^a$	$2.40 \pm 0.24^a$	N.A.
Out-of-plane strain (%)	$-2.05 \pm 0.21^a$	$-3.67 \pm 0.13^a$	N.A.
Tetragonality (c/a)	<b><math>0.993 \pm 0.024</math></b>	<b><math>0.969 \pm 0.014</math></b>	<b>1.030</b>
Magnetic properties	Ferromagnetic	Antiferromagnetic	Antiferromagnetic
$T_C/T_N$ (K)	$T_C = 140$	$T_N = 100$	$T_N = 250$
Electrical properties	Insulating	Insulating	Insulating

Table 5.1. Properties of nanocomposite films compared to single phase films and bulk. (Table from <sup>167</sup>)

<sup>a</sup>Strain calculated relative to *bulk*  $\text{Sm}_{0.37}\text{Sr}_{0.63}\text{MnO}_3$

The in-plane lattice parameters of the  $\text{Sm}_{0.34}\text{Sr}_{0.66}\text{MnO}_3$  phase in both the nanocomposite film and single phase SSMO films were estimated by first determining the out-of-plane parameter from the  $2\theta-\omega$  scans, and then by using this value to extract the in-plane lattice parameter obtained from the RSM (113) peak. It is important to note that the single phase SSMO film was prepared as a comparison only after the exact

composition for the nanocomposite film was determined. For growing single phase SSMO,  $\text{Sm}_{0.34}\text{Sr}_{0.66}\text{MnO}_3$  target was made from a stoichiometric mixture of  $\text{Sm}_2\text{O}_3 + \text{SrCO}_3 + \text{MnO}_2$  powders followed by cold-pressing into 1 inch diameter pellet with 5 tons equivalent of force for 30 minutes. Subsequently, the pellet was sintered at 1100 °C for 6 hours. As shown in Table 5.1, the in-plane and out-of-plane lattice parameters in the nanocomposite film are  $a$ :  $3.846 \pm 0.016 \text{ \AA}$  and  $c$ :  $3.819 \pm 0.008 \text{ \AA}$ , respectively. These values are  $1.61 \pm 0.42\%$  in tension in-plane and  $-2.05 \pm 0.21\%$  in compression out-of-plane relative to bulk  $\text{Sm}_{0.37}\text{Sr}_{0.63}\text{MnO}_3$ , giving a  $c/a$  of  $0.993 \pm 0.024$ . In contrast, the in-plane and out-of-plane lattice parameters for the single phase SSMO film from  $2\theta$ - $\omega$  scans are  $a$ :  $3.876 \pm 0.009 \text{ \AA}$  and  $c$ :  $3.756 \pm 0.005 \text{ \AA}$ , respectively. These values are  $2.40 \pm 0.24\%$  in tension in-plane and  $-3.67 \pm 0.13\%$  in compression out-of-plane relative to bulk  $\text{Sm}_{0.37}\text{Sr}_{0.63}\text{MnO}_3$ , giving a  $c/a$  of  $0.969 \pm 0.014$ . The higher level of strain and overall low  $c/a$  in the single phase film arise because of the in-plane epitaxial straining from the STO substrate ( $a = 3.905 \text{ \AA}$ ). The magnetic and lattice parameter data for bulk SSMO was taken at  $\text{Sm}_{0.37}\text{Sr}_{0.63}\text{MnO}_3$  because it is the closest available data to the actual composition of the nanocomposite phase.

The partial relaxation of the in-plane lattice parameter to  $3.876 \text{ \AA}$  is expected owing to the relatively thick film. The out-of-plane compression arises through elastic strain to conserve the cell volume. On the other hand, in the nanocomposite film the out-of-plane compression arises from vertical epitaxy with the stiff  $\text{Sm}_{1.64}\text{Sr}_{0.22}\text{Mn}_{0.14}\text{O}_3$  nano-pillars. Here, for the (001)  $\text{Sm}_{1.64}\text{Sr}_{0.22}\text{Mn}_{0.14}\text{O}_3$  orientation 3 unit cells of SSMO match with 1 unit cell of  $\text{Sm}_{1.64}\text{Sr}_{0.22}\text{Mn}_{0.14}\text{O}_3$  ( $3 \times 3.819 \text{ \AA} \parallel 1 \times 10.93 \text{ \AA}$ ), and for the (110)  $\text{Sm}_{1.64}\text{Sr}_{0.22}\text{Mn}_{0.14}\text{O}_3$  orientation, 4 unit cells of SSMO match with 1 unit cell of  $\text{Sm}_{1.64}\text{Sr}_{0.22}\text{Mn}_{0.14}\text{O}_3$  ( $4 \times 3.819 \text{ \AA} \parallel 1 \times 10.93 \times \sqrt{2} \text{ \AA}$ ). The in-plane tension arises because upon cooling the film from the growth temperature, the stiff  $\text{Sm}_{1.64}\text{Sr}_{0.22}\text{Mn}_{0.14}\text{O}_3$  pillars with a lower coefficient of thermal expansion cause the vertically epitaxially coupled  $\text{Sm}_{0.34}\text{Sr}_{0.66}\text{MnO}_3$  to expand.<sup>27</sup> The tension is less in the composite film compared to the single phase SSMO films because of the different mechanism of the strain control.

## 5.4. Magnetic and Electrical Properties of $\text{Sm}_{0.34}\text{Sr}_{0.66}\text{MnO}_3\text{--Sm}_{1.64}\text{Sr}_{0.22}\text{Mn}_{0.14}\text{O}_3$ VAN Thin Films

Resistance vs. temperature plots comparing a nanocomposite film to a single phase SSMO film are shown in Figure 5.9. An insulating profile was observed throughout the measurement temperature range. Below 50 K, the resistance of both films is beyond the measurement limit. The electrical conduction mechanism at high temperatures follows the small polaron hopping (SPH) model.<sup>170-171</sup> The resistance as a function of temperature is given by:

$$R(T) = ATe^{\frac{E_A}{k_B T}} \quad (5.2),$$

where  $E_A$  is the activation energy for conduction,  $T$  is the temperature and  $A$  is a constant. The activation energy  $E_A$  is determined by using linear fitting of the  $\ln(R/T)$  vs.  $1/T$  (dotted line in Figure 5.9), giving 94 meV for the nanocomposite film and 84 meV for the single phase SSMO film. Both these values are higher than the bulk SSMO value of 45–46 meV.<sup>172</sup> This is consistent with reduction of the electrical conduction because of strain in the films (and in the nanocomposite case, defects along the vertical interfaces between the two phases).

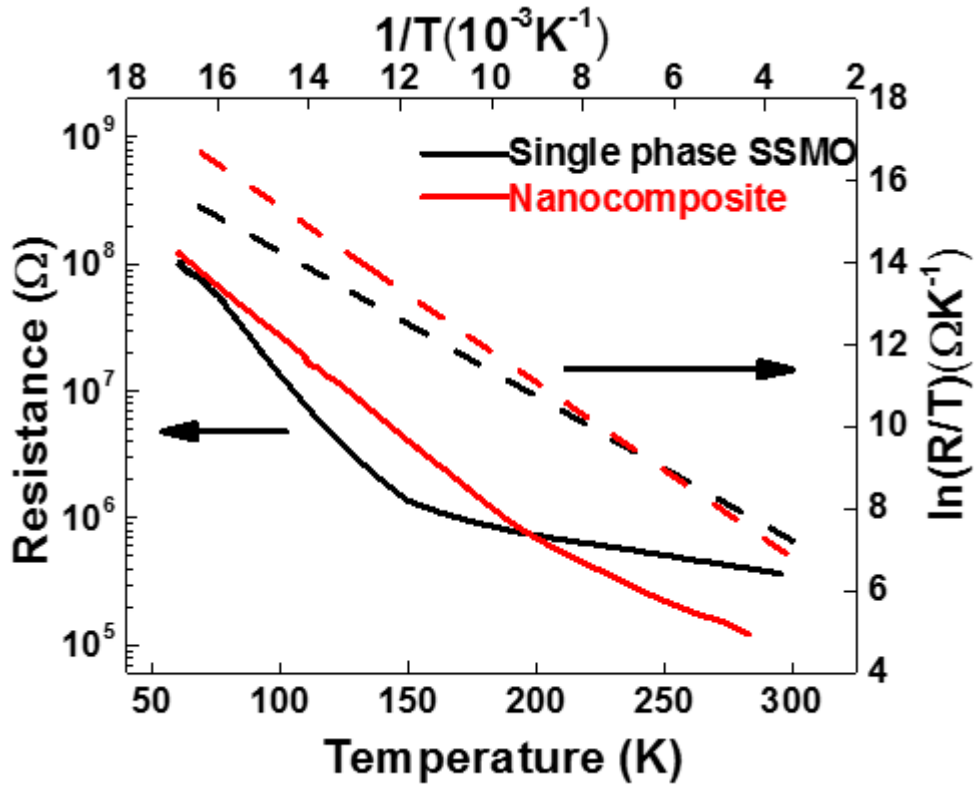


Figure 5.9 Resistance vs. temperature plot comparing the nanocomposite to a single phase film. The dotted lines in the plot shows linear fitting of  $1/T$  vs.  $\ln(R/T)$ . (Figure from <sup>167</sup>)

The comparative magnetic properties of the nanocomposite and single phase SSMO films are shown in Figure 5.10.  $M$  vs.  $T$  plots show ferromagnetism with a  $T_C$  of 140 K for the nanocomposite film. We note that in the literature the highest  $T_C$  value in the ferromagnetic insulating (FMI) Sr-doped  $\text{SmMnO}_3$  system is 100 K which is for the optimally doped (25% Sr doped) composition.<sup>150</sup> Therefore the  $T_C$  of the SSMO phase formed in our nanocomposite films is 40 K higher than for any FMI Sr-doped  $\text{SmMnO}_3$  phase. In addition, the  $T_C$  of our nanocomposite films is 10 K higher than for the ferromagnetic metal (FMM), Sr-doped  $\text{SmMnO}_3$  (48% Sr).<sup>173</sup>

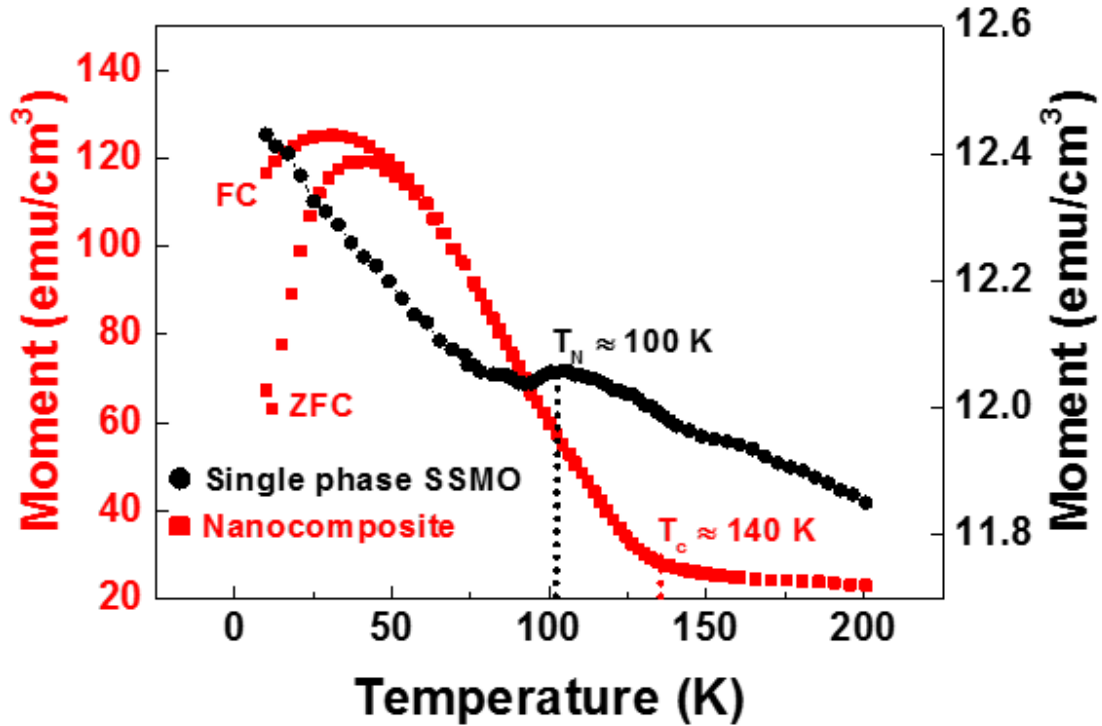


Figure 5.10. Magnetization vs. temperature plot comparing the nanocomposite to a single-phase film. (Figure from <sup>167</sup>)

A cluster-glass like behavior with a strong bifurcation between the field-cooled (FC) and zero field-cooled (ZFC) at 50 K was observed and the proposed origin of this is discussed later.<sup>174</sup> Figure 5.11 shows the magnetic hysteresis loop of  $M$  vs.  $H$  at 10 K for the nanocomposite film. After subtracting the paramagnetic background from the substrate and  $\text{Sm}_{1.64}\text{Sr}_{0.22}\text{Mn}_{0.14}\text{O}_3$ , a clear ferromagnetic hysteresis loop is obtained. The coercivity ( $H_C$ ) and saturation magnetic moment ( $M_S$ ) are 100 Oe and  $146\text{ emu cm}^{-3}$  ( $1.93\mu\text{B/Mn}$ ), respectively. This is comparable to the optimum 25% Sr doped  $\text{SmMnO}_3$  phase, as mentioned above.<sup>151</sup>

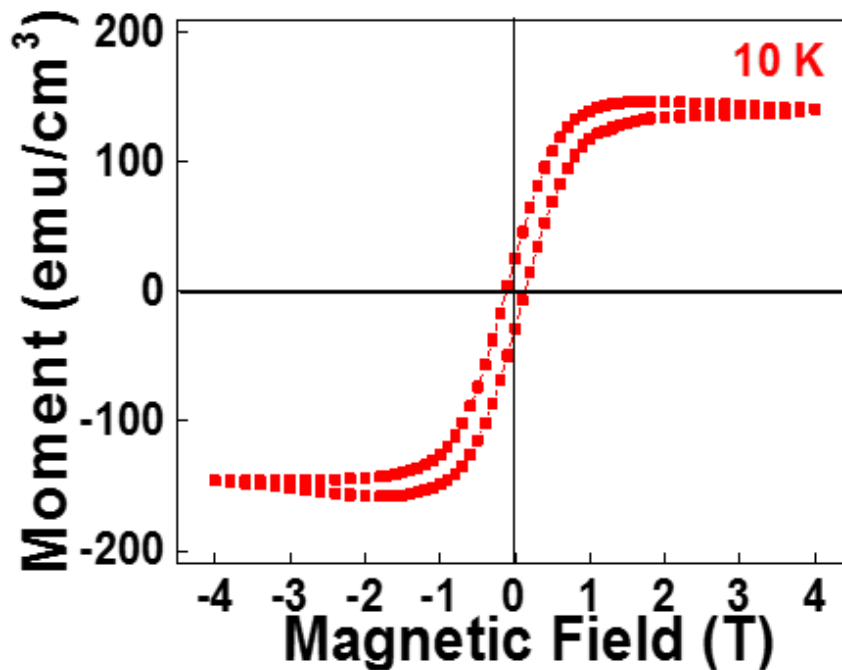


Figure 5.11 shows the magnetic hysteresis loop of the nanocomposite film. (Figure from <sup>167</sup>)

For the single phase SSMO films, AFM behavior was observed with a  $T_N$  of 100 K (Figure 5.10).<sup>148</sup> This is comparable to bulk  $\text{Sm}_{0.34}\text{Sr}_{0.66}\text{MnO}_3$  which shows C-type antiferromagnet behavior, although the  $T_N$  is higher for the bulk at  $\sim 250$  K, consistent with the very different levels of tetragonal distortion ( $c/a = 0.969$  for the single phase films vs. 1.030 for the bulk, as shown in Table 5.1).

We now turn to gain an understanding of the magnetic properties of the plain versus nanocomposite films obtained in this study. In doped manganites, magnetic interactions between the Mn atoms are determined by competition between FM double exchange interactions and AFM super-exchange.<sup>175</sup> The origin of the magnetic properties in the nanocomposite films can be understood by first realizing that the level of structural distortion strongly influences these interactions. With Jahn–Teller effects at play, small distortions of  $\text{MnO}_6$  can stabilize either of the  $e_g$  orbitals,  $3z^2 - r^2$  or  $x^2 -$

$y^2$ . For  $c/a > 1$  ( $c/a < 1$ ), the  $\text{MnO}_6$  octahedra are tensile strained (compressed) and consequently the  $3z^2 - r^2$  ( $x^2 - y^2$ ) orbitals are energetically favored over the  $x^2 - y^2$  ( $3z^2 - r^2$ ) orbitals.

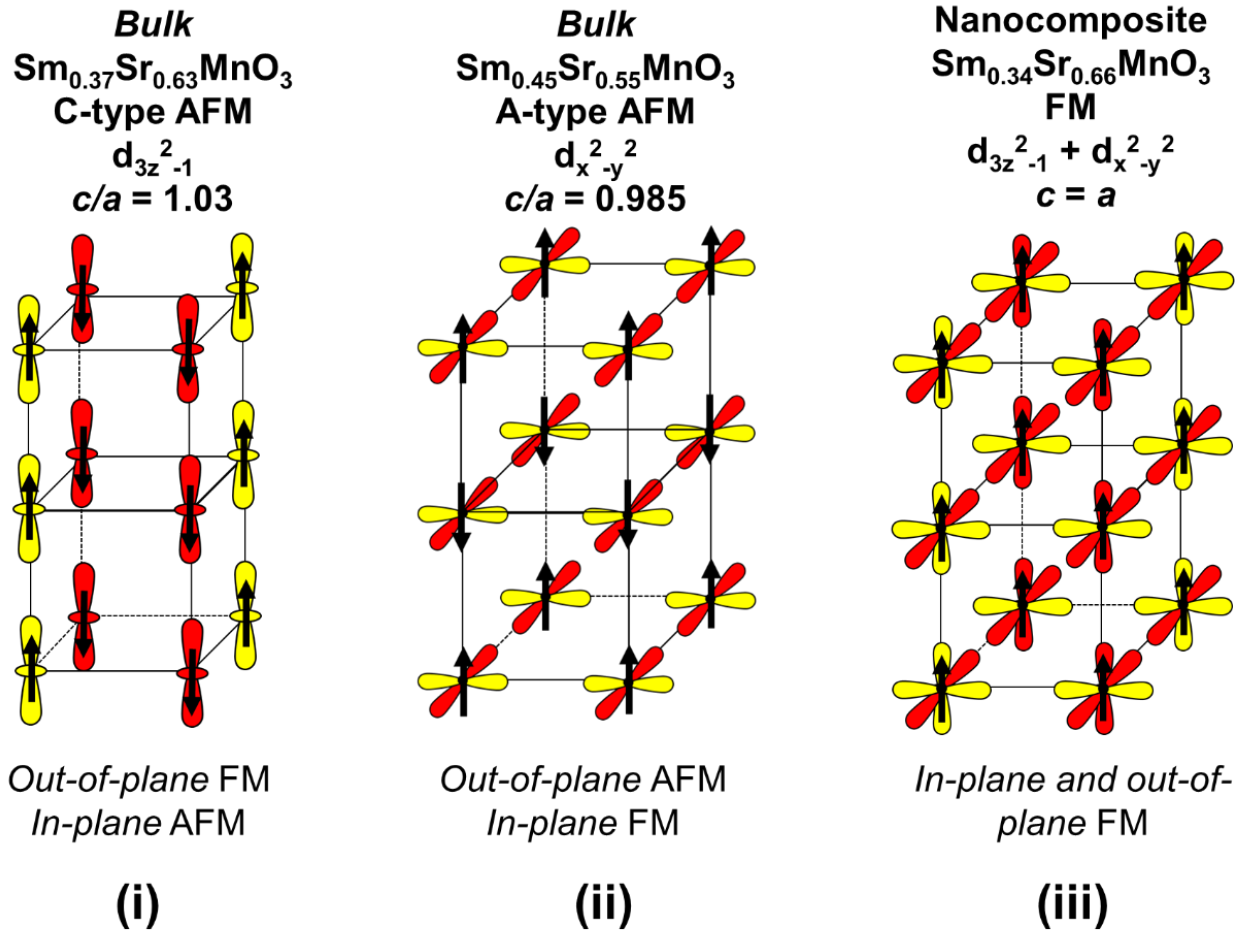


Figure 5.12. Schematic diagram showing C-type (out of plane coupling) and A-type AFM orbitals (in plane coupling) as well as FM orbitals. (both in plane and out of plane coupling). (Magnetic properties measurement were done with the help of Dr. Eun-Mi Choi). (Figure from <sup>167</sup>)

Hence, for  $c/a > 1$  the  $3z^2 - r^2$  orbitals have a higher occupancy. This results in 1-D FM double exchange interactions along the out-of-plane direction. The 1-D FM columns are AFM owing to super-exchange coupling. This results in a C-type AFM structure (as shown in Figure 5.12 (i)). This is the case for bulk  $\text{Sm}_{0.37}\text{Sr}_{0.63}\text{MnO}_3$ ,  $c/a = 1.03$  (Table 5.1).

For  $c/a < 1$ , the  $x^2 - y^2$  orbitals have a higher occupancy. This leads to strong double exchange coupling in the  $\text{MnO}_2$  planes which strengthens the ferromagnetic ordering in-plane. At the same time, super-exchange coupling stabilizes the antiferromagnetic ordering in the out-of-plane direction. This results in an A-type AFM as shown in Figure 5.12 (ii). This is the case for the single phase  $\text{Sm}_{0.34}\text{Sr}_{0.66}\text{MnO}_3$  films,  $c/a = 0.969$  (Table 5.1).

In our  $\text{Sm}_{0.34}\text{Sr}_{0.66}\text{MnO}_3$  nanocomposite films,  $c/a = 0.993 \pm 0.024$  (Table 5.1). Hence, the tetragonal distortion is reversed compared to the bulk value. Because  $c$  is close to  $a$  there is more or less equal occupation of the  $x^2 - y^2$  and  $3z^2 - r^2$  orbitals which produces double exchange interactions in both the in-plane and out-of-plane directions, thus leading to ferromagnetic ordering in 3-dimensions (as shown in Figure 5.12 (iii)).

Besides the extent of tetragonal distortion in the films, we should consider the actual Mn–O–Mn bond lengths. This is because AFM super-exchange interactions depend on Mn–O distances more strongly than the FM double exchange interactions. Hence, longer Mn–O bond lengths make the AFM super-exchange coupling weaker, whereas they influence the FM double exchange much less.<sup>176</sup> Hence, in our films FM double exchange dominates over AFM super-exchange, leading to the observed FM behavior. Overall, however, the AFM interactions in the film compete with the FM interactions. This competition explains the cluster glass-like behaviour in the  $M$  vs.  $T$  plot below 50 K in Figure 5.10.

The creation of high  $T_C$  ferromagnetism in our nanocomposite films is achieved via strain coupling between two phases. The work parallels artificial super-lattice (SL) studies where magnetic phases are coupled to other phases in a parallel configuration. In the SL studies, large increase of ferromagnetic  $T_C$  have been found when the in-plane strain is controlled by lateral coupling of phases. A ferromagnetic  $T_C$  of 650 K

(increased by nearly 300 K compared to bulk and plain films) has been observed for LSMO–BTO (with in-plane straining of the LSMO by 1%).<sup>177</sup> A key difference between the SL films and the nanocomposite films is that the nanocomposite films self-assemble rather than being made by a complex layering process.

In summary, nanocomposite films containing  $\text{Sm}_{0.34}\text{Sr}_{0.66}\text{MnO}_3$  were grown on  $\text{SrTiO}_3$  (001) with 120 nm thickness. Stiff  $\text{Sm}_{1.64}\text{Sr}_{0.22}\text{Mn}_{0.14}\text{O}_3$  nanopillars formed in the matrix of  $\text{Sm}_{0.34}\text{Sr}_{0.66}\text{MnO}_3$ , gave a unique strain state of lower in-plane tensile and out-of-plane compression than can otherwise be realized in single phase films. This leads to a lower  $c/a$  value compared to both the single phase films and bulk. This  $c/a$  reduction leads to 140 K ferromagnetism and insulating behavior. This work demonstrates a novel strain approach for tuning magnetic properties in thin films.

# Chapter 6 Exploration of VAN Structure Formation and Properties Using Sputter Deposition

As introduced in Chapter 2, the main advantage of sputter deposition compared to PLD lies in its scalability and lower cost. With that in mind, we sought to explore the feasibility and develop more understanding in the growth process using sputter deposition to achieve VAN structure. In the first section of this chapter, BaTiO<sub>3</sub>–Sm<sub>2</sub>O<sub>3</sub> sputter growth is discussed in detail from sample preparation to growth parameters and their effects on film structure and properties. The second section will present growth of other materials combinations such as BaTiO<sub>3</sub>–Cu<sub>2</sub>O and Cu<sub>2</sub>O–ZnO. The last section of this chapter will present the potential, limitations and challenges in VAN growth by sputtering process.

## 6.1. Sputter Growth of BaTiO<sub>3</sub>–Sm<sub>2</sub>O<sub>3</sub>

BaTiO<sub>3</sub>–Sm<sub>2</sub>O<sub>3</sub> was chosen as the starting material for this study due to well reported success in PLD-grown BaTiO<sub>3</sub>–Sm<sub>2</sub>O<sub>3</sub> VAN structure to enable direct comparison.<sup>30</sup> A 2-inch diameter (BaTiO<sub>3</sub>)<sub>0.5</sub>–(Sm<sub>2</sub>O<sub>3</sub>)<sub>0.5</sub> composite sputter target with 99.99% purity was obtained from Able Target Limited. The films were grown on (001) SrTiO<sub>3</sub> single crystal substrates with RF magnetron sputter gun in UNIVEX 450B system. The sputter deposition was conducted in Sensors and Transducer cleanroom in Institute of Materials Research and Engineering (IMRE), Singapore. Sputter power ranging from 50 W to 200 W was used. Background pressure consists of mixture of Argon and Oxygen gas ranging from the lowest pressure limit (0.5 Pa) to the highest pressure limit (8.0 Pa) of the sputter system was applied. Substrate temperature was varied from 500 °C to 800 °C. In addition, the effect of different ratio of argon and oxygen mixture was also studied. Lastly, it is important to acknowledge that some arguments or possible explanations to the observed experimental results are speculative

in nature. Detailed investigation may be needed to accurately elucidate all the observed trend during the optimization process, which is beyond the current scope of exploratory work.

### 6.1.1 Effect of Substrate Temperature

Figure 6.1 shows the  $2\theta$ - $\omega$  XRD scan of the nanocomposite film grown on STO (001) with substrate temperature 500 °C to 800 °C with 100 °C increment, with all other parameters kept constant. In all depositions, the argon/oxygen ratio was kept at 3:1, with 6.0 Pa chamber pressure as well as 150 W sputter power. It is worth noting that due to the lack of quick and accurate method to determine film thickness (e.g. no step coverage was possible due to the limited substrate size, which makes determining thickness with profilometer not possible), the film thickness for most films was not known. However, to ensure comparability between different films, during optimization of growth conditions, the deposition time was adjusted commensurately with respect to theoretical growth rate. (e.g. film grown at 75 W power was deposited for twice the amount of time compared to film grown at 150 W power). TEM image from figure 6.7 provides a rare thickness data (~200 nm) for one of the films which may be used to represent the thicknesses for most films in this study, although significant variation in thickness may occur due to complex interdependency between all deposition parameters which may results in inaccurate anticipation of deposition time.

As mentioned in earlier chapters, high temperature energetically favor layer by layer growth. Thus it is highly expected that higher temperature will lead to better crystallinity of the film. For all data presented in this work, the argon/oxygen ratio was kept at 3:1, with 6.0 Pa chamber pressure as well as 150 W sputter power. As seen in Figure 6.1, the film grown at 500 °C shows very weak  $\text{Sm}_2\text{O}_3$  peak. As temperature increases, the peak intensity becomes stronger and sharper, which is a signature of better crystalline quality of the film. It is important to note that the  $\text{BaTiO}_3$  peak is not observed in all films. This may be due to overlapping with strong  $\text{SrTiO}_3$  substrate peak.

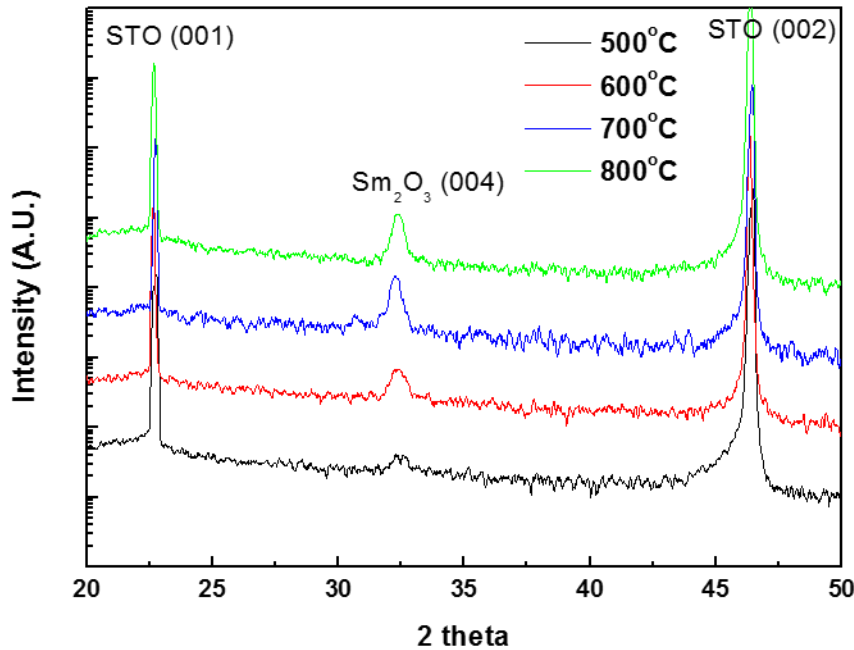


Figure 6.1.  $2\theta$ - $\omega$  XRD profiles for films grown at temperature from 500 °C to 800 °C

In addition, no significant difference was observed between 700 °C and 800 °C which means that 700 °C is enough to get film of sufficient crystallinity. Therefore in most part of our study, films were grown at 700 °C.

### 6.1.2 Effect of Sputtering Power

Figure 6.2 shows the  $2\theta$ - $\omega$  XRD scan of the nanocomposite film grown using sputter power ranging from 50 W to 200 W. To study the effect of the sputtering power on the film structure, the argon/oxygen ratio was kept at 3:1, with 6.0 Pa chamber pressure as well as 700 °C substrate temperature. To maintain constant thickness, the deposition time was adjusted to offset the low power growth (e.g. the deposition time is three times longer for 50 W deposition compared to 150 W deposition). One assumption here is that the deposition rate increases linearly with increasing sputter power.

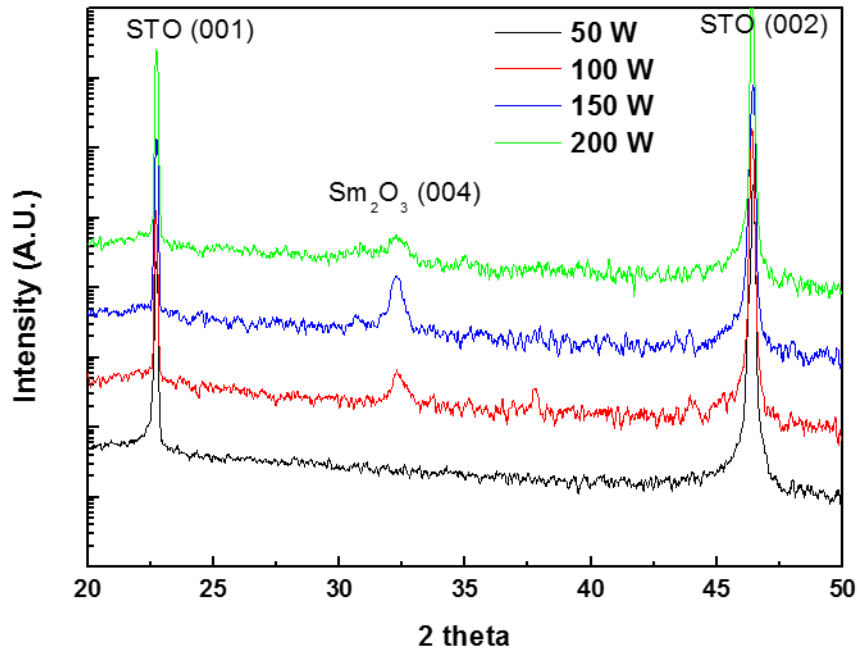


Figure 6.2.  $2\theta$ - $\omega$  XRD profiles for films grown with 50 W to 200 W power.

The assumption that deposition rate increases with sputter power is backed by the facts that the observed self-bias (DC bias voltage of the cathode) changes from 70 V to 250 V for the power range of 50 W to 200 W, which is almost linear. As the bias voltage increases, the ions in the sputter plasma were accelerated at a higher rate towards the target, resulting in more atoms being sputtered out. This self-bias voltage directly affects sputter yield, which is essentially the deposition rate.<sup>108</sup> Nevertheless, as we shall see in the later section, it is not trivial to determine the deposition rate as it depends on many factors.

As seen in Figure 6.2, at 50 W sputter power, no film peak was observed. A possible explanation for this is at low power, there is not enough self-bias voltage built up to enable sufficient sputter yield for target species (thus although the deposition time was commensurately adjusted, no sputtering actually occur because the kinetic energy of  $\text{Ar}^+$  ions are not sufficient). As the power was increased to 100 W, the  $\text{Sm}_2\text{O}_3$  peak starts to appear and at 150 W, a relatively sharp peak can be observed. Nevertheless,

when the sputtering power was further increased to 200 W, the  $\text{Sm}_2\text{O}_3$  peak fades away. This can be associated with excessive deposition rate which may result in re-sputtering of deposited film and thus may degrade the crystalline quality of the film.

### 6.1.3 Effect of Total Gas Pressure

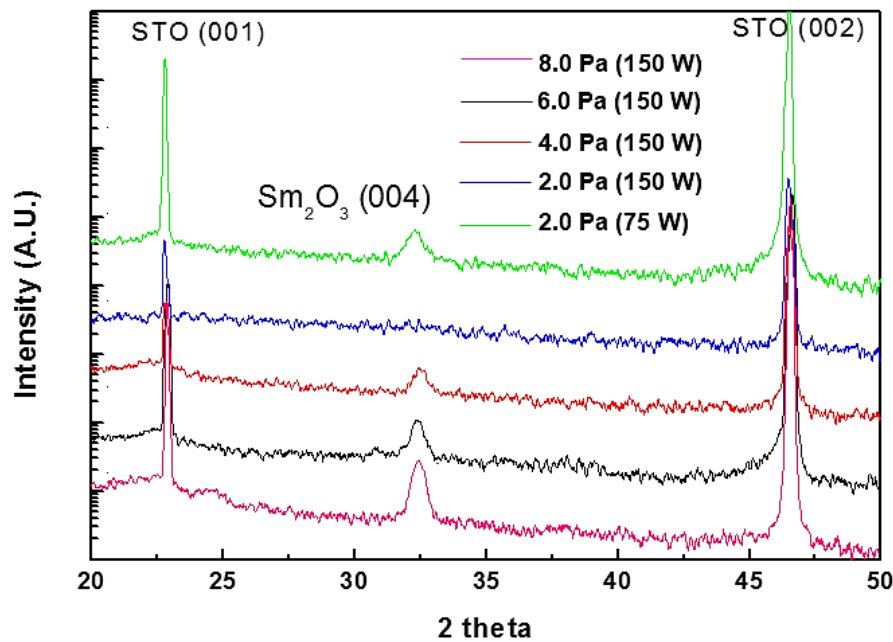


Figure 6.3.  $2\theta$ - $\omega$  XRD profiles for films grown with 2.0 Pa to 8.0 Pa total gas pressure

Figure 6.3 shows the effect of changing the total gas pressure on the film peak. To study the effect of total gas pressure, the argon/oxygen ratio was kept at 3:1, with 700 °C substrate temperature and 150 W power was used (unless otherwise indicated in the figure). At high pressure (8.0 Pa), the  $\text{Sm}_2\text{O}_3$  peak was sharp, indicating a well-crystallized film. At low pressure (e.g. 2.0 Pa), no peak was observed, which may be caused by two possible factors. Firstly, at low pressure, the ion plasma is unstable and thus deposition cannot be sustained effectively.<sup>178</sup> However, this is less likely to be the case as plasma was observed to be present throughout the film deposition. Secondly, a more likely cause for the absent of film peak is that at low pressure, the kinetic energy of depositing atoms is very high due to less collisions and scattering along their path from cathode to anode, which might have resulted in some degree of re-sputtering on

the substrate. This scenario is better illustrated in equation 6.1 in relation to self-bias which essentially determines the kinetic energy of bombarding ions.

Note that however, when the film was grown at 2.0 Pa and 75 W power, the Sm<sub>2</sub>O<sub>3</sub> peak was observed. An explanation to this phenomena can be associated to the self-bias voltage built up in the RF plasma. The self-bias voltage can be related to power and pressure through a simple equation<sup>179</sup>:

$$V_{\text{bias}} \approx \sqrt{\frac{W}{P}} \quad (6.1),$$

where  $V_{\text{bias}}$  is the self-bias,  $W$  is the sputter power and  $P$  is the total gas pressure. In our case, by lowering the sputter power from 150 W to 75 W at 2.0 Pa gas pressure, the self-bias can be maintained at a sufficient level where re-sputtering on the substrate is prevented. In other words, the effect of sputter power and total gas pressure on self-bias is inter-related. As mentioned earlier, the self-bias voltage directly affect the sputter yield which consequently dictates the deposition rate.

Thus, it can be inferred that when the self-bias is too high (as in the case of 2.0 Pa and 150 W film), Sm<sub>2</sub>O<sub>3</sub> formation is inhibited. On the other hand, when the self-bias is lowered either by increasing pressure or lowering power, Sm<sub>2</sub>O<sub>3</sub> peak was observed.

#### **6.1.4 Effect of Ar/O<sub>2</sub> Ratio**

The effect of Ar/O<sub>2</sub> ratio was also examined by keeping other deposition parameters constant. The substrate temperature was kept at 700 °C, power at 150 W, and total pressure at 6.0 Pa. The Ar/O<sub>2</sub> ratio was varied from 0.5 to 8.0, as shown in Figure 6.4. It was observed that at very low Argon/Oxygen ratio, no Sm<sub>2</sub>O<sub>3</sub> peak was observed.

As the Ar/O<sub>2</sub> ratio was increased from 0.5 to 3.0, Sm<sub>2</sub>O<sub>3</sub> peak gradually becomes stronger. Above Ar/O<sub>2</sub> ratio of 3.0, however, no significant change in the Sm<sub>2</sub>O<sub>3</sub> peak was observed. The observed trend can be understood from the deposition rate point of

view. When the level of argon is too low during the deposition, less argon ions participate in the bombardment process while some oxygen gas molecules gets ionized into oxygen ions. This may have resulted in oxygen ions (anion) bombardment of the substrate instead of cathode target which degrades the film crystallinity. In other words, there need to be sufficient level of argon in the mixture gas for crystalline phase to be properly deposited. Once the sufficient level of argon to oxygen in the mixture was reached (in our case it is 3:1), no significant change was observed in the XRD peak. On the other hand, excessive argon/oxygen ratio can result in oxygen vacancies in the film. Therefore, maintaining a sufficient level of oxygen is also essential in growing oxide film to maintain the proper oxygen stoichiometry in the film.<sup>107</sup>

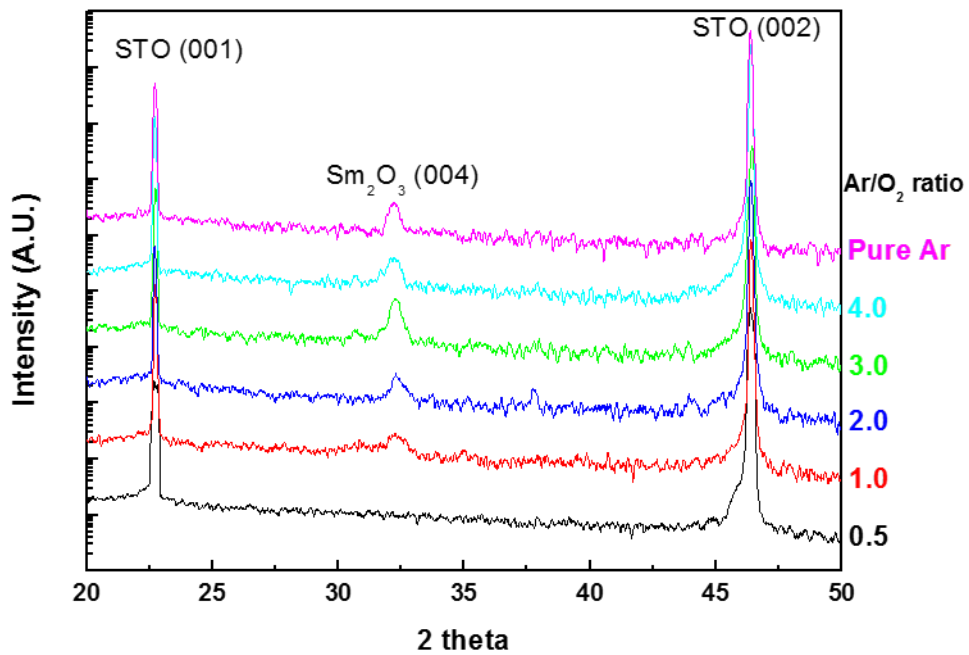


Figure 6.4.  $2\theta$ - $\omega$  XRD profiles for films grown at Ar/O<sub>2</sub> ratio of 0.5 to 8.0.

### 6.1.5 Other Characterizations and Conclusions

Figure 6.5. shows the XRD scan (top) and the PFM amplitude scan (bottom) of a BaTiO<sub>3</sub>-Sm<sub>2</sub>O<sub>3</sub> nanocomposite film grown at substrate temperature of 700 °C, sputter power of 150 W, total gas pressure of 6.0 Pa as well as argon to oxygen ratio of 3:1.

The film for PFM characterization was grown on Nb-doped STO substrate instead of STO substrate in order to provide the necessary electrical conductivity for the bottom contact. A platinum top electrode was deposited on the top surface of the sample using sputtering. It can be seen from Figure 6.5, the bright area can be associated to BaTiO<sub>3</sub> because it has piezoelectric response while Sm<sub>2</sub>O<sub>3</sub> does not have any piezoelectric response, thus is expected to appear dark. In this case, BaTiO<sub>3</sub> can be associated with the matrix due to its percolative nature while Sm<sub>2</sub>O<sub>3</sub> can be associated to the pillars. This is consistent with the results in chapter 4 which shows that at 50:50 ratio, Ba<sub>0.6</sub>Sr<sub>0.4</sub>TiO<sub>3</sub> forms the matrix while Sm<sub>2</sub>O<sub>3</sub> forms the pillars. This is also consistent with the earlier reports in PLD-grown BaTiO<sub>3</sub> – Sm<sub>2</sub>O<sub>3</sub> system which shows Sm<sub>2</sub>O<sub>3</sub> as the nano-pillars.<sup>30</sup> It is important to note that while PFM results show a hint of vertically-aligned nanocomposite (VAN) structure, no such evidence can be obtained from XRD scan (e.g. no clear BaTiO<sub>3</sub> peak was observed). In addition, Figure 6.5 does not represent all of the films grown in this study. Nevertheless, this is an encouraging preliminary step towards obtaining self-assembled VAN using sputtering because PFM data shows that the film surface consists of at least 2 different phases, one piezoelectric (the bright region in Figure 6.5 (b)) and the other one showing no piezoelectric response. Secondly, although arguments can be made that the bright region in the PFM image is the result of current leakage through conducting grain boundaries, the non-leaky shape of P-E loop as well as the low level of leakage current density shown in Figure 6.6. (a) and (c) excludes this possibility.

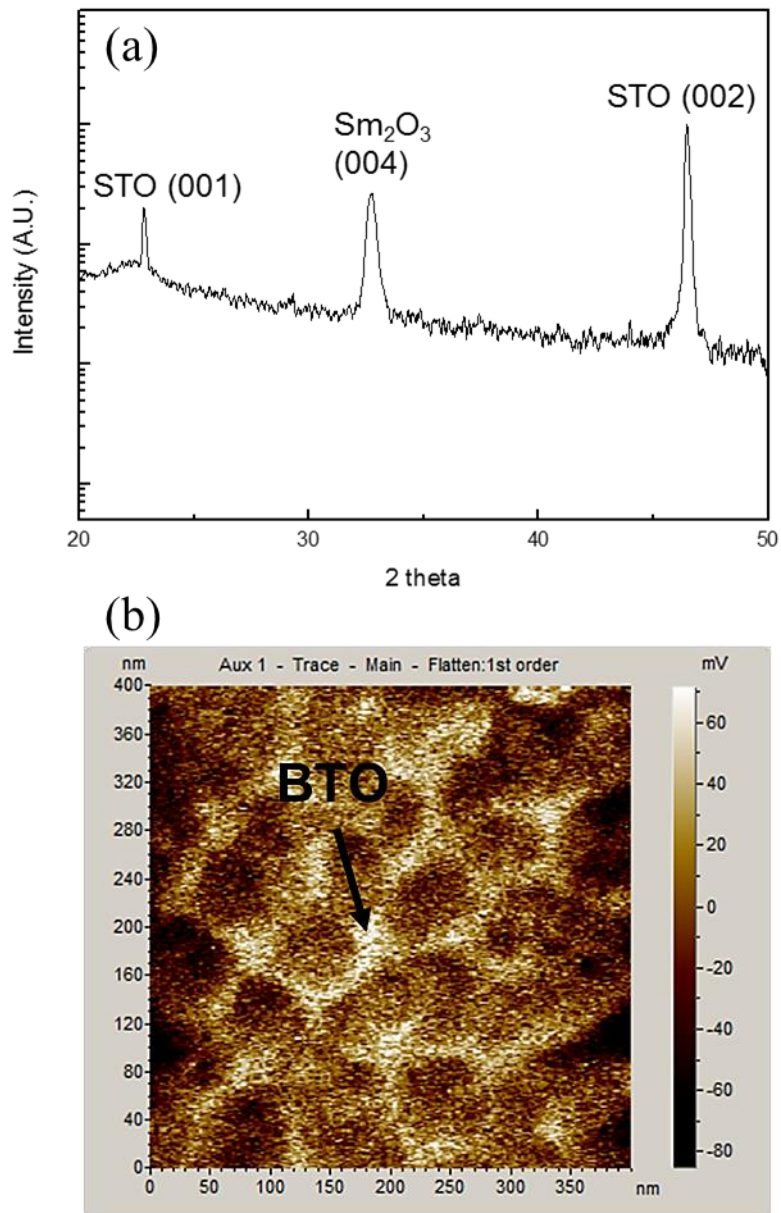


Figure 6.5. (a)  $2\theta$ - $\omega$  XRD scan and (b) PFM amplitude scan for BaTiO<sub>3</sub>-Sm<sub>2</sub>O<sub>3</sub> film grown on Nb:STO (001) conductive substrate.

In order to have clear comparison with the literature, Figure 6.6 shows the ferroelectric hysteresis curve as well as the leakage current curve of sputter-grown BaTiO<sub>3</sub>-Sm<sub>2</sub>O<sub>3</sub> film compared to PLD-grown film from the literature.<sup>30</sup>

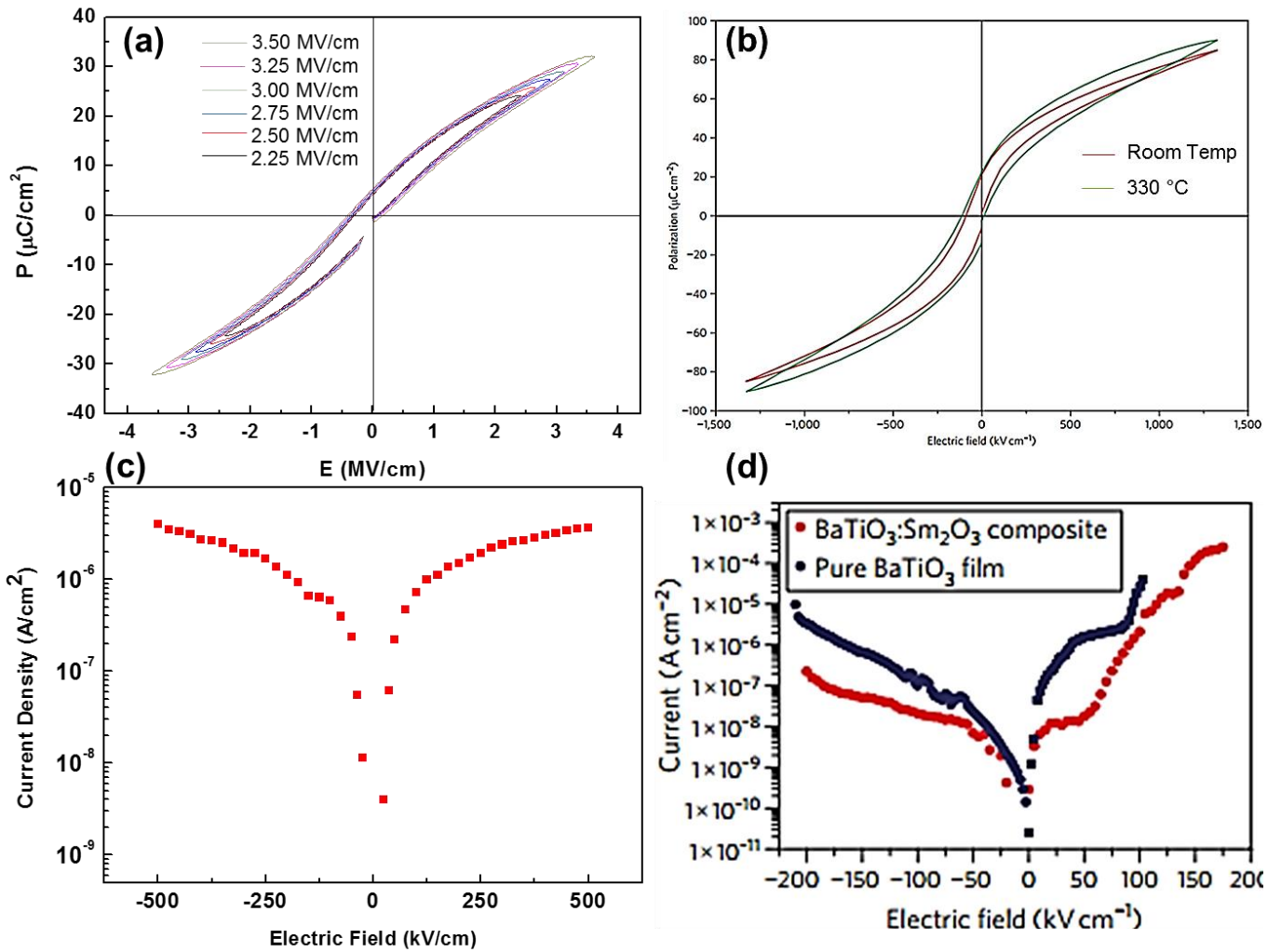


Figure 6.6. (a) Ferroelectric hysteresis loop of sputter-grown nanocomposite BaTiO<sub>3</sub>-Sm<sub>2</sub>O<sub>3</sub> film with 200 nm thickness grown on Nb:STO (001) substrate. (b) Figure adopted from literature showing PLD-grown BaTiO<sub>3</sub>-Sm<sub>2</sub>O<sub>3</sub> nanocomposite film with 1 μm thickness.<sup>30</sup> (c) J-E plot showing leakage current density of sputter-grown BaTiO<sub>3</sub>-Sm<sub>2</sub>O<sub>3</sub> film compared to (d) literature J-E plot showing leakage current of pure BaTiO<sub>3</sub> as well as PLD-grown BaTiO<sub>3</sub>-Sm<sub>2</sub>O<sub>3</sub> nanocomposite film with 600 nm thickness.<sup>30</sup> (Figure B and D from <sup>30</sup>)

As seen from Figure 6.6. (a) and (b), the sputter-grown film shows lower polarization ( $\approx 30 \mu\text{C}/\text{cm}^2$ ) compared to the PLD-grown film ( $\approx 80 \mu\text{C}/\text{cm}^2$ ). The primary reason for this is because the polarization in Figure 6.6. (a) did not saturate up until the point of dielectric breakdown. Another contributing factor that can be

associated with this is the better crystalline quality of the PLD-grown material and also the highly strained (2.35% strain) BaTiO<sub>3</sub> phase in the reported PLD-grown nanocomposite. In addition, the observed coercive field was similar between sputter-grown ( $\approx 250$  kV/cm) and PLD-grown film ( $\approx 200$  kV/cm). In addition, the sputter-grown film shows lower remnant polarization ( $\approx 5$   $\mu\text{C}/\text{cm}^2$ ) as compared to the PLD-grown film ( $\approx 21$   $\mu\text{C}/\text{cm}^2$ ).

Figure 6.6. (c) and (d) shows the comparison of leakage current density between the sputter-grown film and the PLD-grown film from literature. The leakage current of the sputter-grown film was similar to those of PLD-grown pure BaTiO<sub>3</sub> film which was approximately 1 order of magnitude higher than the PLD-grown nanocomposite film. Nevertheless, it is important to note that the sputter-grown leakage current was characterized using 2-point probe setup as opposed to 4-point probe which was used in the PLD-grown film. The use of 2-point probe to characterize leakage current might have resulted in inaccuracy of the resistivity and leakage current values due to the contribution from contact resistance.

It is important to note that while the PFM result shown in Figure 6.5 confirms phase separation on the film surface, it does not confirm that the nanocomposite film is vertically aligned. What could have been a solid confirmation was cross sectional TEM as shown in Figure 6.7. However, due to the low resolution of the available TEM as well as inferior sample preparation technique (e.g. the specimen cross section has to be atomically thin for electron beam to penetrate and thus reveal the phase-contrast), the figure did not show clear vertically aligned structure.

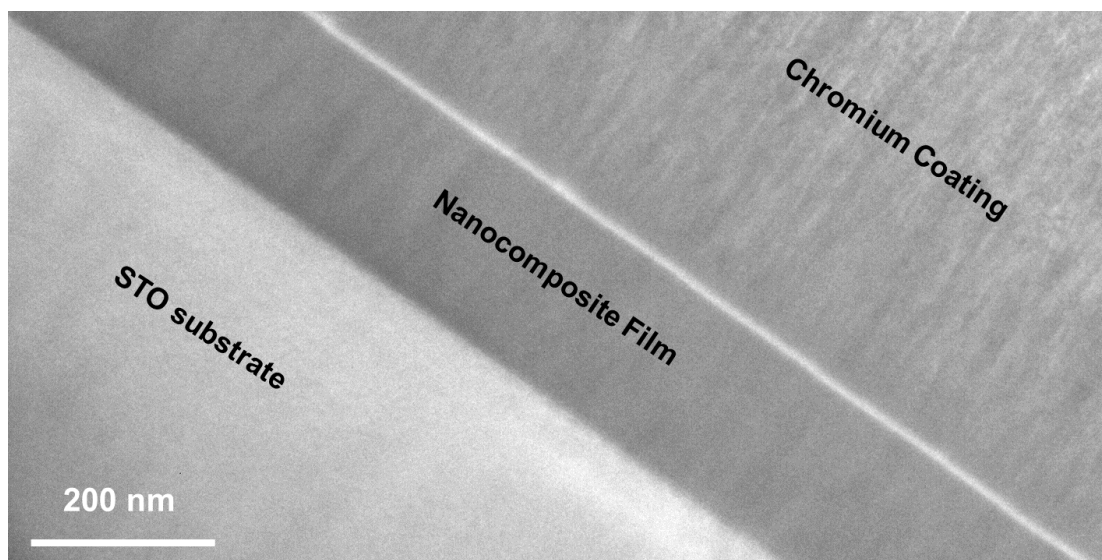


Figure 6.7. Cross section TEM of the  $\text{BaTiO}_3 - \text{Sm}_2\text{O}_3$  nanocomposite film. In this film, no obvious vertically aligned structure can be observed. (TEM was done in the Institute of Materials Research and Engineering, Singapore with the help of Dr. Nancy Wong).

In summary, ferroelectric behavior was observed in sputter-grown  $\text{BaTiO}_3\text{-Sm}_2\text{O}_3$  film, albeit inferior in terms of polarization as compared to PLD-grown film. Electrical characterization of the film shows low leakage current density as well as reasonable level of ferroelectric polarization, albeit not saturated. PFM scan confirms nanocolumnar surface of the film. However, it is important to acknowledge that the film could not be poled using PFM (which can only apply 10 V voltage) owing to its high level of thickness (200 nm) which means a voltage of more than 20 V is required to produce the necessary electric field of 1000 kV/cm, as in the case for PLD-grown film in the literature (Figure 6.6.(b)). Further to that, no clear  $\text{BaTiO}_3$  peak was observed in the XRD scan. This can be due to overlapping with the STO substrate peak and low level of crystallinity of sputter-grown film. In addition, preliminary study using TEM did not show clear vertically aligned structure.

Therefore, no solid conclusion can be drawn whether or not the nanocomposite is ferroelectric. The bottom line is that however, the nanocomposite film shows phase separation, as evidenced from PFM image shown in Figure 6.5. However, to arrive at a solid conclusion, two further experimental verification have to be carried out. Firstly,

the vertically aligned structure has to be confirmed by high resolution TEM setup (which was not available when the study was done). Secondly, film with lower level of thickness is required for electrical poling to be effective in PFM, therefore providing the possibility to confirm ferroelectricity in the film. In conclusion, this study shows some promises as well as some experimental challenges arising from sputtering VAN structure and can be a good basis for further study in this direction.

## 6.2. Sputtering Growth of Other Nanocomposite Materials

Besides the BaTiO<sub>3</sub>–Sm<sub>2</sub>O<sub>3</sub> system shown in section 6.1, we have attempted to grow two other combinations of nanocomposites namely BaTiO<sub>3</sub>–Cu<sub>2</sub>O as well as Cu<sub>2</sub>O–ZnO. The rationale of choosing the two compositions for my study was that Cu<sub>2</sub>O is a well-reported p-type material while ZnO is a well-known n-type material for photovoltaic applications.<sup>180</sup>

### 6.2.1. Cu<sub>2</sub>O-ZnO Nanocomposite

Figure 6.8 shows the 2θ-ω XRD profiles of Cu<sub>2</sub>O-ZnO nanocomposite grown using co-sputtering from two separate 3-inch targets of ZnO and Copper, respectively. It can be observed that both Cu<sub>2</sub>O and ZnO peaks were present in the nanocomposite film. It should be acknowledged that this work did not go through systematic optimization process because it was done as part of curious exploration while waiting for the commercial targets for BaTiO<sub>3</sub>-Sm<sub>2</sub>O<sub>3</sub> system. Thus, only data from film with clear peaks showing both Cu<sub>2</sub>O and ZnO phases are shown. The sputter deposition was done at 700 °C substrate temperature, argon to oxygen ratio of 3:1 and total chamber pressure of 6.0 Pa. The sputter power was adjusted to be the same (100 W) for both targets. However, the molar ratio of the two phases in the nanocomposite film is not known (or separately characterized) due to different sputter yield in different target. Deposition was carried out for 2 hours in total which consists of 20 minutes of depositing only from ZnO target, followed by 80 minutes of depositing from both targets, and lastly 20 minutes of depositing only from Cu<sub>2</sub>O target. However, no thickness data was available on this film due to limitation of characterization equipment.

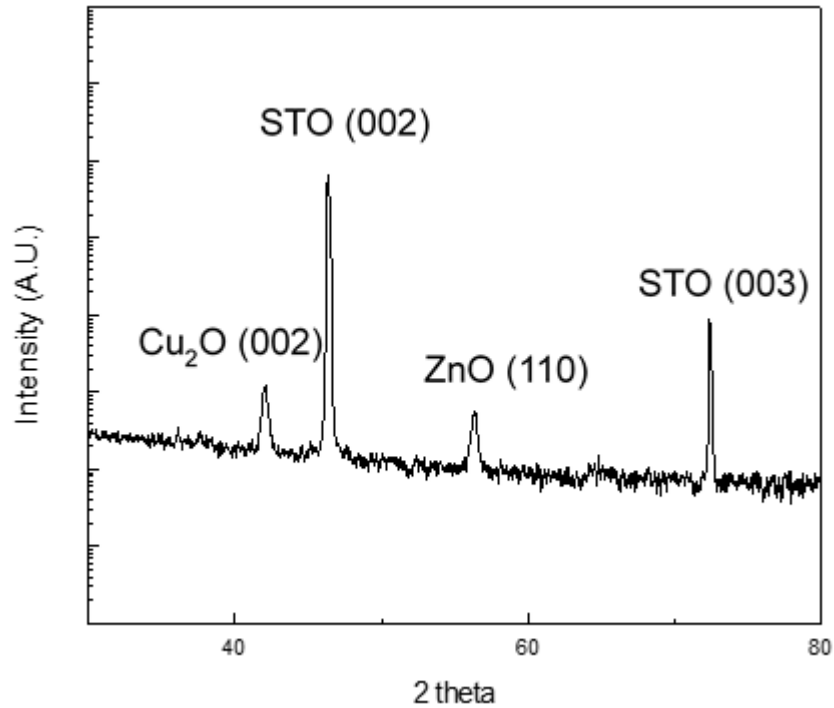


Figure 6.8.  $2\theta$ - $\omega$  XRD profile of  $\text{Cu}_2\text{O}$ - $\text{ZnO}$  nanocomposite film showing clear, separate peaks of both phases.

Preliminary photovoltaic effect characterization done on the sample did not show any open circuit voltage nor short circuit current, as shown in Figure 6.9. The primary reason of the absence of observable photovoltaic behavior can be associated with incompatible length scales in  $\text{Cu}_2\text{O}$ . Although it was well reported that nanostructured architectures can result in better charge collection,  $\text{Cu}_2\text{O}$  nanostructure was reported to have incompatibility between the nanostructure size required for efficient charge collection ( $< 1 \mu\text{m}$ ) and the thickness necessary to form enough built-in potential that prevents recombination ( $> 2 \mu\text{m}$ ).<sup>181</sup>

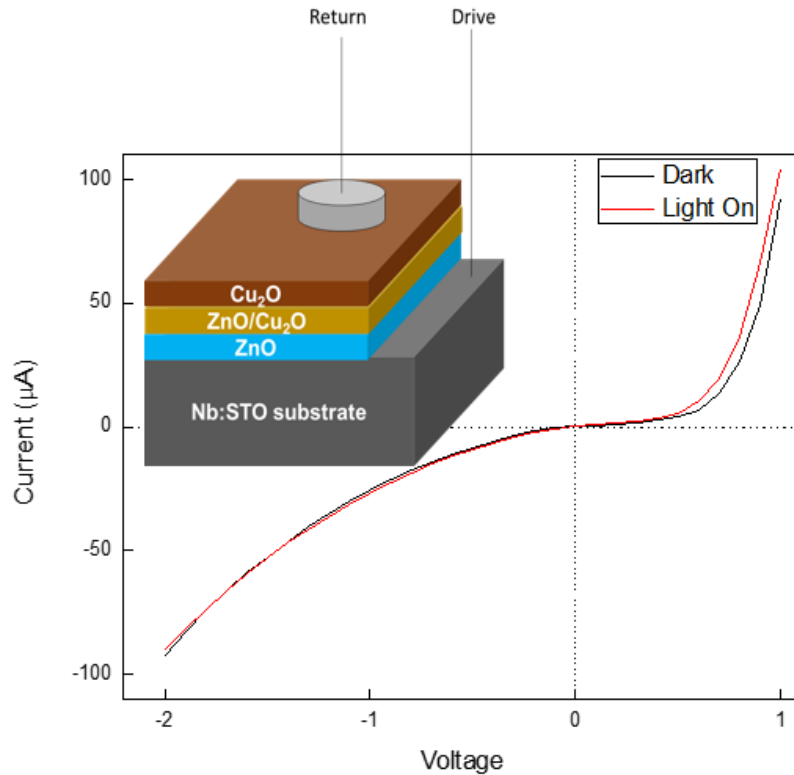


Figure 6.9. Schematic diagram showing the  $\text{Cu}_2\text{O}$ - $\text{ZnO}$  nanocomposite film as well as preliminary photovoltaic characterization.

In conclusion, although no photovoltaic properties has been observed in this system, preliminary results shows that it is possible to form phase-separated nanocomposite of oxide photovoltaic materials by sputtering without requiring careful optimization of sputter growth parameter (compared to the case for  $\text{BaTiO}_3$ - $\text{Sm}_2\text{O}_3$ ) although further study has to be conducted to confirm the morphology of the film. The primary challenge of this system is believed to lie in optimization of electrical transport properties for photovoltaic characterizations.

### 6.2.2. $\text{BaTiO}_3$ - $\text{Cu}_2\text{O}$ Nanocomposite

The rationale behind this material system is to make use of the ferroelectric built in internal electric field of  $\text{BaTiO}_3$  phase to induce charge separation in  $\text{Cu}_2\text{O}$ . Similar to  $\text{Cu}_2\text{O}$ - $\text{ZnO}$  system, no systematic optimization was conducted for this system. The nanocomposite film was grown using co-sputtering from two separate 3-inch targets of

BaTiO<sub>3</sub> and Copper, respectively. The sputter deposition was done at 700 °C substrate temperature, argon to oxygen ratio of 3:1 and total chamber pressure of 6.0 Pa. The sputter power was adjusted to be the same (100 W) for both targets. Figure 6.10 shows the 2θ-ω XRD profiles of BaTiO<sub>3</sub>-Cu<sub>2</sub>O nanocomposite. Both Cu<sub>2</sub>O and BaTiO<sub>3</sub> peaks were observed in the XRD scan. Besides XRD, FESEM scan done on this films shows rough texture with sign of phase-separation, as shown in Figure 6.11.

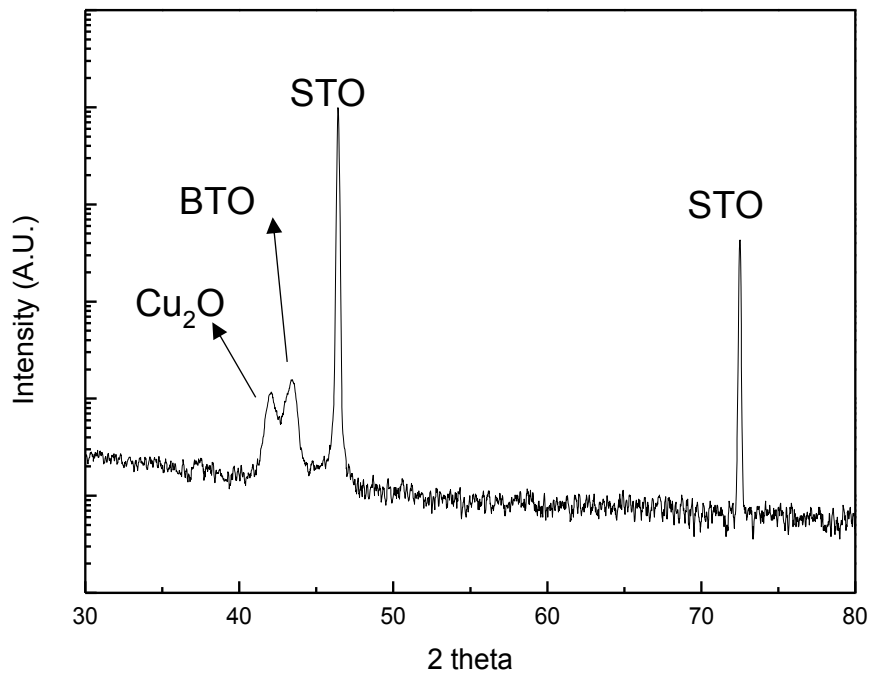


Figure 6.10. 2θ-ω XRD profile of BaTiO<sub>3</sub>-Cu<sub>2</sub>O nanocomposite film showing clear, separate peaks of both phases.

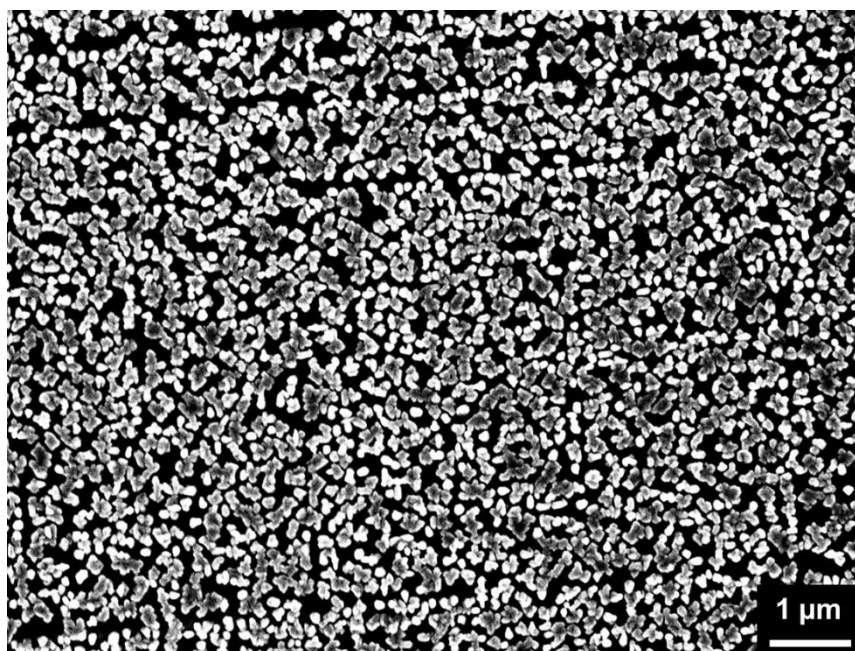


Figure 6.11. FESEM image showing rough texture of agglomerates on the BaTiO<sub>3</sub>-Cu<sub>2</sub>O nanocomposite film.

While both XRD scan and FESEM image shows phase separation of BaTiO<sub>3</sub> and Cu<sub>2</sub>O, it is by no means a solid confirmation that the two phases in the nanocomposite are vertically aligned. Thus, in order to provide additional support that the phases are indeed vertically aligned, electrical characterization was done on the sample. Figure 6.12 shows the P-E loop of the sample measured in *in-plane* vs *out-of-plane* direction.

It can be observed from Figure 6.12 that the phase-separated nanocomposite BaTiO<sub>3</sub>-Cu<sub>2</sub>O shows very leaky behavior in the *out-of-plane* direction while the *in-plane* P-E loop shows dielectric behavior. As Cu<sub>2</sub>O has very low resistivity compared to BaTiO<sub>3</sub>, the source of lossy behavior in the *out-of-plane* direction must be originated from Cu<sub>2</sub>O, which can be associated with a percolative path from which current travels in the *out-of-plane* direction. The absence of lossy behavior in the *in-plane* P-E loops re-inforce the suggestion that the nanocomposite is vertically aligned instead of randomly dispersed. Therefore, this observation points to a strong possibility that the nanocomposite is indeed vertically aligned.

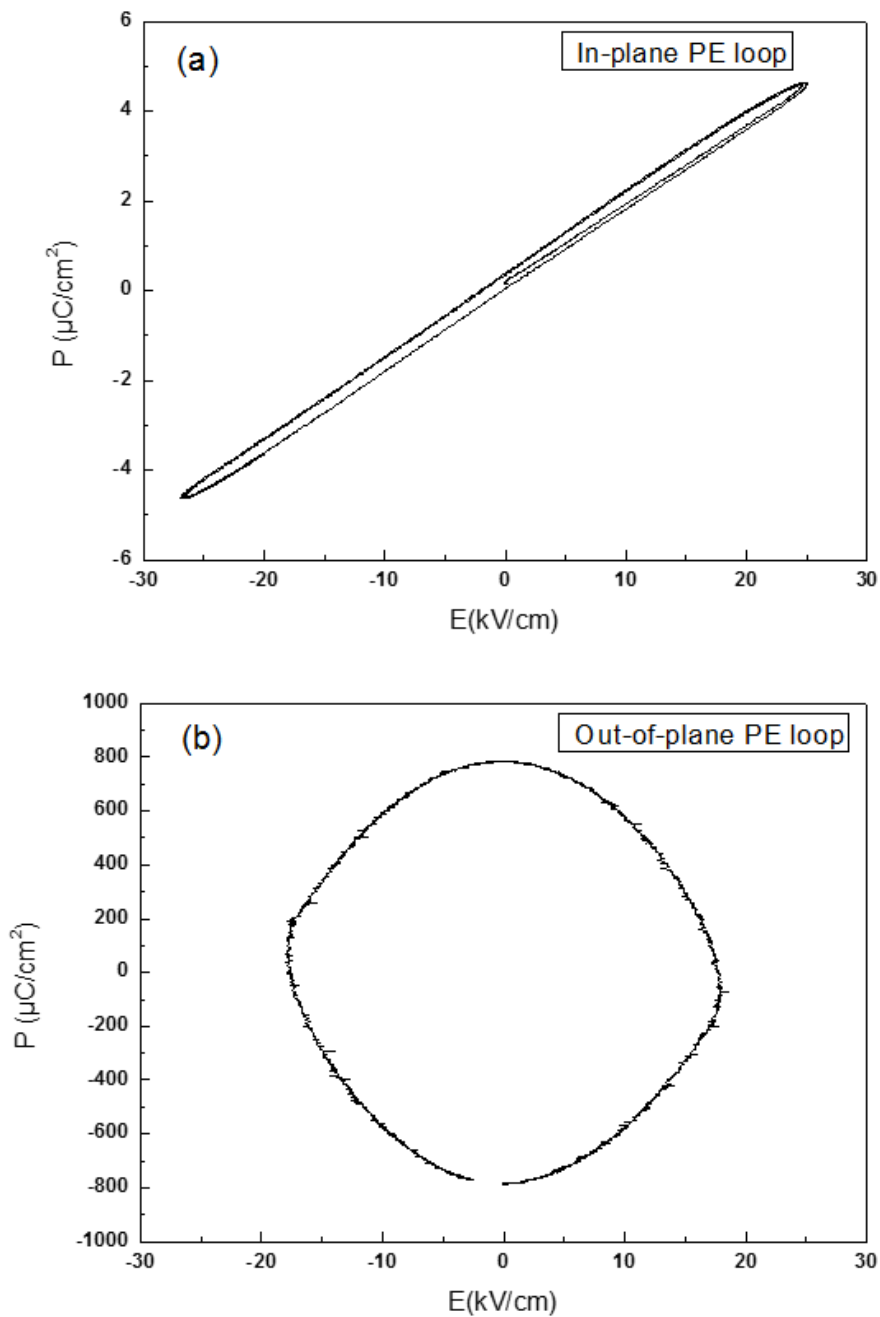


Figure 6.12. P-E loop of  $\text{BaTiO}_3\text{-Cu}_2\text{O}$  nanocomposite film in (a) *in-plane* direction and (b) *out-of-plane* direction.

In conclusion, it was observed that  $\text{BaTiO}_3\text{-Cu}_2\text{O}$  nanocomposite shows promising possibility to be vertically-aligned albeit with no systematic optimization. Detailed study is required to find out the underlying principle behind the relative ease for certain

material combination for form phase-separated vertically-aligned nanocomposite. (e.g. in BaTiO<sub>3</sub>-Cu<sub>2</sub>O case, clear and sharp peaks corresponding to both phases were observed in XRD while it was not the case for BaTiO<sub>3</sub>-Sm<sub>2</sub>O<sub>3</sub>). In my study, one possibility that can be associated with the relative ease of formation of BaTiO<sub>3</sub>-Cu<sub>2</sub>O nanocomposite as compared to two other systems is the ionic radii differences of all the species involved in the nanocomposite. As shown in Figure 6.13, Cu atom is much smaller compared to Ba atom, thus there will be lower possibility of intermixing compared to the case of BaTiO<sub>3</sub>-Sm<sub>2</sub>O<sub>3</sub> where the atomic radii of Cu and Zn are very similar.

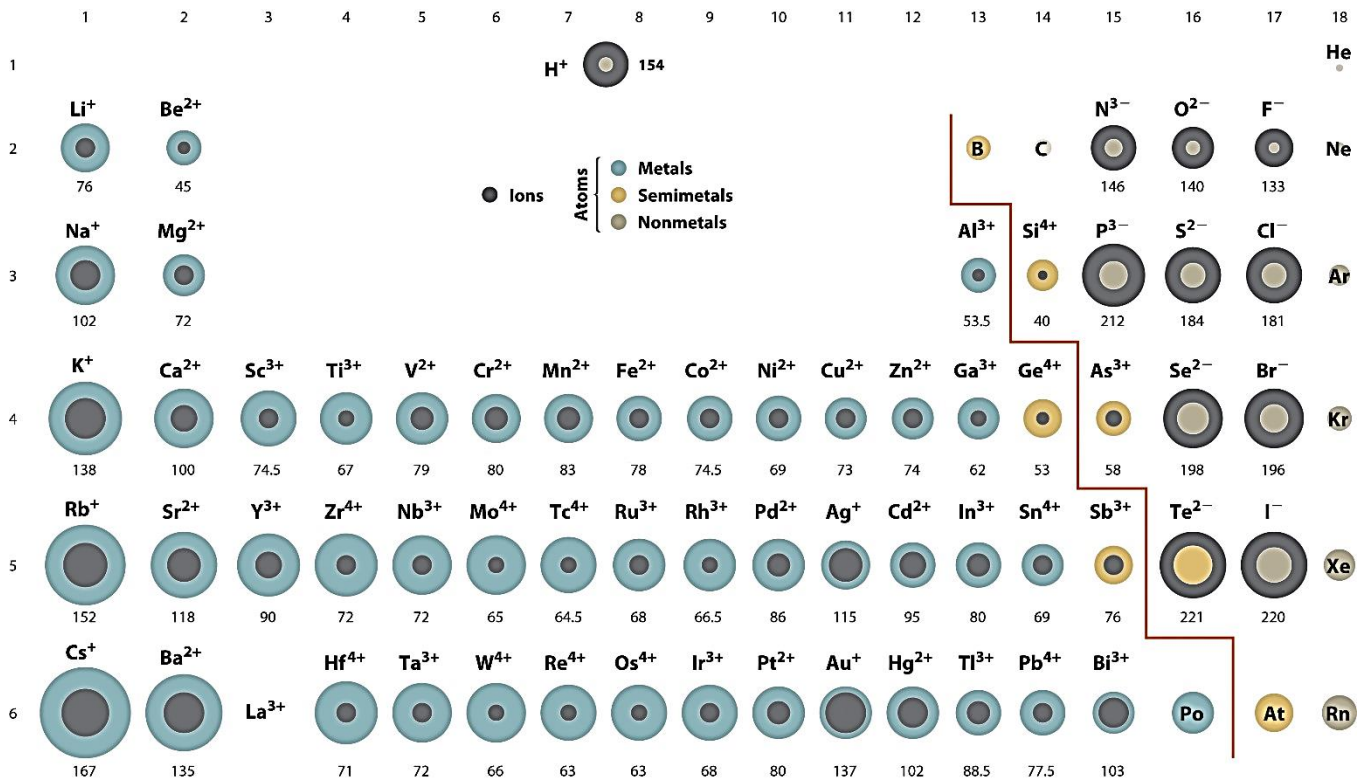


Figure 6.13. Ionic radii of different atoms of the periodic table. (Image from <sup>182</sup>).

## 6.3. Limitations and Challenges in Using Sputtering for VAN Growth

As discussed in Chapter 2, the great potential in using sputtering to grow VAN architecture compared to PLD lies in its scalability. Nevertheless, compared to PLD, sputtering process is fundamentally different. Some basic major differences listed in the table below will be discussed in more details in the subsequent sub-section.

	<b>Sputtering</b>	<b>PLD</b>
1	Different sputter yield for different materials	All materials are ablated at the same time
2	Complex inter-relationship between deposition parameters	Relatively little inter-relationship between deposition parameters
3	Continuous deposition	Short deposition pulses

Table 6.1. Fundamental differences in deposition process between sputtering and PLD.

### 6.3.1. Ablation Selectivity

It is a well-known phenomenon in sputtering that different elements have different sputter yield even under the same power.<sup>107</sup> As the deposition of VAN structure often involves complex combination of elements, this presents obvious limitations for sputtering. On the other hand, VAN structures have been successfully grown using PLD thanks to its non-selectivity during ablation process (i.e. all species are ablated simultaneously).

One way to circumvent the problem of different sputter yield is to use co-sputtering (e.g. simultaneous sputtering from different gun sources containing different targets). However, co-sputtering present another challenges due to the unique inter-dependency between deposition parameters which will be discussed in the next section

(e.g. total gas pressure may have different effect on different sources), making it hard to control the final composition of the film.

### 6.3.2. Inter-relationship between Deposition Parameters

Table 6.2 presents the comparison of deposition parameters that can be controlled in sputtering and PLD.

	<b>Sputtering</b>	<b>PLD</b>
1	Sputtering Power	Laser Fluence (energy density)
2	Total gas pressure	Total gas pressure
3	Target-substrate distance	Target-substrate distance
4	Ar/O <sub>2</sub> mixture ratio	Laser repetition rate
5	Substrate temperature	Substrate temperature

Table 6.2. Deposition parameters in sputtering and PLD.

Before we discuss about complex inter-relationship between parameters in sputtering, we will start off by discussing the deposition parameters of PLD. In PLD, most of the deposition parameters can be tuned rather independently without affecting each other. For instance, tuning laser fluence will not affect the total gas pressure in the system. Likewise, laser repetition rate, substrate temperature, and target-substrate distance can be independently adjusted to fit the deposition requirements. The only parameters that can have overlapping effect with each other is total gas pressure and target-substrate distance.

In general, when the atomic species was first ablated from the target, they have very high kinetic energy. The role of background gas pressure is to scatter and retard the violent movement of these atomic species. Thus depending on the pressure, the energy at which atomic species arrive at the substrate can be controlled. On the other hand, given constant pressure, the energy of the arriving species can also be controlled

by adjusting the distance between target and substrate (e.g. further distance will result in lowering of the kinetic energy of the atomic species). The relationship between pressure and target-substrate distance in PLD can be expressed by the following simple equation:

$$Pd^r = C \quad (6.2),$$

where P is the total gas pressure, d is the distance between target and substrate, r is a positive coefficient which is material-dependent and C is a parameter which depends on both the materials and PLD system geometry. From equation 6.2., it can be seen that increasing gas pressure has similar effect (albeit not linear due to the r factor) compared to increasing target-substrate distance and vice versa. Apart from this inter dependency between pressure and distance, however, all other parameters can be tuned independently in PLD.

Moving on to sputtering, apart from substrate temperature, all other parameters have certain degree of inter-dependency. For instance, as discussed in section 6.1.3, in equation 6.1., both sputter power and pressure can affect the built in self-bias voltage in RF sputtering, which in turn affect sputter yield and consequently, deposition rate. In addition, it is well known that in order for plasma to be self-sustaining, the product of pressure and target-substrate distance must satisfy a certain value (also known as Paschen's law).<sup>107</sup> For instance, in DC sputtering, in order for plasma to self-sustain,

$$Pd > 0.5 \text{ cm} \cdot \text{Torr} \quad (6.3),$$

where p is the total pressure (in Torr) and d is the target-substrate distance (in cm).

In addition, changing the Ar/O<sub>2</sub> ratio will directly affect the deposition rate as well. In other words, the deposition rate in sputter deposition is affected by power, gas pressure, gas mixture, as well as target-substrate distance. Therefore, it is obvious that the optimization process in sputter growth is much more tedious compared to PLD growth where most parameters can be independently controlled and studied.

### 6.3.3. Continuity of Deposition

Another important difference between sputter growth and PLD growth lies in the continuity of deposition process. For instance, in sputter growth, atomic species arrives continuously on the substrate while growth is taking process. In other words, deposition (adsorption of species) and growth happens at the same time on the substrate.

On the other hand, in PLD, high supersaturation of arriving atomic species on the target during the deposition pulse is used to impose layer-by-layer like growth. The pulsed nature of deposition in PLD cause a separation of the deposition (adsorption) and growth in time; almost no nucleation and growth takes place during the deposition pulse. Determination of the kinetic growth parameters in between the deposition pulses is, therefore, less complicated (e.g. by adjusting laser repetition rate, one can directly control the growth kinetics).<sup>107</sup>

In conclusion, the route to film growth optimization in sputtering is much more tedious compared to PLD. In our study, there are some limitations in the equipments in terms of the range of parameters that we can explore. For instance, the total gas pressure is limited at 0.5 Pa to 8.0 Pa, which is not a big range. Thus, the entire optimization process requires careful study of the effect of each parameter and circumvention of limitations in sputter growth either by modifying the equipment of by adopting new technology.

# Chapter 7 Conclusions and Future Works

This dissertation works center around a newly emerging architecture in oxide thin film, the vertically aligned nanocomposite. The main advantage of this architecture compared to conventional single/multi-layer thin films is the ability to induce and maintain large level of strain without strain relaxation at high level of thickness. Because of it being relatively recently developed architecture, no study was done to elucidate the origin of its strain states, which is of paramount importance since the understanding of strain states would enable one to more effectively design material system with desired level of strain to enhance its functional properties. In view of that, the origin of strain was elucidated by studying  $\text{Ba}_{0.6}\text{Sr}_{0.4}\text{TiO}_3\text{-Sm}_2\text{O}_3$  VAN with different phase ratios. It was concluded from the study that while phase ratios dictates which phase to be the matrix and pillar, the strain level originates from the combination of lattice mismatch as well as thermal expansion mismatch between the two phases in the nanocomposite.

In addition, to examine the importance of strain not only in the biaxial (*in-plane*) direction but also in the *out-of-plane* direction, studies of the effect of  $c/a$  ratio on physical properties were done on both  $\text{Ba}_{0.6}\text{Sr}_{0.4}\text{TiO}_3\text{-Sm}_2\text{O}_3$  and  $\text{Sm}_{0.34}\text{Sr}_{0.66}\text{MnO}_3\text{-Sm}_2\text{O}_3$  VAN thin films. It was found that ferroelectricity is enhanced by large  $c/a$  ratio in  $\text{Ba}_{0.6}\text{Sr}_{0.4}\text{TiO}_3\text{-Sm}_2\text{O}_3$  system. In addition, ferromagnetism was induced from otherwise antiferromagnetism state by inducing a strain state which results in  $c/a$  ratio of close to unity in  $\text{Sm}_{0.34}\text{Sr}_{0.66}\text{MnO}_3\text{-Sm}_2\text{O}_3$  system. These studies are important because they show different effects of strain on physical properties and thus serve as guidance for choosing the appropriate materials to give the appropriate strain level which eventually enhance its physical properties.

Finally, the potential of scalability was explored by using sputtering to grow VAN structure instead of the commonly used PLD growth. This study is extremely important

because scalability is essential for good science to translate into good applications, and sputtering generally is a more suitable method for this purpose. BaTiO<sub>3</sub>–Sm<sub>2</sub>O<sub>3</sub> was used as a primary study material due to its well reported VAN properties in the literature. Besides this, BaTiO<sub>3</sub>-Cu<sub>2</sub>O and Cu<sub>2</sub>O-ZnO were also explored. Preliminary results from XRD, SEM, TEM as well as electrical characterization of these films showed signatures of VAN structures. Nevertheless, no solid conclusion can be drawn whether or not the nanocomposites are indeed vertically aligned although signature of phase separation was observed in PFM and SEM. Likewise, the functional properties (e.g. ferroelectricity) warrants further confirmation due to limitation of experimental resource/capability. Very importantly, the vertically aligned structure has to be confirmed by high resolution TEM setup and delicate TEM sample preparation. In short, this part of study presents some initial exploration into sputtering for VAN which shines light into the primary differences between PLD and sputtering and thus can provide guidance on potential challenges in optimization process. Although extensive works still need to be done on the system, this will make a good case for further studies as well as set up the stage for further exploration of sputtering method to grow VAN structure.

Since the foundation of good research lies in asking the right questions, future work that will be interesting to explore in this area including, but not limited to the following questions:

1. Is it possible to achieve the same strain states and same functional properties enhancements in sputter-grown VAN compared to PLD grown VAN? What are the critical factors that can be potential limitations/challenges?
2. Can we achieve 3D strain states in most other materials? (e.g. not limited to oxides and metals)
3. Can VAN structure be grown on non-single crystal substrates? (e.g. glass or silicon)
4. Can VAN structure enhance other functional physical properties? (e.g. Thermoelectric)

# Reference

1. Schlom, D.; Haeni, J.; Lettieri, J.; Theis, C.; Tian, W.; Jiang, J.; Pan, X., Oxide nano-engineering using MBE. *Materials Science and Engineering: B* 2001, 87 (3), 282-291.
2. Yu, Z.; Ramdani, J.; Curless, J.; Overgaard, C.; Finder, J.; Droopad, R.; Eisenbeiser, K.; Hallmark, J.; Ooms, W.; Kaushik, V., Epitaxial oxide thin films on Si (001). *Journal of Vacuum Science & Technology B: Microelectronics and Nanometer Structures Processing, Measurement, and Phenomena* 2000, 18 (4), 2139-2145.
3. Zheng, H.; Wang, J.; Lofland, S.; Ma, Z.; Mohaddes-Ardabili, L.; Zhao, T.; Salamanca-Riba, L.; Shinde, S.; Ogale, S.; Bai, F., Multiferroic BaTiO<sub>3</sub>-CoFe<sub>2</sub>O<sub>4</sub> nanostructures. *Science* 2004, 303 (5658), 661-663.
4. MacManus-Driscoll, J. L.; Zerrer, P.; Wang, H.; Yang, H.; Yoon, J.; Fouchet, A.; Yu, R.; Blamire, M. G.; Jia, Q., Strain control and spontaneous phase ordering in vertical nanocomposite heteroepitaxial thin films. *Nature materials* 2008, 7 (4), 314.
5. Arthur, J. R., Molecular beam epitaxy. *Surface science* 2002, 500 (1), 189-217.
6. Wang, H.; Foltyn, S.; Arendt, P.; Jia, Q.; MacManus-Driscoll, J.; Stan, L.; Li, Y.; Zhang, X.; Dowden, P., Microstructure of SrTiO<sub>3</sub> buffer layers and its effects on superconducting properties of YBa<sub>2</sub>Cu<sub>3</sub>O<sub>7-δ</sub> coated conductors. *Journal of materials research* 2004, 19 (6), 1869-1875.
7. Narayan, J.; Larson, B., Domain epitaxy: A unified paradigm for thin film growth. *Journal of Applied Physics* 2003, 93 (1), 278-285.

8. Millis, A.; Darling, T.; Migliori, A., Quantifying strain dependence in “colossal” magnetoresistance manganites. *Journal of Applied Physics* 1998, 83 (3), 1588-1591.
9. Ranno, L.; Llobet, A.; Tiron, R.; Favre-Nicolin, E., Strain-induced magnetic anisotropy in epitaxial manganite films. *Applied surface science* 2002, 188 (1), 170-175.
10. Zhong, W.; Vanderbilt, D., Competing structural instabilities in cubic perovskites. *Physical review letters* 1995, 74 (13), 2587.
11. Fuchs, D.; Arac, E.; Pinta, C.; Schuppler, S.; Schneider, R.; Löhneysen, H. v., Tuning the magnetic properties of LaCoO<sub>3</sub> thin films by epitaxial strain. *Physical Review B* 2008, 77 (1), 014434.
12. Fuchs, D.; Dieterle, L.; Arac, E.; Eder, R.; Adelman, P.; Eyert, V.; Kopp, T.; Schneider, R.; Gerthsen, D.; Löhneysen, H. v., Suppression of the ferromagnetic state in LaCoO<sub>3</sub> films by rhombohedral distortion. *Physical Review B* 2009, 79 (2), 024424.
13. Adamo, C.; Ke, X.; Wang, H.; Xin, H.; Heeg, T.; Hawley, M.; Zander, W.; Schubert, J.; Schiffer, P.; Muller, D., Effect of biaxial strain on the electrical and magnetic properties of (001) La<sub>0.7</sub>Sr<sub>0.3</sub>MnO<sub>3</sub> thin films. *Applied physics letters* 2009, 95 (11), 112504.
14. Schlom, D. G.; Chen, L.-Q.; Eom, C.-B.; Rabe, K. M.; Streiffer, S. K.; Triscone, J.-M., Strain tuning of ferroelectric thin films. *Annu. Rev. Mater. Res.* 2007, 37, 589-626.
15. Pertsev, N.; Zembilgotov, A.; Tagantsev, A., Effect of mechanical boundary conditions on phase diagrams of epitaxial ferroelectric thin films. *Physical review letters* 1998, 80 (9), 1988.

16. Li, Y.; Hu, S.; Liu, Z.; Chen, L., Phase-field model of domain structures in ferroelectric thin films. *Applied Physics Letters* 2001, 78 (24), 3878-3880.
17. Pertsev, N.; Kukhar, V.; Kohlstedt, H.; Waser, R., Phase diagrams and physical properties of single-domain epitaxial  $\text{Pb}(\text{Zr}_{1-x}\text{Ti}_x)\text{O}_3$  thin films. *Physical Review B* 2003, 67 (5), 054107.
18. Haeni, J.; Chang, W.; Uecker, R., P. reiche, YL Li, S. Choudhury, W. Tian, ME Hawley, B. Craigo, AK Tagantsev, XQ Pan, S. K. Streiffer, LQ Chen, SW Kirchoefer, J. Levy, DG Schlom. Room-temperature ferroelectricity in strained  $\text{SrTiO}_3$ . *Nature* 2004, 430, 758.
19. James, A.; Xi, X., Effects of buffer layer thickness and strain on the dielectric properties of epitaxial  $\text{SrTiO}_3$  thin films. *Journal of applied physics* 2002, 92 (10), 6149-6152.
20. Zhang, Z.; Chen, Y.; Yang, S.; Zhang, F.; Ma, B.; Xu, B.; Zeng, Y.; Wang, Z.; Zhang, X., Effect of a low-temperature thin buffer layer on the strain accommodation of  $\text{In}_{0.25}\text{Ga}_{0.75}\text{As}$  grown on a  $\text{GaAs}$  (001) substrate. *Semiconductor science and technology* 2003, 18 (11), 955.
21. Uecker, R.; Bertram, R.; Brützm, M.; Galazka, Z.; Gesing, T. M.; Gugushev, C.; Klimm, D.; Klupsch, M.; Kwasniewski, A.; Schlom, D. G., Large-lattice-parameter perovskite single-crystal substrates. *Journal of Crystal Growth* 2017, 457, 137-142.
22. Bozovic, I.; Logvenov, G.; Belca, I.; Narimbetov, B.; Sveklo, I., Epitaxial Strain and Superconductivity in  $\text{La}_{2-x}\text{Sr}_x\text{CuO}_4$  Thin Films. *Physical review letters* 2002, 89 (10), 107001.

23. Jiang, J.; Pan, X.; Tian, W.; Theis, C.; Schlom, D., Abrupt PbTiO<sub>3</sub>/SrTiO<sub>3</sub> superlattices grown by reactive molecular beam epitaxy. *Applied Physics Letters* 1999, 74 (19), 2851-2853.
24. Tenne, D.; Bruchhausen, A.; Lanzillotti-Kimura, N.; Fainstein, A.; Katiyar, R.; Cantarero, A.; Soukiassian, A.; Vaithyanathan, V.; Haeni, J.; Tian, W., Probing nanoscale ferroelectricity by ultraviolet Raman spectroscopy. *Science* 2006, 313 (5793), 1614-1616.
25. Weal, E.; Patnaik, S.; Bi, Z.; Wang, H.; Fix, T.; Kursumovic, A.; Driscoll, J. M., Coexistence of strong ferromagnetism and polar switching at room temperature in Fe<sub>3</sub>O<sub>4</sub>–BiFeO<sub>3</sub> nanocomposite thin films. *Applied Physics Letters* 2010, 97 (15), 153121.
26. Bousquet, E.; Dawber, M.; Stucki, N.; Lichtensteiger, C.; Hermet, P.; Gariglio, S.; Triscone, J.-M.; Ghosez, P., Improper ferroelectricity in perovskite oxide artificial superlattices. *Nature* 2008, 452 (7188), 732.
27. MacManus-Driscoll, J.; Suwardi, A.; Kursumovic, A.; Bi, Z.; Tsai, C.-F.; Wang, H.; Jia, Q.; Lee, O. J., New strain states and radical property tuning of metal oxides using a nanocomposite thin film approach. *APL Materials* 2015, 3 (6), 062507.
28. MacManus-Driscoll, J. L., Self-assembled heteroepitaxial oxide nanocomposite thin film structures: designing interface-induced functionality in electronic materials. *Advanced Functional Materials* 2010, 20 (13), 2035-2045.
29. MacManus-Driscoll, J.; Suwardi, A.; Wang, H., Composite epitaxial thin films: A new platform for tuning, probing, and exploiting mesoscale oxides. *MRS bulletin* 2015, 40 (11), 933-942.

30. Harrington, S. A.; Zhai, J.; Denev, S.; Gopalan, V.; Wang, H.; Bi, Z.; Redfern, S. A.; Baek, S.-H.; Bark, C. W.; Eom, C.-B., Thick lead-free ferroelectric films with high Curie temperatures through nanocomposite-induced strain. *Nature nanotechnology* 2011, 6 (8), 491-495.
31. Zavaliche, F.; Zheng, H.; Mohaddes-Ardabili, L.; Yang, S.; Zhan, Q.; Shafer, P.; Reilly, E.; Chopdekar, R.; Jia, Y.; Wright, P., Electric field-induced magnetization switching in epitaxial columnar nanostructures. *Nano letters* 2005, 5 (9), 1793-1796.
32. Zheng, H.; Straub, F.; Zhan, Q.; Yang, P. L.; Hsieh, W. K.; Zavaliche, F.; Chu, Y. H.; Dahmen, U.; Ramesh, R., Self-Assembled Growth of BiFeO<sub>3</sub>-CoFe<sub>2</sub>O<sub>4</sub> Nanostructures. *Advanced Materials* 2006, 18 (20), 2747-2752.
33. Zheng, H.; Kreisel, J.; Chu, Y.-H.; Ramesh, R.; Salamanca-Riba, L., Heteroepitaxially enhanced magnetic anisotropy in BaTiO<sub>3</sub> - CoFe<sub>2</sub>O<sub>4</sub> nanostructures. *Applied physics letters* 2007, 90 (11), 113113.
34. Comes, R.; Liu, H.; Khokhlov, M.; Kasica, R.; Lu, J.; Wolf, S. A., Directed self-assembly of epitaxial CoFe<sub>2</sub>O<sub>4</sub>-BiFeO<sub>3</sub> multiferroic nanocomposites. *Nano letters* 2012, 12 (5), 2367-2373.
35. Dix, N.; Muralidharan, R.; Rebled, J.-M.; Estradé, S.; Peiró, F.; Varela, M.; Fontcuberta, J.; Sánchez, F., Selectable spontaneous polarization direction and magnetic anisotropy in BiFeO<sub>3</sub> - CoFe<sub>2</sub>O<sub>4</sub> epitaxial nanostructures. *ACS nano* 2010, 4 (8), 4955-4961.
36. Wang, Z.; Yang, Y.; Viswan, R.; Li, J.; Viehland, D., Giant electric field controlled magnetic anisotropy in epitaxial BiFeO<sub>3</sub>-CoFe<sub>2</sub>O<sub>4</sub> thin film heterostructures on single crystal Pb(Mg<sub>1/3</sub>Nb<sub>2/3</sub>)<sub>0.7</sub>Ti<sub>0.3</sub>O<sub>3</sub> substrate. *Applied Physics Letters* 2011, 99 (4), 043110.

37. Liao, S.-C.; Tsai, P.-Y.; Liang, C.-W.; Liu, H.-J.; Yang, J.-C.; Lin, S.-J.; Lai, C.-H.; Chu, Y.-H., Misorientation control and functionality design of nanopillars in self-assembled Perovskite– Spinel heteroepitaxial nanostructures. *ACS nano* 2011, 5 (5), 4118-4122.
38. Yan, L.; Xing, Z.; Wang, Z.; Wang, T.; Lei, G.; Li, J.; Viehland, D., Direct measurement of magnetoelectric exchange in self-assembled epitaxial BiFeO<sub>3</sub>–CoFe<sub>2</sub>O<sub>4</sub> nanocomposite thin films. *Applied Physics Letters* 2009, 94 (19), 192902.
39. Zhan, Q.; Yu, R.; Crane, S.; Zheng, H.; Kisielowski, C.; Ramesh, R., Structure and interface chemistry of perovskite-spinel nanocomposite thin films. *Applied physics letters* 2006, 89 (17), 172902.
40. Crane, S.; Bihler, C.; Brandt, M.; Goennenwein, S.; Gajek, M.; Ramesh, R., Tuning magnetic properties of magnetoelectric BiFeO<sub>3</sub>–NiFe<sub>2</sub>O<sub>4</sub> nanostructures. *Journal of magnetism and magnetic Materials* 2009, 321 (4), L5-L9.
41. Li, J.; Levin, I.; Slutsker, J.; Provenzano, V.; Schenck, P. K.; Ramesh, R.; Ouyang, J.; Roytburd, A. L., Self-assembled multiferroic nanostructures in the CoFe<sub>2</sub>O<sub>4</sub>-PbTiO<sub>3</sub> system. *Applied Physics Letters* 2005, 87 (7), 072909.
42. Tan, Z.; Slutsker, J.; Roytburd, A. L., Epitaxial self-assembly of multiferroic nanostructures. *Journal of Applied Physics* 2009, 105 (6), 061615.
43. Levin, I.; Li, J.; Slutsker, J.; Roytburd, A. L., Design of Self-Assembled Multiferroic Nanostructures in Epitaxial Films. *Advanced Materials* 2006, 18 (15), 2044-2047.
44. Moshnyaga, V.; Damaschke, B.; Shapoval, O.; Belenchuk, A.; Faupel, J.; Lebedev, O.; Verbeeck, J.; Van Tendeloo, G.; Mücksch, M.; Tsurkan, V., Structural phase

- transition at the percolation threshold in epitaxial  $(\text{La}_{0.7}\text{Ca}_{0.3}\text{MnO}_3)_{1-x}:(\text{MgO})_x$  nanocomposite films. *Nature materials* 2003, 2 (4), 247.
45. Dix, N.; Muralidharan, R.; Guyonnet, J.; Warot-Fonrose, B.; Varela, M.; Paruch, P.; Sánchez, F.; Fontcuberta, J., On the strain coupling across vertical interfaces of switchable  $\text{BiFeO}_3$ – $\text{CoFe}_2\text{O}_4$  multiferroic nanostructures. *Applied Physics Letters* 2009, 95 (6), 062907.
  46. Nagarajan, V.; Jia, C.; Kohlstedt, H.; Waser, R.; Misirlioglu, I.; Alpay, S.; Ramesh, R., Misfit dislocations in nanoscale ferroelectric heterostructures. *Applied Physics Letters* 2005, 86 (19), 192910.
  47. Choi, K. J.; Biegalski, M.; Li, Y.; Sharan, A.; Schubert, J.; Uecker, R.; Reiche, P.; Chen, Y.; Pan, X.; Gopalan, V., Enhancement of ferroelectricity in strained  $\text{BaTiO}_3$  thin films. *Science* 2004, 306 (5698), 1005-1009.
  48. Lee, O.; Harrington, S. A.; Kursumovic, A.; Defay, E.; Wang, H.; Bi, Z.; Tsai, C.-F.; Yan, L.; Jia, Q.; MacManus-Driscoll, J. L., Extremely high tunability and low loss in nanoscaffold ferroelectric films. *Nano letters* 2012, 12 (8), 4311-4317.
  49. Yang, H.; Wang, H.; Yoon, J.; Wang, Y.; Jain, M.; Feldmann, D. M.; Dowden, P. C.; MacManus-Driscoll, J. L.; Jia, Q., Vertical Interface Effect on the Physical Properties of Self-Assembled Nanocomposite Epitaxial Films. *Advanced Materials* 2009, 21 (37), 3794-3798.
  50. Bi, Z.; Lee, J. H.; Yang, H.; Jia, Q.; MacManus-Driscoll, J. L.; Wang, H., Tunable lattice strain in vertically aligned nanocomposite  $(\text{BiFeO}_3)_x:(\text{Sm}_2\text{O}_3)_{1-x}$  thin films. *Journal of Applied Physics* 2009, 106 (9), 094309.
  51. Bi, Z.; Anderoglu, O.; Zhang, X.; MacManus-Driscoll, J. L.; Yang, H.; Jia, Q.; Wang, H., Nanoporous thin films with controllable nanopores processed from vertically aligned nanocomposites. *Nanotechnology* 2010, 21 (28), 285606.

52. Yang, H.; Wang, H.; Zou, G.; Jain, M.; Suvorova, N.; Feldmann, D.; Dowden, P.; DePaula, R.; MacManus-Driscoll, J.; Taylor, A., Leakage mechanisms of self-assembled  $(\text{BiFeO}_3)_{0.5}:(\text{Sm}_2\text{O}_3)_{0.5}$  nanocomposite films. *Applied Physics Letters* 2008, 93 (14), 142904.
53. Chen, A.; Bi, Z.; Jia, Q.; MacManus-Driscoll, J. L.; Wang, H., Microstructure, vertical strain control and tunable functionalities in self-assembled, vertically aligned nanocomposite thin films. *Acta Materialia* 2013, 61 (8), 2783-2792.
54. Fix, T.; Choi, E.-M.; Robinson, J. W.; Lee, S. B.; Chen, A.; Prasad, B.; Wang, H.; Blamire, M. G.; MacManus-Driscoll, J. L., Electric-field control of ferromagnetism in a nanocomposite via a ZnO phase. *Nano letters* 2013, 13 (12), 5886-5890.
55. Liu, H.-J.; Chen, L.-Y.; He, Q.; Liang, C.-W.; Chen, Y.-Z.; Chien, Y.-S.; Hsieh, Y.-H.; Lin, S.-J.; Arenholz, E.; Luo, C.-W., Epitaxial photostriction–magnetostriction coupled self-assembled nanostructures. *Acs Nano* 2012, 6 (8), 6952-6959.
56. Cole, M.; Nothwang, W.; Hubbard, C.; Ngo, E.; Ervin, M., Low dielectric loss and enhanced tunability of  $\text{Ba}_{0.6}\text{Sr}_{0.4}\text{TiO}_3$  based thin films via material compositional design and optimized film processing methods. *Journal of applied physics* 2003, 93 (11), 9218-9225.
57. Cole, M. W.; Hubbard, C.; Ngo, E.; Ervin, M.; Wood, M.; Geyer, R., Structure–property relationships in pure and acceptor-doped  $\text{Ba}_{1-x}\text{Sr}_x\text{TiO}_3$  thin films for tunable microwave device applications. *Journal of applied physics* 2002, 92 (1), 475-483.
58. Joshi, P.; Cole, M., Mg-doped  $\text{Ba}_{0.6}\text{Sr}_{0.4}\text{TiO}_3$  thin films for tunable microwave applications. *Applied Physics Letters* 2000, 77 (2), 289-291.

59. Kong, L. B.; Li, S.; Zhang, T.; Zhai, J.; Boey, F. C.; Ma, J., Electrically tunable dielectric materials and strategies to improve their performances. *Progress in Materials Science* 2010, 55 (8), 840-893.
60. Park, B. H.; Jia, Q., Enhanced dielectric properties of (Ba, Sr)TiO<sub>3</sub> thin films applicable to tunable microwave devices. *Japanese journal of applied physics* 2002, 41 (11S), 7222.
61. Chong, K.; Kong, L.; Chen, L.; Yan, L.; Tan, C.; Yang, T.; Ong, C.; Osipowicz, T., Improvement of dielectric loss tangent of Al<sub>2</sub>O<sub>3</sub> doped Ba<sub>0.5</sub>Sr<sub>0.5</sub>TiO<sub>3</sub> thin films for tunable microwave devices. *Journal of applied physics* 2004, 95 (3), 1416-1419.
62. Yamada, T.; Sandu, C. S.; Gureev, M.; Sherman, V. O.; Noeth, A.; Mural, P.; Tagantsev, A. K.; Setter, N., Self-Assembled Perovskite-Fluorite Oblique Nanostructures for Adaptive (Tunable) Electronics. *Advanced Materials* 2009, 21 (13), 1363-1367.
63. Yamada, T.; Sandu, C.; Gureev, M.; Tagantsev, A.; Mural, P.; Funakubo, H.; Setter, N. In *Self-assembled ferroelectric-dielectric nanocomposite films for tunable applications*, IOP Conference Series: Materials Science and Engineering, IOP Publishing: 2010; p 012010.
64. MacManus-Driscoll, J.; Foltyn, S.; Jia, Q.; Wang, H.; Serquis, A.; Civale, L.; Maiorov, B.; Hawley, M.; Maley, M.; Peterson, D., Strongly enhanced current densities in superconducting coated conductors of YBa<sub>2</sub>Cu<sub>3</sub>O<sub>7-x</sub> + BaZrO<sub>3</sub>. *Nature materials* 2004, 3 (7), 439.
65. Zhu, Y.; Tsai, C.-F.; Wang, J.; Kwon, J. H.; Wang, H.; Varanasi, C. V.; Burke, J.; Brunke, L.; Barnes, P. N., Interfacial defects distribution and strain coupling in the

- vertically aligned nanocomposite  $\text{YBa}_2\text{Cu}_3\text{O}_{7-x}/\text{BaSnO}_3$  thin films. *Journal of Materials Research* **2012**, *27* (13), 1763-1769.
66. Sieger, M.; Hänisch, J.; Iida, K.; Gaitzsch, U.; Rodig, C.; Schultz, L.; Holzapfel, B.; Hühne, R. In *Pulsed laser deposition of thick BaHfO<sub>3</sub>-doped YBa<sub>2</sub>Cu<sub>3</sub>O<sub>7-δ</sub> films on highly alloyed textured Ni-W tapes*, Journal of Physics: Conference Series, IOP Publishing: 2014; p 022032.
67. Harrington, S.; Durrell, J.; Maiorov, B.; Wang, H.; Wimbush, S.; Kursumovic, A.; Lee, J.; MacManus-Driscoll, J., Self-assembled, rare earth tantalate pyrochlore nanoparticles for superior flux pinning in  $\text{YBa}_2\text{Cu}_3\text{O}_{7-\delta}$  films. *Superconductor Science and Technology* **2008**, *22* (2), 022001.
68. Ercolano, G.; Harrington, S.; Wang, H.; Tsai, C.; MacManus-Driscoll, J., Enhanced flux pinning in  $\text{YBa}_2\text{Cu}_3\text{O}_{7-\delta}$  thin films using Nb-based double perovskite additions. *Superconductor Science and Technology* **2010**, *23* (2), 022003.
69. Wu, H.; Chai, G.; Xu, B.; Li, J.; Zhang, Z., Effect of out-of-plane misfit strain on phase diagrams and ferroelectric properties of ferroelectric films in vertical nanocomposite structures. *Applied Physics A* **2013**, *113* (1), 155-160.
70. Khatkhatay, F.; Chen, A.; Lee, J. H.; Zhang, W.; Abdel-Raziq, H.; Wang, H., Ferroelectric properties of vertically aligned nanostructured  $\text{BaTiO}_3\text{-CeO}_2$  thin films and their integration on silicon. *ACS applied materials & interfaces* **2013**, *5* (23), 12541-12547.
71. Karimi, S.; Reaney, I.; Han, Y.; Pokorny, J.; Sterianou, I., Crystal chemistry and domain structure of rare-earth doped  $\text{BiFeO}_3$  ceramics. *Journal of materials science* **2009**, *44* (19), 5102-5112.

72. Luo, H.; Yang, H.; Baily, S. A.; Ugurlu, O.; Jain, M.; Hawley, M. E.; McCleskey, T. M.; Burrell, A. K.; Bauer, E.; Civale, L., Self-assembled epitaxial nanocomposite BaTiO<sub>3</sub>- NiFe<sub>2</sub>O<sub>4</sub> films prepared by polymer-assisted deposition. *Journal of the American Chemical Society* **2007**, *129* (46), 14132-14133.
73. Chen, A.; Bi, Z.; Tsai, C. F.; Lee, J.; Su, Q.; Zhang, X.; Jia, Q.; MacManus-Driscoll, J. L.; Wang, H., Tunable low-field magnetoresistance in (La<sub>0.7</sub>Sr<sub>0.3</sub>MnO<sub>3</sub>)<sub>0.5</sub>:(ZnO)<sub>0.5</sub> self-assembled vertically aligned nanocomposite thin films. *Advanced Functional Materials* **2011**, *21* (13), 2423-2429.
74. Chen, A.; Bi, Z.; Hazariwala, H.; Zhang, X.; Su, Q.; Chen, L.; Jia, Q.; MacManus-Driscoll, J. L.; Wang, H., Microstructure, magnetic, and low-field magnetotransport properties of self-assembled (La<sub>0.7</sub>Sr<sub>0.3</sub>MnO<sub>3</sub>)<sub>0.5</sub>:(CeO<sub>2</sub>)<sub>0.5</sub> vertically aligned nanocomposite thin films. *Nanotechnology* **2011**, *22* (31), 315712.
75. Bi, Z.; Weal, E.; Luo, H.; Chen, A.; MacManus-Driscoll, J. L.; Jia, Q.; Wang, H., Microstructural and magnetic properties of (La<sub>0.7</sub>Sr<sub>0.3</sub>MnO<sub>3</sub>)<sub>0.7</sub>:(Mn<sub>3</sub>O<sub>4</sub>)<sub>0.3</sub> nanocomposite thin films. *Journal of Applied Physics* **2011**, *109* (5), 054302.
76. Ning, X.; Wang, Z.; Zhang, Z., Large, Temperature-Tunable Low-Field Magnetoresistance in La<sub>0.7</sub>Sr<sub>0.3</sub>MnO<sub>3</sub>: NiO Nanocomposite Films Modulated by Microstructures. *Advanced Functional Materials* **2014**, *24* (34), 5393-5401.
77. Moshnyaga, V.; Damaschke, B.; Shapoval, O.; Belenchuk, A.; Faupel, J.; Lebedev, O.; Verbeeck, J.; Van Tendeloo, G.; Mücksch, M.; Tsurkan, V., Structural phase transition at the percolation threshold in epitaxial (La<sub>0.7</sub>Ca<sub>0.3</sub>MnO<sub>3</sub>)<sub>1-x</sub>:(MgO)<sub>x</sub> nanocomposite films. *Nature materials* **2003**, *2* (4), 247.
78. Sangle, A. L.; Lee, O. J.; Kursumovic, A.; Zhang, W.; Chen, A.; Wang, H.; MacManus-Driscoll, J. L., Very high commutation quality factor and dielectric

tunability in nanocomposite SrTiO<sub>3</sub> thin films with T<sub>c</sub> enhanced to > 300° C.

*Nanoscale* **2018**.

79. Zhu, Y.; Chang, W. S.; Yu, R.; Liu, R.; Wei, T.-C.; He, J.-H.; Chu, Y.-H.; Zhan, Q., Spontaneous orientation-tuning driven by the strain variation in self-assembled ZnO-SrRuO<sub>3</sub> heteroepitaxy. *Applied Physics Letters* **2015**, *107* (19), 191902.
80. Lee, O.; Kursumovic, A.; Bi, Z.; Tsai, C. F.; Wang, H.; MacManus-Driscoll, J. L., Giant Enhancement of Polarization and Strong Improvement of Retention in Epitaxial Ba<sub>0.6</sub>Sr<sub>0.4</sub>TiO<sub>3</sub>-Based Nanocomposites. *Advanced Materials Interfaces* **2017**, *4* (15).
81. Liu, H. J.; Tra, V. T.; Chen, Y. J.; Huang, R.; Duan, C. G.; Hsieh, Y. H.; Lin, H. J.; Lin, J. Y.; Chen, C. T.; Ikuhara, Y., Large Magnetoresistance in Magnetically Coupled SrRuO<sub>3</sub>-CoFe<sub>2</sub>O<sub>4</sub> Self-assembled Nanostructures. *Advanced Materials* **2013**, *25* (34), 4753-4759.
82. Li, L.; Sun, L.; Gomez-Diaz, J. S.; Hogan, N. L.; Lu, P.; Khatkhatay, F.; Zhang, W.; Jian, J.; Huang, J.; Su, Q., Self-Assembled Epitaxial Au-Oxide Vertically Aligned Nanocomposites for Nanoscale Metamaterials. *Nano letters* 2016, *16* (6), 3936-3943.
83. Su, Q.; Zhang, W.; Lu, P.; Fang, S.; Khatkhatay, F.; Jian, J.; Li, L.; Chen, F.; Zhang, X.; MacManus-Driscoll, J. L., Self-Assembled Magnetic Metallic Nanopillars in Ceramic Matrix with Anisotropic Magnetic and Electrical Transport Properties. *ACS applied materials & interfaces* 2016, *8* (31), 20283-20291.
84. Park, C.; Yoon, J.; Thomas, E. L., Enabling nanotechnology with self-assembled block copolymer patterns. *Polymer* 2003, *44* (22), 6725-6760.

85. Narayan, J.; Tiwari, A., Novel methods of forming self-assembled nanostructured materials: Ni nanodots in Al<sub>2</sub>O<sub>3</sub> and TiN matrices. *Journal of nanoscience and nanotechnology* 2004, 4 (7), 726-732.
86. Alloyeau, D.; Ricolleau, C.; Mottet, C.; Oikawa, T.; Langlois, C.; Le Bouar, Y.; Braidy, N.; Loiseau, A., Size and shape effects on the order-disorder phase transition in CoPt nanoparticles. *Nature materials* 2009, 8 (12), 940.
87. Tersoff, J.; van Der Gon, A. D.; Tromp, R., Critical island size for layer-by-layer growth. *Physical review letters* 1994, 72 (2), 266.
88. Eaglesham, D.; Cerullo, M., Dislocation-free Stranski-Krastanov growth of Ge on Si (100). *Physical review letters* 1990, 64 (16), 1943.
89. Barabasi, A.-L., Self-assembled island formation in heteroepitaxial growth. *Applied physics letters* 1997, 70 (19), 2565-2567.
90. Zheng, H.; Zhan, Q.; Zavaliche, F.; Sherburne, M.; Straub, F.; Cruz, M. P.; Chen, L.-Q.; Dahmen, U.; Ramesh, R., Controlling self-assembled perovskite– spinel nanostructures. *Nano letters* 2006, 6 (7), 1401-1407.
91. Martin, L.; Chu, Y.-H.; Ramesh, R., Advances in the growth and characterization of magnetic, ferroelectric, and multiferroic oxide thin films. *Materials Science and Engineering: R: Reports* 2010, 68 (4), 89-133.
92. Zhao, R.; Li, W.; Lee, J. H.; Choi, E. M.; Liang, Y.; Zhang, W.; Tang, R.; Wang, H.; Jia, Q.; MacManus-Driscoll, J. L., Precise Tuning of (YBa<sub>2</sub>Cu<sub>3</sub>O<sub>7-δ</sub>)<sub>1-x</sub>:(BaZrO<sub>3</sub>)<sub>x</sub> Thin Film Nanocomposite Structures. *Advanced Functional Materials* 2014, 24 (33), 5240-5245.
93. Ni, Y.; Rao, W.; Khachatryan, A. G., Pseudospinodal mode of decomposition in films and formation of chessboard-like nanostructure. *Nano letters* 2009, 9 (9), 3275-3281.

94. Mecke, K., Morphology of spatial patterns-porous media, spinodal decomposition and dissipative structures. *Acta Physica Polonica. Series B* 1997, 28 (8), 1747-1782.
95. Zhang, C.; Yeo, S.; Horibe, Y.; Choi, Y.; Guha, S.; Croft, M.; Cheong, S.-W.; Mori, S., Coercivity and nanostructure in magnetic spinel  $\text{Mg}(\text{Mn}, \text{Fe})_2\text{O}_4$ . *Applied physics letters* 2007, 90 (13), 133123.
96. Park, S.; Horibe, Y.; Asada, T.; Wielunski, L.; Lee, N.; Bonanno, P.; O'Malley, S.; Sirenko, A.; Kazimirov, A.; Tanimura, M., Highly aligned epitaxial nanorods with a checkerboard pattern in oxide films. *Nano letters* 2008, 8 (2), 720-724.
97. Bi, Z., Vertically aligned nanocomposite thin films. Texas A&M University: 2011.
98. Eason, R., Pulsed laser deposition of thin films: applications-led growth of functional materials. John Wiley & Sons: 2007.
99. Panda, A. K.; Singh, A.; Mishra, M.; Thirumurugesan, R.; Kuppusami, P.; Mohandas, E., Plasma plume behavior of laser ablated cerium oxide: Effect of oxygen partial pressure. *Laser and Particle Beams* 2014, 32 (3), 429-435.
100. Mostako, A.; Khare, A., Effect of target-substrate distance onto the nanostructured rhodium thin films via PLD technique. *Applied Nanoscience* 2012, 2 (3), 189-193.
101. Dam, B.; Stauble-Pumpin, B., Growth mode issues in epitaxy of complex oxide thin films. *Journal of Materials Science: Materials in Electronics* 1998, 9 (3), 217-226.
102. Lee, S.; Sangle, A.; Lu, P.; Chen, A.; Zhang, W.; Lee, J. S.; Wang, H.; Jia, Q.; MacManus-Driscoll, J. L., Novel Electroforming-Free Nanoscaffold Memristor with Very High Uniformity, Tunability, and Density. *Advanced materials* 2014, 26 (36), 6284-6289.

103. Wang, J.; Neaton, J.; Zheng, H.; Nagarajan, V.; Ogale, S.; Liu, B.; Viehland, D.; Vaithyanathan, V.; Schlom, D.; Waghmare, U., Epitaxial BiFeO<sub>3</sub> multiferroic thin film heterostructures. *science* 2003, 299 (5613), 1719-1722.
104. Rossmagel, S. M.; Cuomo, J. J.; Westwood, W. D., Handbook of plasma processing technology: fundamentals, etching, deposition, and surface interactions. William Andrew: 1990.
105. Kaufman, H. R.; Robinson, R. S., Broad-beam ion source technology and applications. *Vacuum* 1989, 39 (11-12), 1175-1180.
106. Chapman, B. N., Glow discharge processes: sputtering and plasma etching. Wiley: 1980.
107. Hoffman, D.; Singh, B.; Thomas III, J. H., Handbook of vacuum science and technology. Academic Press: 1997.
108. Schuegraf, K. K., Handbook of thin-film deposition processes and techniques: principles, methods, equipment, and applications. Noyes Data Corporation/Noyes Publications: 1988.
109. Rossmagel, S.; Kaufman, H., Induced drift currents in circular planar magnetrons. *Journal of Vacuum Science & Technology A: Vacuum, Surfaces, and Films* 1987, 5 (1), 88-91.
110. Thornton, J. A. In Structure-zone models of thin films, Modeling of Optical Thin Films, International Society for Optics and Photonics: 1988; pp 95-106.
111. Cullity, B. D.; Cullity, S. R.; Stock, S., Elements of X-ray Diffraction. 2001.
112. Eaton, P.; West, P., Atomic force microscopy. Oxford University Press: 2010.
113. Horcas, I.; Fernández, R.; Gomez-Rodriguez, J.; Colchero, J.; Gómez-Herrero, J.; Baro, A., WSXM: a software for scanning probe microscopy and a tool for nanotechnology. *Review of Scientific Instruments* 2007, 78 (1), 013705.

114. Su, Q.; Yoon, D.; Chen, A.; Khatkhatay, F.; Manthiram, A.; Wang, H., Vertically aligned nanocomposite electrolytes with superior out-of-plane ionic conductivity for solid oxide fuel cells. *Journal of Power Sources* 2013, 242, 455-463.
115. Tra, V. T.; Yang, J. C.; Hsieh, Y. H.; Lin, J. Y.; Chen, Y. C.; Chu, Y. H., Controllable electrical conduction at complex oxide interfaces. *physica status solidi (RRL)-Rapid Research Letters* 2014, 8 (6), 478-500.
116. Kursumovic, A.; Defay, E.; Lee, O. J.; Tsai, C. F.; Bi, Z.; Wang, H.; MacManus-Driscoll, J. L., A New Material for High-Temperature Lead-Free Actuators. *Advanced Functional Materials* 2013, 23 (47), 5881-5886.
117. Oon, J. L. Nanocomposites of  $Ba_{0.6}Sr_{0.4}TiO_3-Sm_2O_3$  for enhanced tunability and reduced dielectric loss. United Kingdom: University of Cambridge, 2013.
118. Fang, T.-H.; Chang, W.-J.; Lin, C.-M.; Ji, L.-W.; Chang, Y.-S.; Hsiao, Y.-J., Effect of annealing on the structural and mechanical properties of  $Ba_{0.7}Sr_{0.3}TiO_3$  thin films. *Materials Science and Engineering: A* 2006, 426 (1), 157-161.
119. Gunn, D. S.; Allan, N. L.; Purton, J. A., Adaptive kinetic Monte Carlo simulation of solid oxide fuel cell components. *Journal of Materials Chemistry A* 2014, 2 (33), 13407-13414.
120. Wimbush, S. C.; Li, M.; Vickers, M. E.; Maiorov, B.; Feldmann, D. M.; Jia, Q.; MacManus-Driscoll, J. L., Interfacial Strain-Induced Oxygen Disorder as the Cause of Enhanced Critical Current Density in Superconducting Thin Films. *Advanced Functional Materials* 2009, 19 (6), 835-841.
121. Stecura, S.; Campbell, W. J. Thermal expansion and phase inversion of rare-earth oxides; Bureau of Mines. College Park Metallurgy Research Center, Md.: 1960.

122. Ban, Z.-G.; Alpay, S., Phase diagrams and dielectric response of epitaxial barium strontium titanate films: A theoretical analysis. *Journal of Applied Physics* 2002, 91 (11), 9288-9296.
123. Banerjee, S.; Mukhopadhyay, P., Phase transformations: examples from titanium and zirconium alloys. Elsevier: 2010; Vol. 12.
124. Jaffe, B., Piezoelectric ceramics. Elsevier: 2012; Vol. 3.
125. Foster, L. S., New developments in ferromagnetic materials. ACS Publications: 1948.
126. Singh, R., Unexpected magnetism in nanomaterials. *Journal of Magnetism and Magnetic Materials* 2013, 346, 58-73.
127. Anderson, P., Antiferromagnetism. Theory of superexchange interaction. *Physical Review* 1950, 79 (2), 350.
128. Zener, C., Interaction between the d-shells in the transition metals. II. Ferromagnetic compounds of manganese with perovskite structure. *Physical Review* 1951, 82 (3), 403.
129. Coey, J.; Viret, M.; von Molnar, S., Mixed-valence manganites—ten years on. 2009.
130. Prellier, W.; Singh, M.; Murugavel, P., The single-phase multiferroic oxides: from bulk to thin film. *Journal of Physics: Condensed Matter* 2005, 17 (30), R803.
131. Eerenstein, W.; Mathur, N.; Scott, J. F., Multiferroic and magnetoelectric materials. *Nature* 2006, 442 (7104), 759.
132. Ramesh, R.; Spaldin, N. A., Multiferroics: progress and prospects in thin films. *Nature materials* 2007, 6 (1), 21-29.

133. Moodera, J.; Hao, X.; Gibson, G.; Meservey, R., Electron-spin polarization in tunnel junctions in zero applied field with ferromagnetic EuS barriers. *Physical Review Letters* 1988, 61 (5), 637.
134. LeClair, P.; Ha, J.; Swagten, H.; Kohlhepp, J.; Van de Vin, C.; De Jonge, W., Large magnetoresistance using hybrid spin filter devices. *Applied Physics Letters* 2002, 80 (4), 625-627.
135. Rogado, N. S.; Li, J.; Sleight, A. W.; Subramanian, M. A., Magnetocapacitance and magnetoresistance near room temperature in a ferromagnetic semiconductor:  $\text{La}_2\text{NiMnO}_6$ . *Advanced Materials* 2005, 17 (18), 2225-2227.
136. Lou, J.; Insignares, R.; Cai, Z.; Ziemer, K. S.; Liu, M.; Sun, N. X., Soft magnetism, magnetostriction, and microwave properties of FeGaB thin films. *Applied Physics Letters* 2007, 91 (18), 182504.
137. Moodera, J. S.; Nowak, J.; van de Veerdonk, R. J., Interface magnetism and spin wave scattering in ferromagnet-insulator-ferromagnet tunnel junctions. *Physical Review Letters* 1998, 80 (13), 2941.
138. Santos, T. S.; Moodera, J. S., Observation of spin filtering with a ferromagnetic EuO tunnel barrier. *Physical Review B* 2004, 69 (24), 241203.
139. Natali, F.; Ruck, B. J.; Plank, N. O.; Trodahl, H. J.; Granville, S.; Meyer, C.; Lambrecht, W. R., Rare-earth mononitrides. *Progress in Materials Science* 2013, 58 (8), 1316-1360.
140. Bowen, M.; Bibes, M.; Barthélémy, A.; Contour, J.-P.; Anane, A.; Lemaitre, Y.; Fert, A., Nearly total spin polarization in  $\text{La}_{2/3}\text{Sr}_{1/3}\text{MnO}_3$  from tunneling experiments. *Applied Physics Letters* 2003, 82 (2), 233-235.
141. Haghiri-Gosnet, A.; Renard, J., CMR manganites: physics, thin films and devices. *Journal of Physics D: Applied Physics* 2003, 36 (8), R127.

142. Bibes, M.; Villegas, J. E.; Barthélémy, A., Ultrathin oxide films and interfaces for electronics and spintronics. *Advances in Physics* 2011, 60 (1), 5-84.
143. Hwang, H. Y.; Iwasa, Y.; Kawasaki, M.; Keimer, B.; Nagaosa, N.; Tokura, Y., Emergent phenomena at oxide interfaces. *Nature materials* 2012, 11 (2), 103.
144. Dagotto, E.; Hotta, T.; Moreo, A., Colossal magnetoresistant materials: the key role of phase separation. *Physics reports* 2001, 344 (1), 1-153.
145. Tokura, Y.; Nagaosa, N., Orbital physics in transition-metal oxides. *Science* 2000, 288 (5465), 462-468.
146. Gajek, M.; Bibes, M.; Barthélémy, A.; Bouzouane, K.; Fusil, S.; Varela, M.; Fontcuberta, J.; Fert, A., Spin filtering through ferromagnetic BiMnO<sub>3</sub> tunnel barriers. *Physical Review B* 2005, 72 (2), 020406.
147. Gajek, M.; Bibes, M.; Fusil, S.; Bouzouane, K.; Fontcuberta, J.; Barthélémy, A.; Fert, A., Tunnel junctions with multiferroic barriers. *Nature materials* 2007, 6 (4), 296.
148. Kurbakov, A.; Lazuta, A.; Ryzhov, V. Phase diagram of Sm<sub>1-x</sub>Sr<sub>x</sub>MnO<sub>3</sub> perovskite manganites, *Journal of Physics: Conference Series*, IOP Publishing: 2010; p 012099.
149. Kurbakov, A., Phase diagram of perovskite manganites Sm<sub>1-x</sub>Sr<sub>x</sub>MnO<sub>3</sub>. *Physics of the Solid State* 2009, 51 (6), 1210-1216.
150. Prasad, B.; Egilmez, M.; Schoofs, F.; Fix, T.; Vickers, M. E.; Zhang, W.; Jian, J.; Wang, H.; Blamire, M. G., Nanopillar spin filter tunnel junctions with manganite barriers. *Nano letters* 2014, 14 (5), 2789-2793.
151. Prasad, B.; Zhang, W.; Jian, J.; Wang, H.; Blamire, M. G., Strongly Bias-Dependent Tunnel Magnetoresistance in Manganite Spin Filter Tunnel Junctions. *Advanced Materials* 2015, 27 (19), 3079-3084.

152. Egilmez, M.; Abdelhadi, M.; Salman, Z.; Chow, K.; Jung, J., Enhancement of the magnetotransport and magnetoresistive anisotropy in  $\text{Sm}_{0.55}\text{Sr}_{0.45}\text{MnO}_3/\text{Nd}_{0.55}\text{Sr}_{0.45}\text{MnO}_3$  bilayers. *Applied Physics Letters* 2009, 95 (11), 112505.
153. Kasai, M.; Kuwahara, H.; Tomioka, Y.; Tokura, Y., Colossal magnetoresistance in  $\text{Sm}_{1-x}\text{Sr}_x\text{MnO}_3$  films. *Journal of applied physics* 1996, 80 (12), 6894-6897.
154. Oshima, H.; Miyano, K.; Konishi, Y.; Kawasaki, M.; Tokura, Y., Switching behavior of epitaxial perovskite manganite thin films. *Applied physics letters* 1999, 75 (10), 1473-1475.
155. Srivastava, M.; Singh, M.; Siwach, P.; Kaur, A.; Razavi, F.; Singh, H., Impact of substrate on magnetic phase coexistence in bicritical  $\text{Sm}_{0.53}\text{Sr}_{0.47}\text{MnO}_3$  thin films. *Solid State Communications* 2012, 152 (2), 138-141.
156. Srivastava, M. K.; Singh, M.; Kaur, A.; Razavi, F.; Singh, H., Low field anisotropic colossal magnetoresistance in  $\text{Sm}_{0.53}\text{Sr}_{0.47}\text{MnO}_3$  thin films. *Journal of Applied Physics* 2011, 110 (12), 123922.
157. Srivastava, M. K.; Siwach, P.; Kaur, A.; Singh, H., Impact of Growth Conditions on the Nature of Magnetism and Magnetotransport of  $\text{Sm}_{0.55}\text{Sr}_{0.45}\text{MnO}_3$  Thin Films. *IEEE Transactions on Magnetism* 2011, 47 (10), 2486-2489.
158. Dagotto, E., Open questions in CMR manganites, relevance of clustered states and analogies with other compounds including the cuprates. *New Journal of Physics* 2005, 7 (1), 67.
159. Gazquez, J.; Bose, S.; Sharma, M.; Torija, M.; Pennycook, S. J.; Leighton, C.; Varela, M., Lattice mismatch accommodation via oxygen vacancy ordering in epitaxial  $\text{La}_{0.5}\text{Sr}_{0.5}\text{CoO}_{3-\delta}$  thin films. *APL Materials* 2013, 1 (1), 012105.

160. Choi, E. M.; Fix, T.; Kursumovic, A.; Kinane, C. J.; Arena, D.; Sahonta, S. L.; Bi, Z.; Xiong, J.; Yan, L.; Lee, J. S., Room temperature ferrimagnetism and ferroelectricity in strained, thin films of  $\text{BiFe}_{0.5}\text{Mn}_{0.5}\text{O}_3$ . *Advanced functional materials* 2014, 24 (47), 7478-7487.
161. Choi, E.-M.; Kursumovic, A.; Lee, O. J.; Kleibeuker, J. e. E.; Chen, A.; Zhang, W.; Wang, H.; MacManus-Driscoll, J. L., Ferroelectric Sm-Doped  $\text{BiMnO}_3$  Thin Films with Ferromagnetic Transition Temperature Enhanced to 140 K. *ACS applied materials & interfaces* 2014, 6 (17), 14836-14843.
162. Singh, M.; Truong, K.; Fournier, P.; Rauwel, P.; Rauwel, E.; Carignan, L.; Ménard, D., Anomalously large ferromagnetic Curie temperature of epitaxial  $\text{Bi}_2\text{CoMnO}_6$  thin films. *Applied Physics Letters* 2008, 92 (11), 112505.
163. Ueda, K.; Muraoka, Y.; Tabata, H.; Kawai, T., Atomic ordering in the  $\text{LaFe}_{0.5}\text{Mn}_{0.5}\text{O}_3$  solid solution film. *Applied Physics Letters* 2001, 78 (4), 512-514.
164. Dunstan, D.; Young, S.; Dixon, R., Geometrical theory of critical thickness and relaxation in strained-layer growth. *Journal of applied physics* 1991, 70 (6), 3038-3045.
165. Sankarrajan, S.; Aravindan, S.; Rajkumar, M.; Rajendran, V., Ultrasonic and elastic moduli evidence for Curie temperature ( $T_c$ ) in  $\text{Sm}_{1-x}\text{Sr}_x\text{MnO}_3$  perovskite magnetic materials at  $x=0.25, 0.30, 0.37, 0.40$  and  $0.44$ . *Journal of Alloys and Compounds* 2009, 485 (1), 17-25.
166. Jung, W.; Tuller, H. L., Investigation of surface Sr segregation in model thin film solid oxide fuel cell perovskite electrodes. *Energy & Environmental Science* 2012, 5 (1), 5370-5378.
167. Suwardi, A.; Prasad, B.; Lee, S.; Choi, E.-M.; Lu, P.; Zhang, W.; Li, L.; Blamire, M.; Jia, Q.; Wang, H., Turning antiferromagnetic  $\text{Sm}_{0.34}\text{Sr}_{0.66}\text{MnO}_3$  into a 140 K

- ferromagnet using a nanocomposite strain tuning approach. *Nanoscale* 2016, 8 (15), 8083-8090.
168. Yang, H.; Wang, H.; Luo, H.; Feldmann, D.; Dowden, P.; DePaula, R.; Jia, Q., Structural and dielectric properties of epitaxial  $\text{Sm}_2\text{O}_3$  thin films. *Applied Physics Letters* 2008, 92 (6), 062905.
169. Kurbakov, A.; Martin, C.; Maignan, A., Crystal and magnetic structures and physical properties of the  $\text{Sm}_{0.37}\text{Sr}_{0.63}\text{MnO}_3$  manganite. *Physics of the Solid State* 2008, 50 (2), 275-282.
170. Worledge, D.; Snyder, G. J.; Beasley, M.; Geballe, T.; Hiskes, R.; DiCarolis, S., Anneal-tunable Curie temperature and transport of  $\text{La}_{0.67}\text{Ca}_{0.33}\text{MnO}_3$ . *Journal of applied physics* 1996, 80 (9), 5158-5161.
171. Prasad, R.; Singh, H.; Singh, M.; Prellier, W.; Siwach, P.; Kaur, A., Thickness dependent transport properties of compressively strained  $\text{La}_{0.88}\text{Sr}_{0.12}\text{MnO}_3$  ultrathin films. *Journal of Applied Physics* 2008, 103 (8), 083906.
172. Hassen, A.; Mandal, P., Correlation between structural, transport, and magnetic properties in  $\text{Sm}_{1-x}\text{A}_x\text{MnO}_3$  (A= Sr, Ca). *Journal of applied physics* 2007, 101 (11), 113917.
173. Martin, C.; Maignan, A.; Hervieu, M.; Raveau, B., Magnetic phase diagrams of  $\text{L}_{1-x}\text{A}_x\text{MnO}_3$  manganites (L= Pr, Sm; A= Ca, Sr). *Physical Review B* 1999, 60 (17), 12191.
174. Srivastava, M. K.; Singh, S.; Siwach, P.; Kaur, A.; Awana, V.; Maurya, K.; Singh, H., Comparative study of magnetic and magnetotransport properties of  $\text{Sm}_{0.55}\text{Sr}_{0.45}\text{MnO}_3$  thin films grown on different substrates. *AIP Advances* 2013, 3 (5), 052118.

175. Nanda, B.; Satpathy, S., Effects of strain on orbital ordering and magnetism at perovskite oxide interfaces: LaMnO<sub>3</sub>/SrMnO<sub>3</sub>. *Physical Review B* 2008, 78 (5), 054427.
176. Kozlenko, D.; Dang, N.; Jiráček, Z.; Kichanov, S.; Lukin, E.; Savenko, B.; Dubrovinsky, L.; Lathe, C.; Martin, C., Structural and magnetic phase transitions in Pr<sub>0.15</sub>Sr<sub>0.85</sub>MnO<sub>3</sub> at high pressure. *The European Physical Journal B-Condensed Matter and Complex Systems* 2010, 77 (3), 407-411.
177. Sadoc, A.; Mercey, B.; Simon, C.; Grebille, D.; Prellier, W.; Lepetit, M.-B., Large increase of the Curie temperature by orbital ordering control. *Physical review letters* 2010, 104 (4), 046804.
178. Zhang, D.; Yang, T.; Ma, J.; Wang, Q.; Gao, R.; Ma, H., Preparation of transparent conducting ZnO: Al films on polymer substrates by rf magnetron sputtering. *Applied Surface Science* 2000, 158 (1), 43-48.
179. Catherine, Y.; Couderc, P., Electrical characteristics and growth kinetics in discharges used for plasma deposition of amorphous carbon. *Thin Solid Films* 1986, 144 (2), 265-280.
180. Izaki, M.; Shinagawa, T.; Mizuno, K.-T.; Ida, Y.; Inaba, M.; Tasaka, A., Electrochemically constructed p-Cu<sub>2</sub>O/n-ZnO heterojunction diode for photovoltaic device. *Journal of Physics D: Applied Physics* 2007, 40 (11), 3326.
181. Musselman, K. P.; Marin, A.; Schmidt-Mende, L.; MacManus-Driscoll, J. L., Incompatible length scales in nanostructured Cu<sub>2</sub>O solar cells. *Advanced Functional Materials* 2012, 22 (10), 2202-2208.
182. Silberberg, M., *Principles of general chemistry*. McGraw-Hill Higher Education: 2012.